



UNIVERSITA' DEGLI STUDI DI PADOVA

Sede Amministrativa: Università degli Studi di Padova

Sede Consorziata: Università degli Studi di Trento

Dipartimento di Ingegneria Meccanica ed Innovazione Gestionale (D.I.M.E.G.)

DOTTORATO DI RICERCA IN : INGEGNERIA METALLURGICA

CICLO : XX

**MIGLIORAMENTO DELLA RESISTENZA AD OSSIDAZIONE DI UNA LEGA γ -TiAl
MEDIANTE NANOCRISTALLIZZAZIONE SUPERFICIALE ED EFFETTO GETTERING**

Coordinatore : Ch.mo Prof. Emilio Ramous

Supervisore : Ch.mo Prof. Diego Colombo ; Ch.mo Prof. Stefano Gialanella

Dottorando : Marco Mandelli

DATA CONSEGNA TESI
31 gennaio 2008

ABSTRACT

γ -titanium aluminide alloys possess many attractive properties such as low density and good high temperature strength which recommend their use in moving structural parts at elevated temperatures. At present, applications as blades in gas turbines and as valves, turbocharger rotors, etc. in car engines are the aim of development in industry. The most limiting factor for their use as high temperature operating components is the weak oxidation resistance at temperatures in excess of 700 °C. Two are the aims of this work: understanding the oxidation mechanism of TiAl alloys in relation with the influence of various parameters (composition, microstructure) on it and the development of new methods in order to increase the oxidation resistance.

In order to perform the first task the most promising methodologies are here presented: the chlorine effect, aluminizing, siliconizing, pack diffusion coatings.

We will finally propose two methods for oxidation resistance improvement: nanocrystallization via laser ablation and superficial chrome enrichment via vacuum interdiffusion of a chrome layer (deposited via laser ablation). The final result is the development of a new promising and versatile methodology which will extend the use of these materials at temperatures in excess of 900 °C.

Much attention is focused on the “numbers” of those phenomena: a finite-difference oxidative model will be developed in order to predict the oxide scale composition, the effect of the grain size on the oxidative behaviour and to calculate the thermal treating duration for the chrome interdiffusion step. The result is a very flexible and versatile approach.

RIASSUNTO

Le leghe basate sulla fase intermetallica γ -TiAl presentano delle interessanti proprietà meccaniche specifiche, anche a temperature relativamente elevate: per questo motivo sono attivamente studiate e hanno trovato diversi impieghi per componenti operanti ad alta temperatura come alcuni componenti di turbogas e motori a scoppio. Nel presente lavoro sono presentati i risultati di uno studio sperimentale nel corso del quale è stato indagato il comportamento ad ossidazione di una lega TiAl nelle condizioni di fornitura e dopo due diversi trattamenti superficiali. In un caso, preliminarmente ai trattamenti ossidativi è stato fatto diffondere all'interno della lega del cromo, deposto sulla superficie dei campioni con una tecnica PVD (physical vapour deposition) basata sull'ablazione laser. La medesima tecnica è stata impiegata per il secondo trattamento superficiale, nel corso del quale la superficie della lega è stata fatta fondere e solidificare così rapidamente da indurre la formazione di uno strato superficiale nanocristallino, che permette l'attivazione di ulteriori percorsi di diffusione, in aggiunta alla diffusione all'interno dei grani cristallini. Nel caso specifico, questa condizione rende possibile un maggior flusso di alluminio verso la superficie, promuovendo la formazione di una scaglia più ricca in allumina determinando una più contenuta cinetica di ossidazione, rispetto a quella osservata nella lega non trattata. Eccezionalmente basse si sono rivelate le cinetiche di ossidazione dei campioni la cui superficie è stata preliminarmente arricchita di cromo. I risultati cinetici, opportunamente modellati, forniscono delle indicazioni circa i meccanismi che dominano la ossidazione della lega nelle tre diverse condizioni e possono essere utilmente impiegati per migliorare ulteriormente i trattamenti superficiali. Sono poi analizzate tutte le ulteriori tecniche di miglioramento della proprietà ossidative tra quelle disponibili in letteratura.

ad Elisabetta ed ai miei genitori

Desidero ringraziare vivamente il Prof. Stefano Gialanella che mi ha seguito durante tutto il percorso : da lui ho sempre ricevuto con una semplicità “ disarmante “ tutte le risposte di cui avevo bisogno. Non meno importante è la mia riconoscenza nei confronti dei Prof. Diego Colombo , Alberto Molinari , Luca Lutterotti e degli Ing. Gloria Ischia , Mauro Bortoloti , Ivan Lonardelli , Fabrizio Girardi : grazie a loro una esperienza interessante ed impegnativa è stata prima di tutto piacevole.

OVERALL INDEX

Chapter 1	Introduction	pag	6
Chapter 2	How to measure the oxidation resistance	pag	10
Chapter 3	Strategies for oxidation resistance improvement		
Chapter 3.1	Microalloying effect on oxidation properties: the chlorine effect	pag	12
Chapter 3.2	NiAl coatings	pag	17
Chapter 3.3	Effect of alloying elements on oxidation resistance	pag	20
Chapter 3.4	Two-step Cr and Al diffusion coating on TiAl at high temperatures	pag	23
Chapter 3.5	Long-term oxidation properties of Al–Ti–Cr two-phase alloys as coating materials for TiAl alloys	pag	26
Chapter 3.6	Influence of siliconizing on the oxidation behaviour of a γ -TiAl based alloy	pag	31
Chapter 3.7	The improvement of high temperature oxidation of Ti–50Al by sputtering Al film and subsequent interdiffusion treatment	pag	37
Chapter 4	Oxidation resistance improvement via laser ablation	pag	43
Chapter 4.1	The nanocrystallization via laser ablation	pag	45
Chapter 4.2	Experimental	pag	48
Chapter 4.3	Results and discussion	pag	50
Chapter 5	Improvement of TiAl oxidation resistance using the “gettering effect”	pag	75
Chapter 5.1	Experimental	pag	76
Chapter 5.2	Results and discussion	pag	79
Chapter 6	Conclusions	pag	88
Bibliography		pag	91

1 INTRODUCTION

γ -titanium aluminide alloys possess many attractive properties such as low density and good high temperature strength which recommend their use in moving structural parts at elevated temperatures. At present, applications as blades in gas turbines and as valves, turbocharger rotors, etc. in car engines are the aim of development in industry. Major drawbacks which still have to be overcome are the limited ductility at room temperature and the insufficient oxidation resistance at temperatures above 700°C [1] Much work has already been done on the first aspect which is reported in [2].

The work on oxidation resistance has been very much focused over the last years on understanding mechanisms for a consequent development of alloys and coatings with optimum oxidation behaviour. Fig 1.1 show us the normalized specific strength (ratio between strength and density) and the oxidation resistance for various Ti alloys.

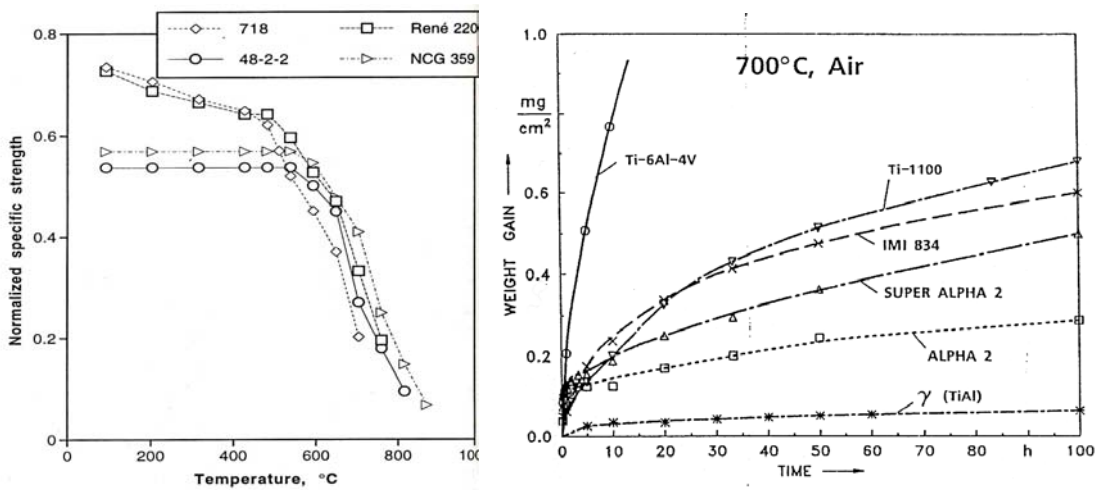


Figure 1.1 Normalized specific strength and oxidative weight gain for various Ti alloys at different temperatures

It is clearly visible that gamma-TiAl alloys offers the best oxidation resistance properties among Ti alloys. The gamma and the α_2 crystal-structures are displayed in Fig 1.2

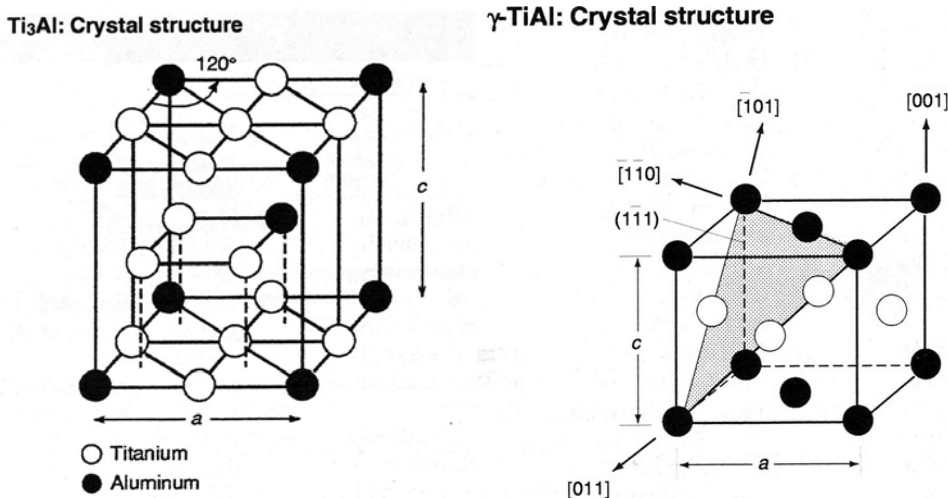


Figure 1.2 Crystal structures for TiAl and Ti₃Al

As a basis for understanding the relative weak oxidation resistance of TiAl alloys is that she usually significantly drops at temperatures above 700°C. The main aspect is that Al₂O₃ is a slow growing protective type of oxide at these temperatures while TiO₂ belongs to the fast growing oxides of non-protective nature .

In other words sufficient oxidation resistance is only achieved if either a continuous alumina layer is formed or if at least a continuous partial layer of alumina exists in the mixture of Al₂O₃ and TiO₂ forming the surface scale.

As shown in the Fig 1.3 , Al₂O₃ is the “preferred” oxide due the very low growth rate.

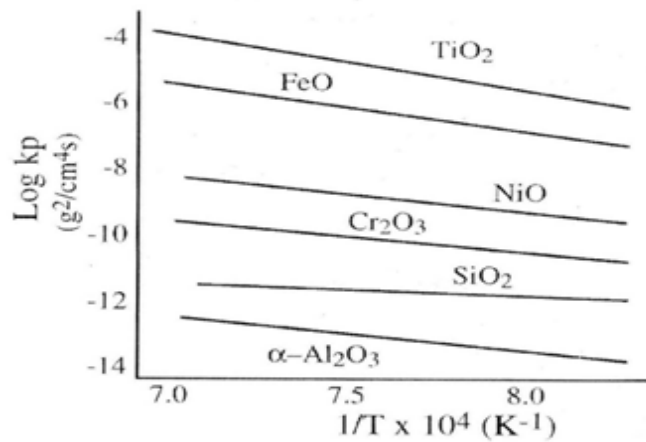


Figure 1.3 Kp values for various substrates which are forming a specific oxide during oxidation

As the results in the literature indicate [4] there may be the formation of an alumina (partial) layer on TiAl alloys in many cases which shows, however, only a temporary stability and may become dissolved after a limited time, thus, leading to a breakaway effect in oxidation. This problem is less marked in pure oxygen than in air but it exists in both atmospheres. Fig. 1.4 show a phase stability diagram for atmospheres containing oxygen and nitrogen at 900°C and for the metals Al and Ti, each with an activity of 1.

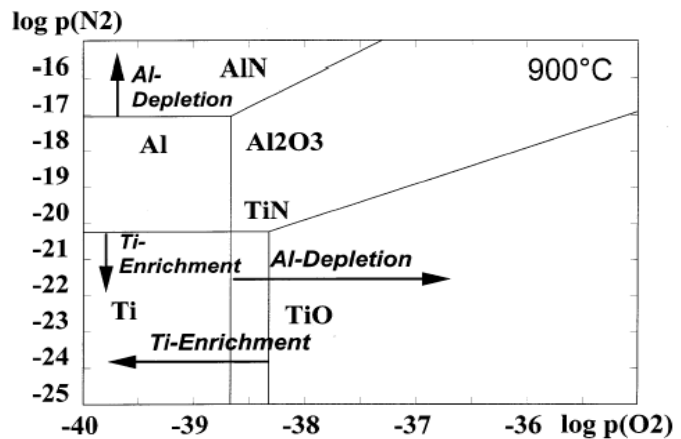


Figure 1.4 Stability diagram at 900 °C for Al-Ti_N-O system

In this diagram it is evident that the stability of Al₂O₃ is only slightly higher than that of TiO (which becomes oxidized to TiO₂ as found in the actual scales), i.e. only slight differences in the Ti and Al activities may turn the stabilities of the oxides formed on the corresponding substrate.

Even for Ti50Al (at.%) alloy the formation of TiO is favoured.

Nevertheless, in the experiments alumina formation is often observed in the beginning which leads to Al-depletion and Ti-enrichment, thus, switching to TiO/TiO₂ formation as the increase of Ti activity renders TiO the more stable oxide. This in turn leads to Al-enrichment and Ti-depletion favouring Al₂O₃ formation again. Usually the result is a scale with a complex mixture of Al₂O₃ and TiO₂ and a structure as shown in Fig. 1.5

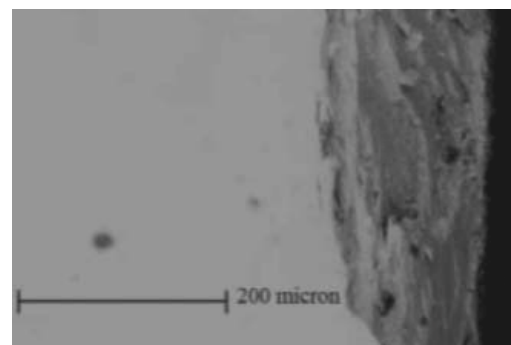


Figure 1.5 Typical oxide scale appearance

In air the formation of a non-protective mixed $\text{Al}_2\text{O}_3/\text{TiO}_2$ scale is further facilitated by the presence of nitrogen (nitrogen effect [13,14]) leading to $\text{Al}_2\text{O}_3/\text{TiN}$ at the scale/substrate interface TiN later becomes oxidized to TiO_2 .

Thus, again the formation of a permanently stable Al_2O_3 partial layer which could act as a barrier is impeded.

Relatively few activities were performed in order to improve the oxidation resistance by adding different elements such as Ni, Co, Au, Ag, Sn, Y, Zr, Hf , Cr, V, Mn, Pd, Pt , Cu, W, Nb, Mo and Si. Among these elements it is mainly Nb which is now used as an alloying element in the more advanced technical versions of the TiAl alloys for increasing the oxidation resistance.

Vanadium addition is almost detrimental but enhances the castability. It should, however, be mentioned that those elements improving oxidation resistance in many cases have a negative effect on the mechanical properties and vice versa. This was the reason why also ‘microalloying’ elements were investigated, i.e. additions in the range of a few hundred ppm. These were C, B, P, Se, Te and the halogens Cl, F, Br [5-9]. C and B seem to have some beneficial effect on oxidation resistance as well as P, Se and Te. However, a really significant effect was found in particular for Cl and to a certain extent also for F and Br.

In this work four main strategies are tested and/or explained

- Microalloying (halogen effect , Cr enrichment)
- Effect of various element additions (alloying)
- Superficial treatment (nanocrystallization)
- Coating

The third approach is related with the relationships between diffusivity and oxidation behaviour : the diffusion influences strongly the “path” in the stability diagram during oxidation ; Enhancing the Al diffusivity makes it possible to guarantee an optimal Al concentration at oxidation interface leading to an alumina rich oxide scale.

In other words oxidation is dominated by two “ considerations “ : thermodynamic stability of the oxide and kinetic.

2 HOW TO MEASURE THE OXIDATION RESISTANCE OF AN ALLOY?

Oxidation resistance is generally “measured” with two methodologies:

- By measuring the weight change during high temperature exposure
- By measuring the oxide scale thickness

In the first case the dimensions are usually [mgcm^{-2}] and in the second case [$\mu\text{m}^2 \text{s}^{-1}$], due the often used “parabolic oxide growth law “ which assumes that :

$$s = \sqrt{K_p * t}$$

where “s” is the oxide scale thickness and “t” the time.

K_p is called “parabolic oxidation factor “ and follows the Arrheius Law for thermal – activated phenomena

$$K_p = K_o * \text{Exp}\left(\frac{-E_{att}}{RT}\right)$$

K_o is a constant and E_{att} is the “energy of the activated complex “ and their units are [J Mol^{-1}]

We can at this point define “two type of K_p ”

- K_p referred to weight changes
- K_p referred to oxide scale thickness

If $V_{Al_2O_3}$ and V_{TiO_2} indicates the volume of a unit alumina and titania cell then

$$V_{ox} = n^{\circ} \text{ cells } Al_2O_3 \cdot V_{Al_2O_3} + n^{\circ} \text{ cells } TiO_2 \cdot V_{TiO_2} ; \quad V_{Al_2O_3} = 254.89 \text{ \AA}^3 ; \quad V_{TiO_2} = 62,43 \text{ \AA}^3$$

Where V_{ox} is the volume of the formed oxide scale.

In the basic alumina cell 22 atoms of oxygen are been coordinated and 6 in the titania basic cell as shown in Fig 2.1

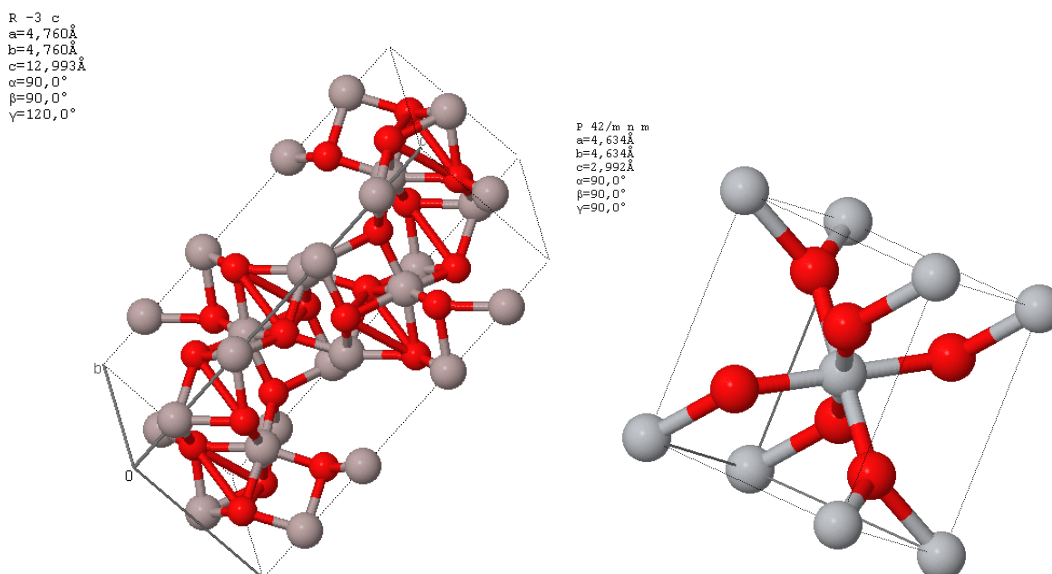


Figure 2.1 Crystal cells for alumina (left side) and titania (right side)

This fact leads to :

$$n^{\circ}at.O = n^{\circ}cellsAl_2O_3 \cdot 22 + n^{\circ}cellsTiO_2 \cdot 6$$

The mass of the oxygen atoms added to the material is therefore

$$mO = \frac{n^{\circ}at.O}{NA} \cdot PA = \frac{n^{\circ}at.O}{6.022 \times 10^{23}} \cdot 16 \left[\frac{mg}{cm^2} \right]$$

In order to calculate the oxygen mass it is necessary to know the titania – alumina ratio : this parameter can be determined through an XRD analysis. Fortunately the “added mass” is in fact practically independent from titania – alumina ratio and one micron thick formed oxide leads to 0.237 mgcm^{-2} weight gain for $1\mu\text{m}$ of oxide.

Two are the aims of this work :

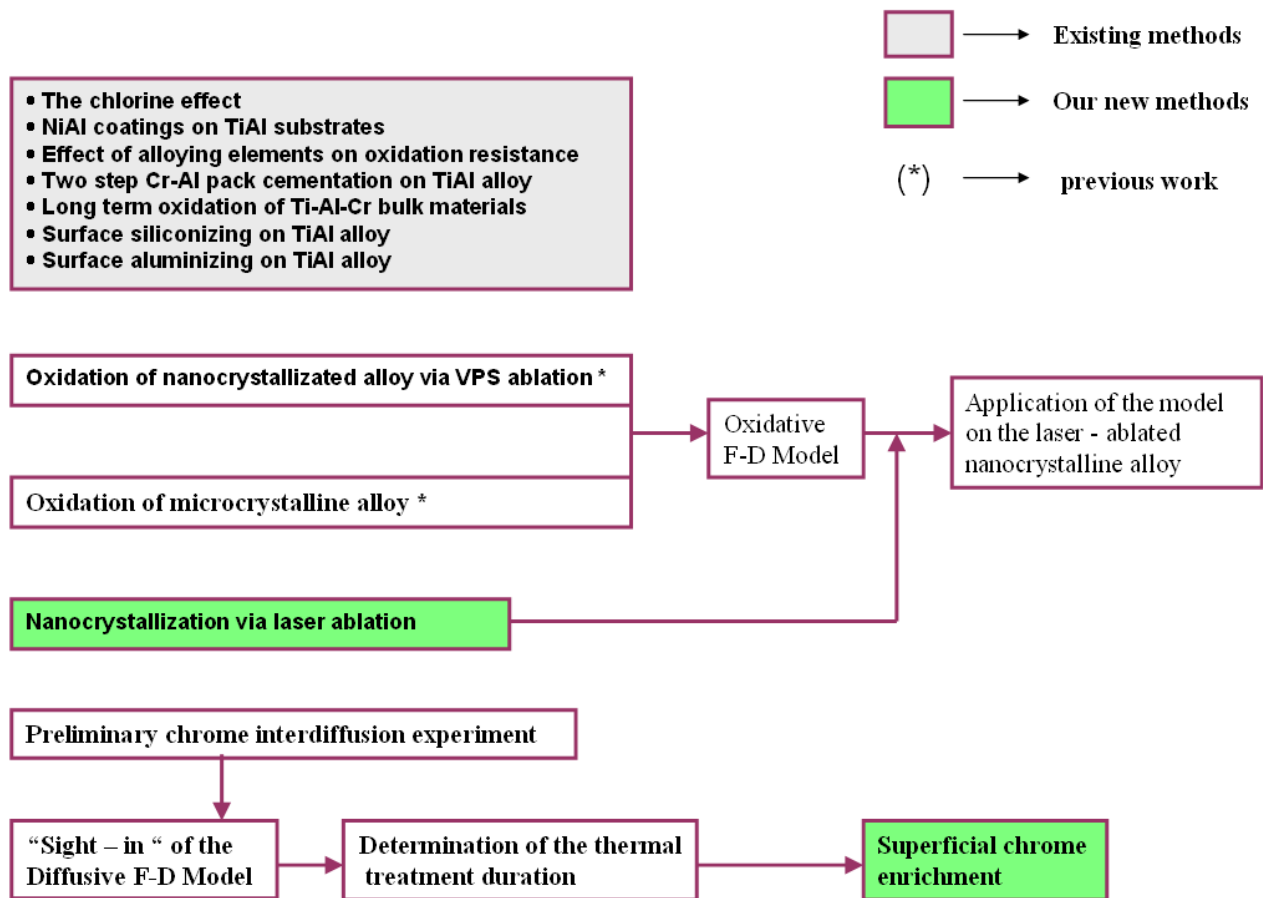
- Understanding the oxidation mechanism of TiAl alloys and the influence of various parameters (composition , microstructure) on it
- The development of new methods in order to increase the oxidation resistance

In order to perform the first task a wide overview of the actual methodologies is presented. We will finally propose two methods for oxidation resistance improvement :

- Nanocrystallization via laser ablation
- Superficial chrome enrichment via vacuum interdiffusion of an PVD deposited chrome layer

Much attention is focused on the “ numbers “ of those phenomena : a finite – difference oxidative model will be developed in order to predict the oxide scale composition , the effect of the grain size on the oxidative behaviour and to calculate the thermal treating duration for the chrome interdiffusion step. The result is a very flexible and versatile approach.

The present work can be summarized as follows:



3.1 MICROALLOYING EFFECT ON OXIDATION PROPERTIES: THE CHLORINE EFFECT ^[9]

Specimen were prepared from stoichiometric γ -TiAl (50% at Al) with subsequent polishing at 4000 grit SiC paper. Microalloying was performed with ion implantation at 70°C on two different bulk materials : TiAl-1.5Cr and γ -AB . The compositions of these alloys are given in Table 3.1. The dose of ion implantation was varied between 10^{15} and $2 \cdot 10^{17}$ ions/cm² and the energies ranged between 15 KeV and 6 MeV.

Chemical analysis of the alloys TiAl-1.5Cr and γ -TAB

	Ti	Al	Cr	Nb	Mn	Si	B
TiAl-1.5Cr	50.1	48.2	1.5	-	-	-	0.007
γ -TAB	48.5	47.4	1.1	1.6	1.2	0.2	0.2

Table 3.1.1 Chemical compositions of the two tested Ti alloys

The result of oxidation test in air at 900 °C were displayed in Fig 3.1. The figure indicates that Cl,I,Br lie in the same scatter band while the unimplanted alloy exhibits much faster oxidation rate.

In the first 2 hours of oxidation the oxidation rates of the three halogen doped specimens are of the same magnitude of the unimplanted alloy but after this incubation period the rate soon drops down to very low values which corresponds to the behaviour of a pure alumina former , as shown in Fig 3.1.

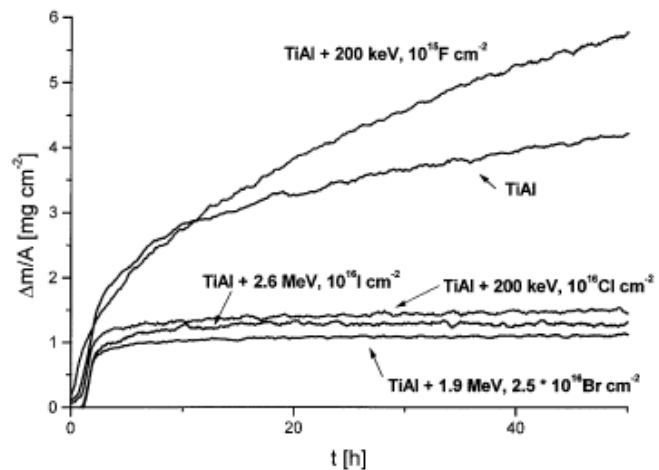


Figure 3.1.1 Weight change due the oxidation at 900 °C in air

Fig 3.2a shows a single side chlorine micro-alloyed Ti48Al 1.5 Cr oxidized for 100h at 900 °C , in air.

Very thick oxide scale is present on the chlorine-implanted side . Implantation dose was 10^{16} Cl ions/cm² with 1MeV energy.

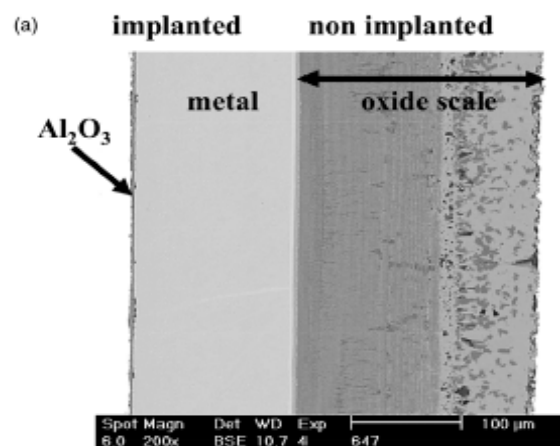


Figure 3.1.2a Single side alloyed Ti48Al 1.5 Cr oxidized for 100h at 900 °C , in air.

Fig 3.2b show the cross section of an Ti48Al1.5Cr alloy with lower implantation energy. Implantation dose was 10^{16} Cl ions/cm² with 400 KeV energy. Oxidation conditions are 100h at 900 °C. Markers n° 1,2,3,4 indicates TiO₂ , Al₂O₃, Al depletion zone and TiAl , respectively.

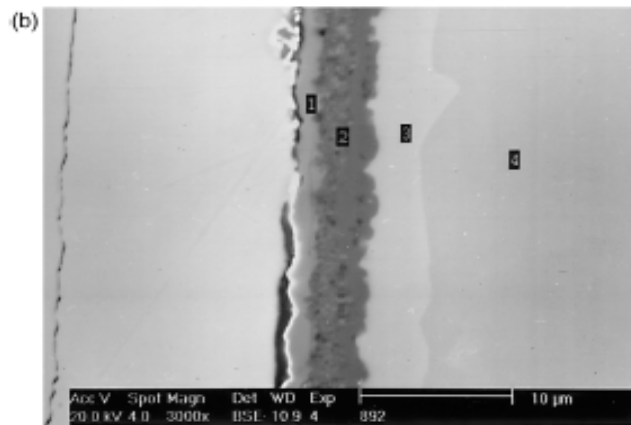


Figure 3.1.2b Ti48Al1.5Cr alloy with chlorine implantation (400 KeV) after 100h of oxidation at 900 °C

Fig 3.2c : Implantation dose was $2.5 \cdot 10^{16}$ B ions/cm² with 1.9 MeV energy.

Fig 3.2d : Implantation dose was 10^{16} I ions/cm² with 2.6 MeV energy

Oxidation conditions are 100h at 900 °C, in both cases.

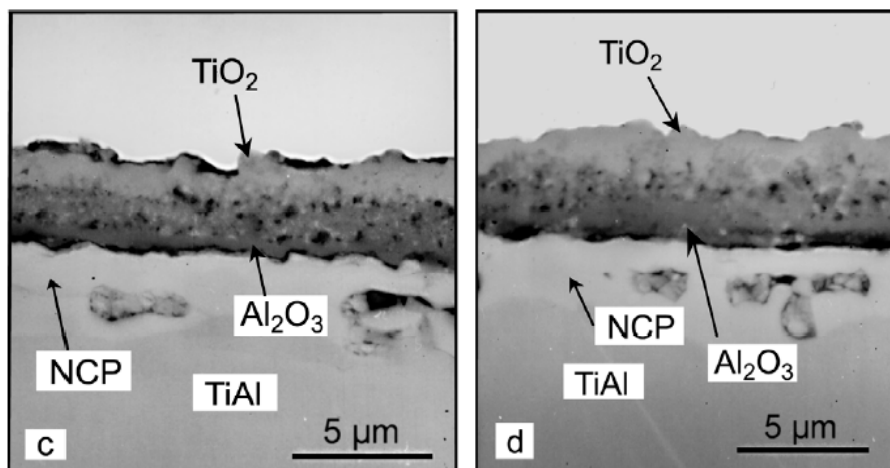


Figure 3.1.2 d and 3.1.2c Scale cross section of an bromine implanted sample (d) and of an iodine implanted sample (c)

Other experiments demonstrated that fluorine ion implantation reduces the oxidation resistance due the higher fraction of titania formed in the scale.

The effect of energy implantation is shown in Fig 3.3.

If the implantation energy is too high then the implanted species is shifted deeper in the alloy and cannot develop its microalloying effect .

The implanted dose is equal to 10^{16} Cl ions/cm²

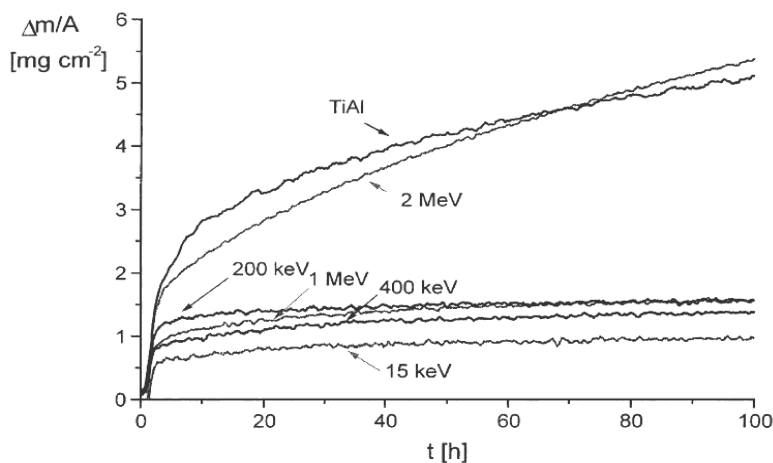


Figure 3.1.3 Effect on oxidation behaviour of the implantation energy

Varying the implantation dose at a fixed implantation energy has two types of effects: the first is that a lower threshold exist which must be exceeded in order to activate positive microalloying effect; The second is that if this threshold is exceeded the dose has an influence on the “incubation period”. Evidently a optimum dose range exist.

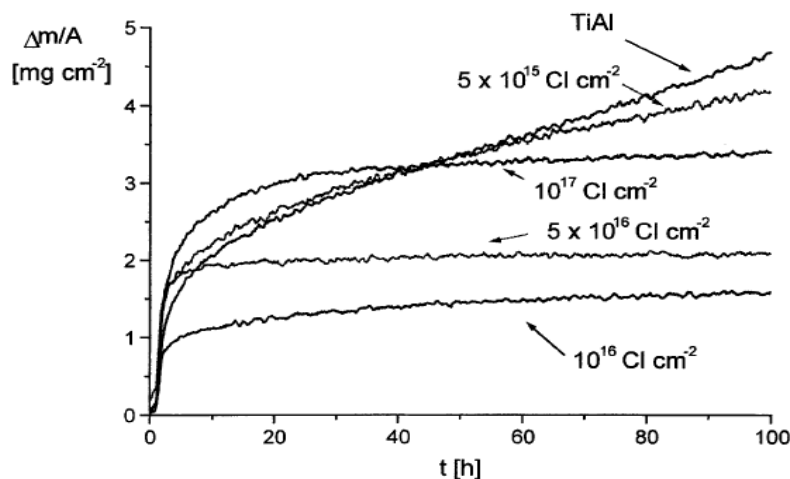


Figure 3.1.4 Weight change during oxidation versus implantation dose

However, with increasing oxidation time chlorine may diffuse into the bulk or some may even evaporate through fissures in the oxide scale so that the chlorine concentration in the metal subsurface zone drops down to optimum values.

The optimum doping condition were found for the two tested alloys (described in Table 3.1.1). Oxidation result are displayed in figure 3.1.5

Form these findings it can be concluded that there must be a synergistic effect even of the macroscopic alloying elements and the halogen ions introduced by ion implantation

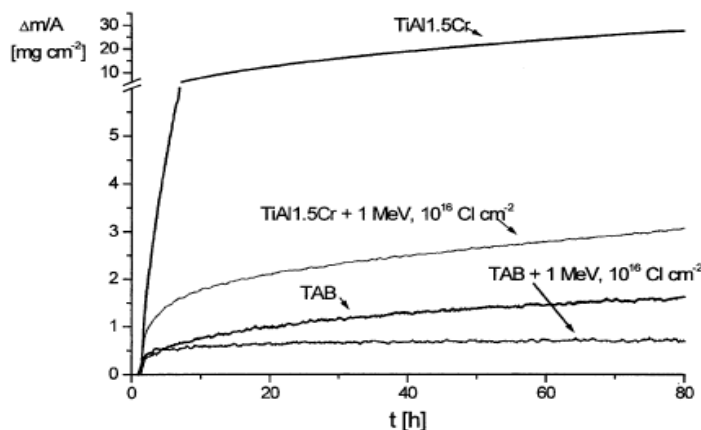


Figure 3.1.5 Effect of chlorine implantation on different substrates

Comparing a specimen with the optimum implantation parameters with the oxidation behaviour of unimplanted titanium aluminide shows that at 800 °C the parabolic constant fall into one common scatter band which is not so far away from the oxidation behaviour of pure titanium, as shown in figure 3.1.6.

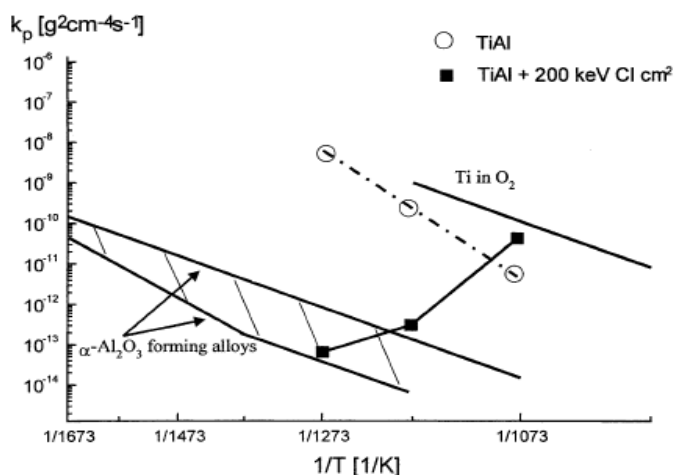


Figure 3.1.6 Kp values of ion implanted TiAl alloy and the typical corresponding values for alumina forming materials

Increasing the temperature to 900 °C , however , shifts the value for the parabolic rate constant to the edge of the scatter band for alumina formers .

Increasing the temperature to 1000 °C lowers the parabolic rate constant to a value which is very close to the lower edge of the scatter band for alumina formers.

The reason for this behaviour was explained by the different temperature dependencies of the volatility of titanium chlorides and aluminium chlorides.

At elevated temperatures most of the metal chlorides develop high vapour pressures and, thus , are present in gas phase.

Fig 3.1.7 shows the interdependence of the metal chloride partial pressures together with the chlorine partial pressure for the situation at the oxide interface , i.e. $p_{O_2} = 10^{-37}$ bar as the equilibrium partial pressure of Al_2O_3 and Al and Ti activities corresponding to stoichiometric TiAl.

In the positive effect zone the partial pressure of AlCl is orders of magnitudes greater than that the next volatile titanium chloride ($TiCl_3$).

In this condition Al will selectively be removed from the alloy to form a volatile AlCl compound.

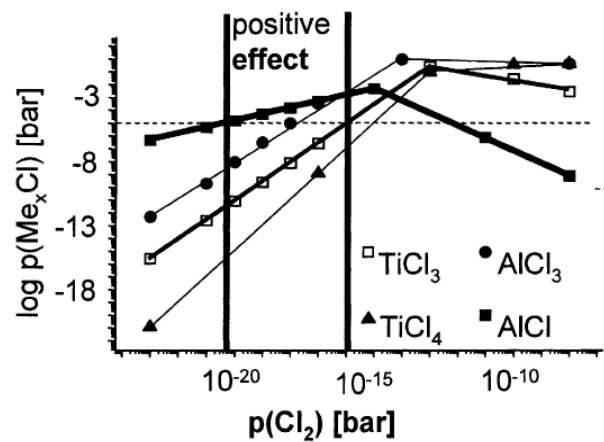
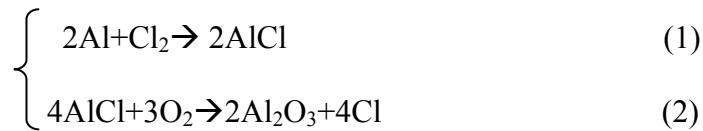
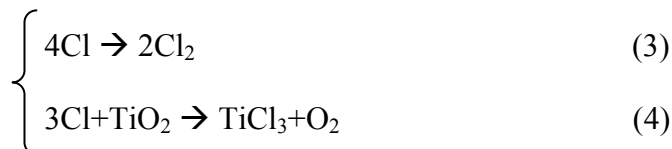


Figure 3.1.7 Optimum partial pressure of chlorine for the alumina formation

If oxygen is present then these reaction will occur:



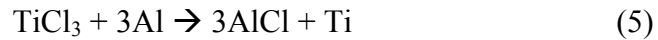
This means if the oxygen partial pressure reaches a certain value the AlCl becomes oxidized and forms solid Al_2O_3 . The chlorine released can either form molecular chlorine gas (3) or react with TiO_2 (4)



AlCl will be converted to Al_2O_3 at much lower p_{O_2} values than $TiCl_3$ to TiO_2 .

Therefore reaction (2) and (4) can occur in the same region of oxide scale (close to the oxide/ metal interface) . Thus , solid TiO_2 is converted into gaseous $TiCl_3$ while gaseous AlCl precipitates as solid Al_2O_3 .

As a consequence a continuous protective Al_2O_3 layer is established underneath outer TiO_2 layer . TiCl_3 can support this mechanism by reactions with the TiAl substrate



AlCl reacts according to reaction (2)

Since there is a very steep oxygen partial pressure gradient over the oxide scale all metal chlorides which diffuse through microcracks or fissures into the inner part of the scale in outward direction soon come into areas of increased oxygen partial pressure leading to reaction (2).

With increasing oxygen partial pressure an alumina diffusion barrier is formed which decreases the oxidation rate to alumina kinetics.

At very low values the chlorine partial pressure is not high enough to evaporate a substantial amount of metal via chloride formation. So in this case no positive effect in the form of alumina precipitation in the inner part of the oxide scale can be expected.

If the partial pressures of the aluminium and the titanium chloride exceed the critical value of 10^{-5} bar then both species , i.e. titanium and aluminium can be evaporated at the same time and at similar amount so that no selective transport and precipitation of alumina is possible.

Since in this case both oxides will be precipitated in the inner part of the oxide scale a mixture of oxides will be present similarly to the case without any chlorine effect. The results of these considerations can be summarized as follows:

- Negative chlorine effect ,i.e. the chlorine concentration is too high and an oxide mixture $\text{Al}_2\text{O}_3 - \text{TiO}_2$ is formed
- Positive chlorine effect, i.e. the chlorine concentration lies in a window where pure alumina is formed
- No chlorine effect , i.e. the chlorine concentration is too low and the usual mixture $\text{Al}_2\text{O}_3 - \text{TiO}_2$ is formed as on unimplanted material

The same type of thermodynamic calculation can be performed with bromine and iodine; The result of these calculations are shown in figure 3.1.8.

In all cases the situation is similar to chlorine case.

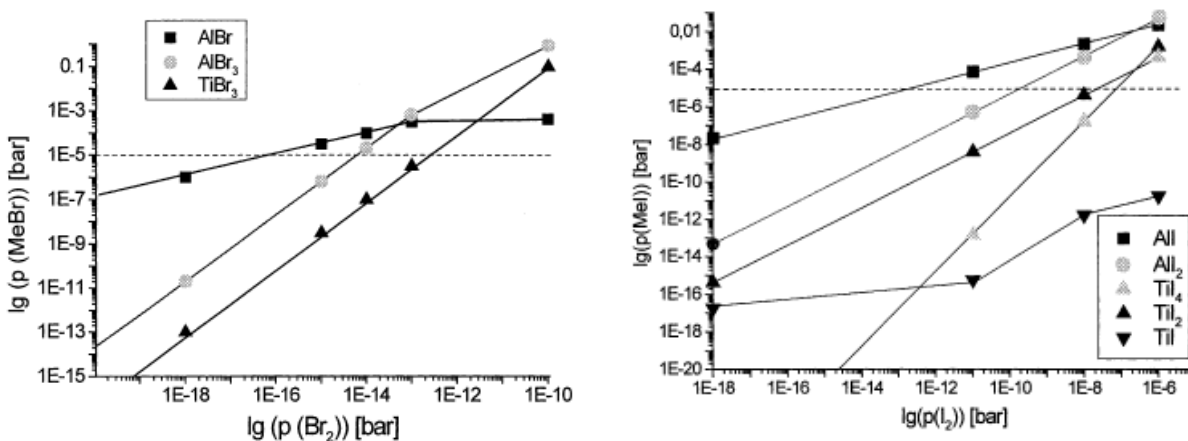


Figure 3.1. 8 Partial pressure of the volatile metallic halide versus the corresponding halogen (bromine/left and iodine/right)

3.2 NiAl COATINGS [10] [11]

A nickel aluminide coating, developed on γ -TiAl alloy by electroplating a Ni film followed by a high Al activity pack cementation, has a duplex layer structure with an outer δ -Ni₂Al₃ layer and an inner TiAl₃/TiAl₂/TiNiAl₂ layer. The coated γ -TiAl was oxidized in air for up to 10000 h under thermal cycling between room temperature and 1173 K. A protective Al₂O₃ scale formed with little oxide exfoliation and the average oxidation amount was 37 g/m² after the 10000 h oxidation. During oxidation at 1173 K the outer δ -Ni₂Al₃ changed to β -NiAl with voids and then to TiNiAl₂, and the inner TiAl₃/TiAl₂/TiNiAl₂ layers to TiAl₂ and TiNiAl₂ layers and then to TiAl₂ and τ 3 layers. The voids in the outer layer were formed by the phase transformation from the δ -Ni₂Al₃ to β -NiAl during oxidation. It was found that after the 10000 h oxidation the higher Al contents in the inner layers were better retained than that in the outer layer.

A Ti-50at%Al alloy was prepared from pure metals, Ti sponge (99.5% purity) and Al (99.99% purity), using Ar-arc melting, and the cylindrical ingot obtained was heated in a vacuum at 1373 K for 9h. A 1 mm thick specimen with a surface area of about 2 cm² was cut from the cylindrical ingot. The specimen surface was polished with abrasive paper #400 and then cleaned ultrasonically in a methanol and benzene solution.

The coating was formed on the γ -TiAl alloy, by electroplating of Ni followed by an Al-pack cementation. A Ni film of about 10 nm thickness was electroplated on the γ -TiAl in a Watt's solution at a bath temperature of 328 K for 2h with a current density of 5 mA/cm². The high Al activity pack cementation was carried out by burying the Ni plated γ -TiAl in a mixture of Al metal powder (15 mass%), NH₄Cl (10 mass%) as an activator, and Al₂O₃ powder (75 mass%) as an anti-sintering agent at 1273 K for 5h.

Fig. 3.2.1(a) and 3.2.1(b) show the cross-sectional microstructure and concentration profiles of Al, Ti, and Ni for the as coated γ -TiAl alloy. The coating has at least six-layers:

(1) Ni₂Al₃, (2) TiNiAl₂, (3) and (5) TiAl₃, (5) L1₂-Ti(Al,Ni)₃, and (6) TiAl₂ in the number sequence from the surface.

Both the TiAl₂ and TiAl₃ contain little Ni, less than 1 at%. It is noteworthy that the Ti content of the outer δ -Ni₂Al₃ layer was negligible, as shown in Fig. 1(b). Further, the Al

content of the inner layer was much higher than 60 at %Al in the outer δ -Ni₂Al₃ layer.

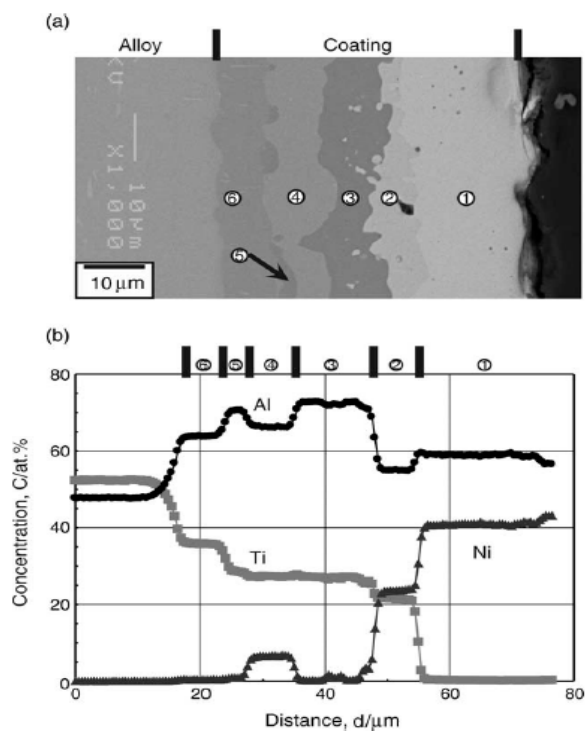


Figure 3.2.1(a) , 3.2.1(b) - Cross-sectional microstructure (a) and concentration profiles (b) of Ti, Al, and Ni for the Ni-Al coated TiAl alloy.

Fig. 3.2.2 and Fig 3.2.3 show the results after oxidation for 1000 h. It was found that the coating changed to a three layer structure from the six layers before oxidation (Fig. 3.2.1(a) – Fig 3.2.1(b)).

The three layers are an inner $TiAl_2$ layer, an intermediate $TiNiAl_2$ layer, and an outer $\beta-NiAl$ layer containing voids.

The voids may have been formed by phase transformation from $\delta-Ni_2Al_3$ to $\delta-NiAl$, accompanied by a volume reduction.

Fig. 3.2.3 and 3.2.4 show the results after oxidation for 3000 h . The outermost layer (1) appears to be a τ_3 phase with a composition of $Ti-44Al-19Ni$, although this is not certain because the layer is very thin. The outer and intermediate layers (2) and (3) and are $\beta-NiAl$ and $TiNiAl_2$.

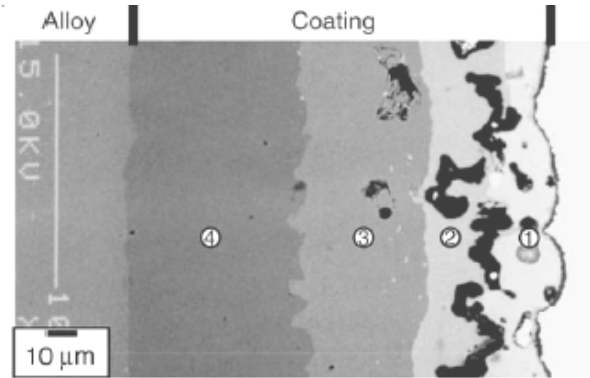


Figure 3.2.2-Coating evolution after 1000 h of oxidation at 900 °C in air

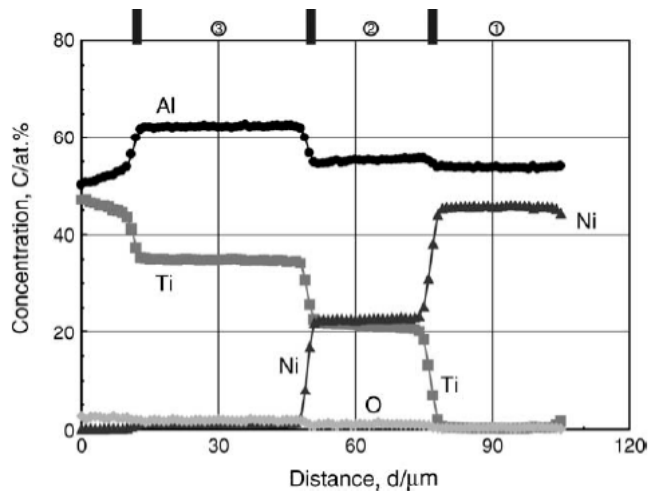


Figure 3.2.3 Concentration profiles of the coated layer after 1000 h of oxidation at 900 °C in air

A part of the $L1_2-Ti(Al,Ni)_3$ layer has decomposed to $TiAl_2$ and $TiNiAl_2$ phases, forming layer (4) . The inner $TiAl_2$ layer is thicker, 70 μm after 2000 h oxidation and 100 μm after 3000 h of oxidation. The voids tend to interconnect (Fig 3.2.4)

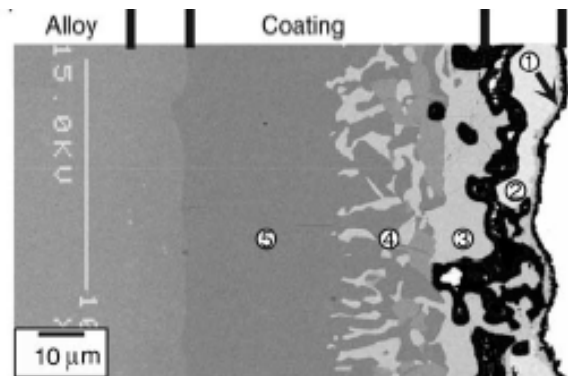


Figure 3.2.3 Coated layer appearance after 3000 h of oxidation at 900 °C in

After oxidation of the specimen 4000 h as shown in Fig 3.2.4 the coating structure remained similar to that after 3000 h oxidation in Fig. 3.2.3 except that the $L1_2$ -Ti(Al,Ni)₃ layer had disappeared and TiAl₂ layer is slightly thinner.

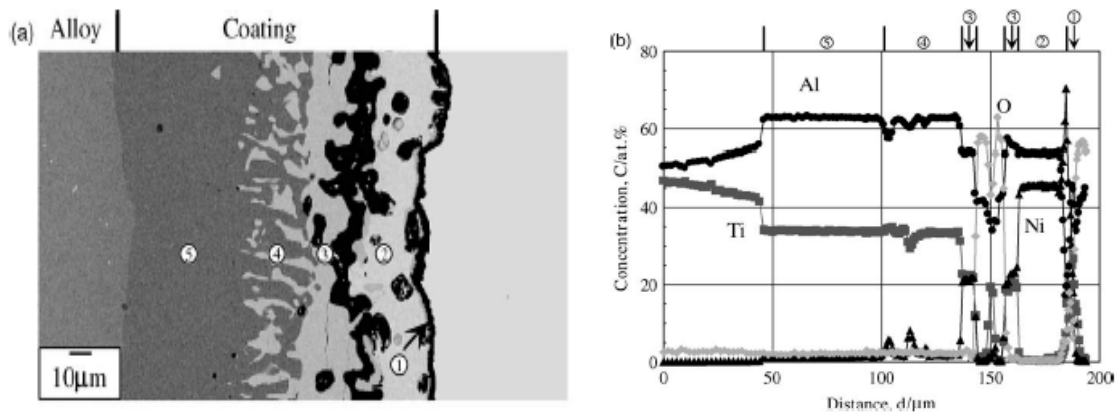


Figure 3.2.4 – Coated layer appearance and concentration profiles after 4000h of oxidation at 900 °C in air

With further oxidation to 10000h, as shown in Fig 3.2.5 a α -Al₂O₃ scale had formed without exfoliation, and the coating consisted of three layers, an outer layer (1) of TiNiAl₂ (including β -NiAl (2)), an intermediate layer (3) of τ_3 , and an inner layer (4) of TiAl₂. while the τ_3 layer thickness had increase, the TiAl₂ layer was thinner, about 30 nm.

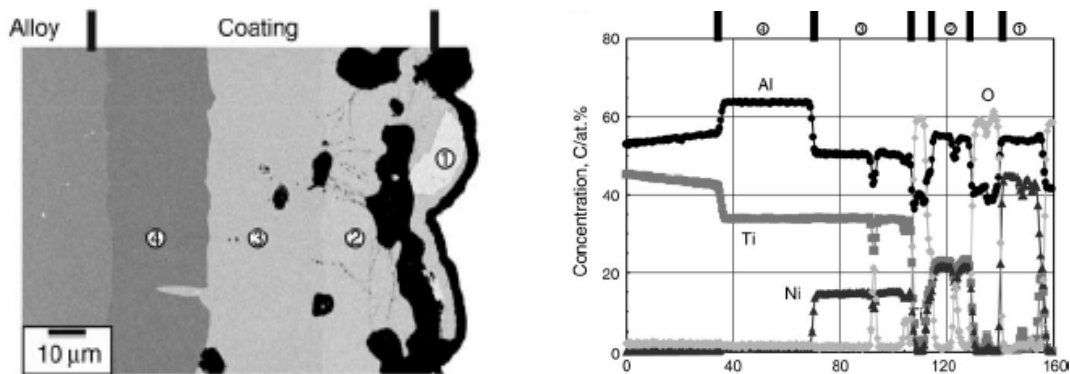


Figure 3.2.5 – Coated layer appearance and concentration profiles after 10000 h of oxidation at 900 °C in air

The results test are summarized in Fig 3.2.6.

All the oxidation test are performed in air at 900 °C under atmospheric pressure.

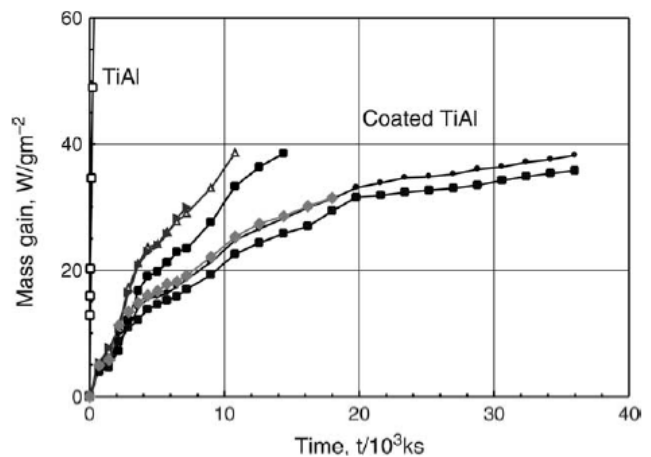


Figure 3.2.6 -Results summary of the oxidation test of the coated alloy versus the uncoated material

3.3 EFFECT OF ALLOYING ELEMENTS ON OXIDATION RESISTANCE ^[12]

As shown in Fig 3.3.1 The additions of Mo,Si and Nb with the order of 5% improved resistance of TiAl alloys for the isothermal condition at elevated temperature under atmospheric environment.

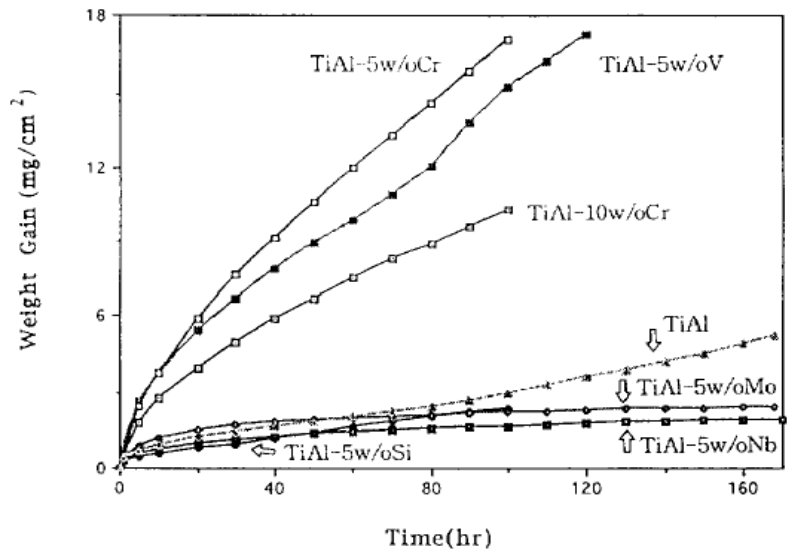


Figure 3.3.1 Oxidation behaviour modification after various ternary additions (Cr,V,Nb,Mo,Si)

In the Fig 3.3.2 (a) and Fig 3.3.2 (b) in displayed the oxidation behaviour for two alloys with Si and Nb additions: the effect of the two elements on oxidation were quite different; crystalline and/or amorphous SiO₂ in the oxide layer was formed by the addition of Si , which acted as a barrier against oxidation.

Nb enhanced the formation of Al₂O₃ and changed the structure of the diffusion barrier against oxidation. The TiO₂/Al₂O₃/Nb₂O₅ layer was also protective .

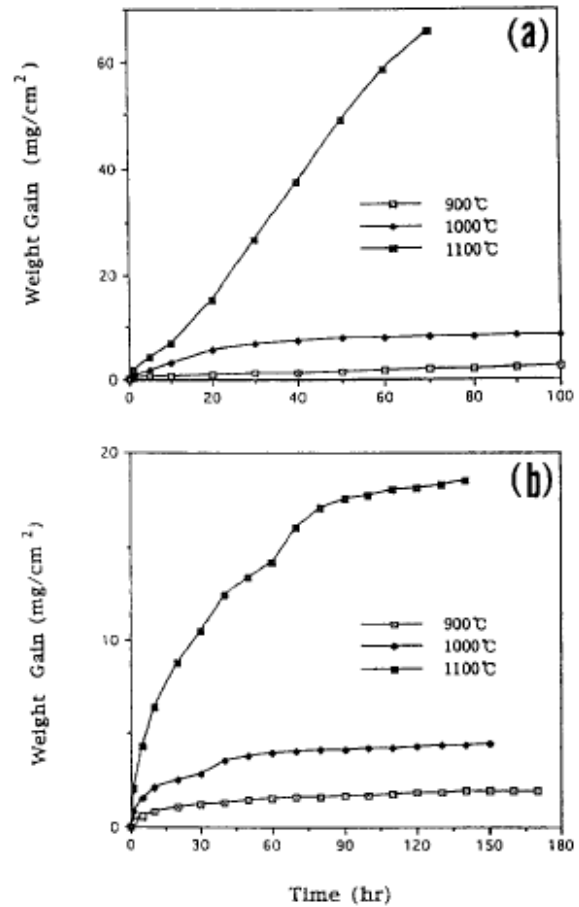


Figure 3.3.2(a) and 3.3.2(b) - Weight change per unit area for TiAl-5wt%Si (a) and TiAl-5wt%Nb (b) at various temperatures

In Fig 3.3.3 the cyclical oxidation behaviour is displayed : the best effect is developed by Nb addition.

It's very remarkable that Cr addition in this case (and whit isothermal oxidation) leads to a decreased oxidation resistance.

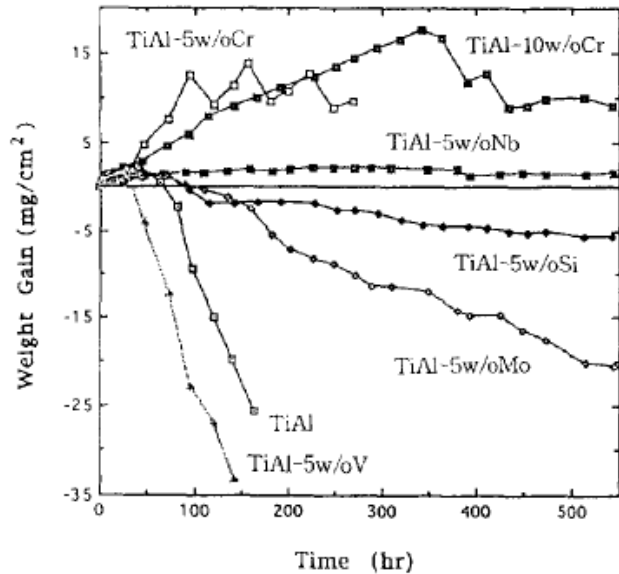


Figure 3.3.3 - Oxidation behaviour with cyclical oxidation at 900 °C for various alloys

The following three mechanism can be derived as guidelines for a good alloying element determination^[13]

- **Valence – control rule** If the formation of TiO_2 were suppressed or minimised , the the situation becomes more favourable to form an Al_2O_3 rich or Al_2O_3 scale. For this purpose the valence control rule (VCR) (or Wagner Hauffe rule is applicable. TiO_2 grows mainly by the oxygen diffusion of oxygen via oxygen vacancies in it. Therefore , additional element that can decrease the oxygen vacancies in TiO_2 are very effective to decrease the overall oxidation rate. Of course , their solubility in TiO_2 and their valence state should be known.
- **Wagner'scaling model** The suppression of internal oxidation of Al to form discrete Al_2O_3 platelets in the substrate is also effective to make a continuous Al_2O_3 layer on the specimen surface
The criterion for the transition from internal to external scaling was given by Wagner^[35,36] and is shown Eq 3.3.1 for the formation of an Al_2O_3 scale on TiAl

$$N_{Al} > \left(\frac{\pi g}{3} * N_o * \frac{D_o V_M}{D_{Al} V_{OX}} \right)^{0.5} \quad \text{Eq 3.3.1}$$

Where N_{Al} is the Al content , N_o is oxygen solubility in the substrate ; D_{Al} and D_o are diffusivities of Al and oxygen ,respectively.

V_M and V_{OX} are volumes of TiAl and Al_2O_3 per mole of Al , respectively.

“g” is a conversion factor from internal to external oxidation.

- **Formation of a barrier layer** a small addition of Si was reported^[37,38,39] to be effective in decreasing the oxidation rate by forming discrete SiO_2 aggregates in the scale near the

scale / substrate interface . The SiO_2 rich layer can work as barrier to some extent. As a result of this , Al_2O_3 is enriched near the interface and this will further contribute to decrease the oxidation rate. Similar effect is developed by Mo and Nb additions. It's remarkable that before the mechanism becomes effective a large amount of added element is consumed.

Fig 3.3.4 shows the effect of additional elements on the mass gain during oxidation.

According to the valence rule the elements that can replace Ti ions in TiO_2 as cations having a valence smaller than four will increase the oxidation rate and vice-versa. This mechanism is applicable to 2Cu, 1Y, 1.5Cr, 1.5Mn.

Regarding group V and VI elements , very small additions of P, Se and Te are effective to decrease the oxidation rate.

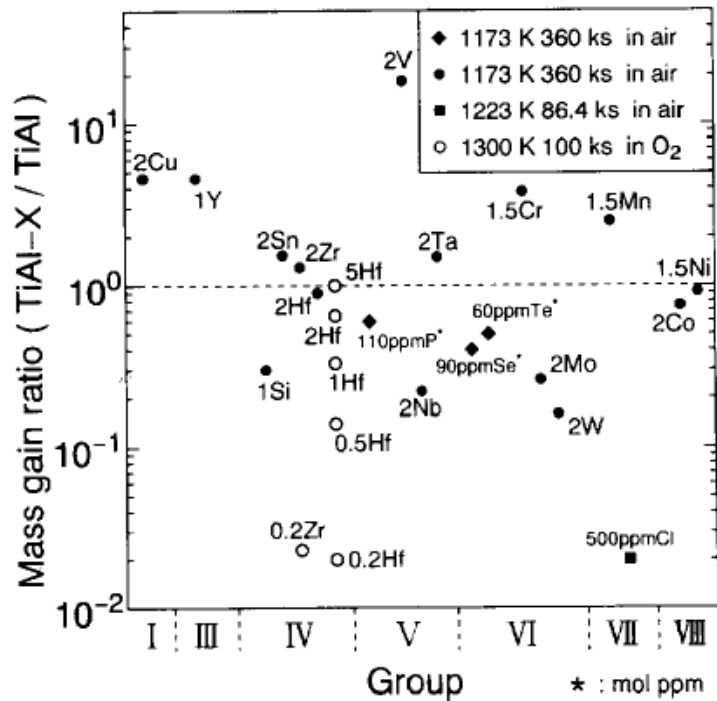


Figure 3.3.4 - effect of additional elements on the mass gain during oxidation.

The oxidation rate reduction due Mo addition is to attribute to its oxygen solubility reduction effect. For Hf addition an optimum concentration should be exist.

3.4 TWO STEP Cr - Al DIFFUSION COATING ON TiAl AT HIGH TEMPERATURE ^[14]

The formation of an oxidation resistive coating layer on a TiAl alloy was investigated with a two-step Cr (at 1573 K for up to 20h) and then Al (at temperatures between 1273 and 1573 K for 10h) pack diffusion process at high temperatures. The coated TiAl was oxidized in air at 1173 K for up to 350h under a thermal cycling condition. The Cr diffusion coating layer consisted of γ , β , and Laves phases, which were transformed during cooling from the β -phase formed at 1573 K. The coating layer formed by the Al diffusion at 1473 and 1573 K consisted of an outermost TiAl_2 , outer Al-rich γTiAl , intermediate γ , β , and Laves phases, and a diffusion zone; there is little Al-diffusion at 1273 and 1373 K. The TiAl coated by the two-step Cr and Al diffusion process at 1573 K showed very good oxidation resistance in air at 1173 K due to the formation of a protective $\alpha\text{-Al}_2\text{O}_3$ scale. After oxidation for up to 350h the coating layer maintained a structure with three phases γ , Laves, and β , which acts as a diffusion barrier to Al and Ti

A Ti-50 at.%Al alloy was prepared by Ar-arc melting from Al metal with 99.99% purity and Ti sponge with a nominal purity of 99.7%, which had been re-melted prior to use for alloy preparation. The melting and casting process was repeated several times to make the alloy composition homogeneous. The alloy ingot was heat-treated in a vacuum (4×10^{-3} Pa) at 1373 K for 9h and 1 mm thick specimens were cut. After drilling a 1.5 mm diameter suspension hole the specimens were polished with water proof emery papers down to grit 1200 and then washed in a methanol–benzene solution under ultra-sonic agitation.

A conventional pack cementation method was used in the present experiment. The TiAl specimen was embedded into an Al_2O_3 container with a mixture of Cr or Al vapour source and Al_2O_3 powder as an anti-sintering agent. The container was heated in a vacuum of 10^3 Pa with a heating rate 0.167 K/s to set temperatures between 1273 and 1573 K, and after keeping it for various times at the temperature the furnace was turned off and left to cool to room temperature. Pulverized Cr metal and TiAl3 alloy were used as the Cr vapour and Al vapour sources, respectively. The Cr pack diffusion was mainly carried out at 1573 K for various times, and after polishing the Cr coated specimen slightly the Al pack diffusion was performed at temperatures between 1273 and 1573 K for 10h. The mass gain of the TiAl alloy specimen was determined from the weights before and after each pack cementation, and the mass change per unit surface area was determined.

Oxidation tests were carried out in air at 1173 K under a thermal cycling condition. The coated specimen was suspended with a platinum wire in an Al_2O_3 crucible ,and the crucible was put in the furnace and heated to 1173 K at a heating rate of 0.167 K/s. After keeping for 24h (the first cycle was 12h) at 1173 K the furnace was turned-off to cool down to room temperature.

The mass change of specimens and exfoliated oxides were measured using a balance with 0.01 mg accuracy at room temperature.

Fig 3.4.1 shows the microstructure after pack diffusion treatment at 1573 K after various treatment times.

(1) indicates an outer layer, (2) the intermetallic layer, (3) a interdiffusion zone and ⊗ the precipitates

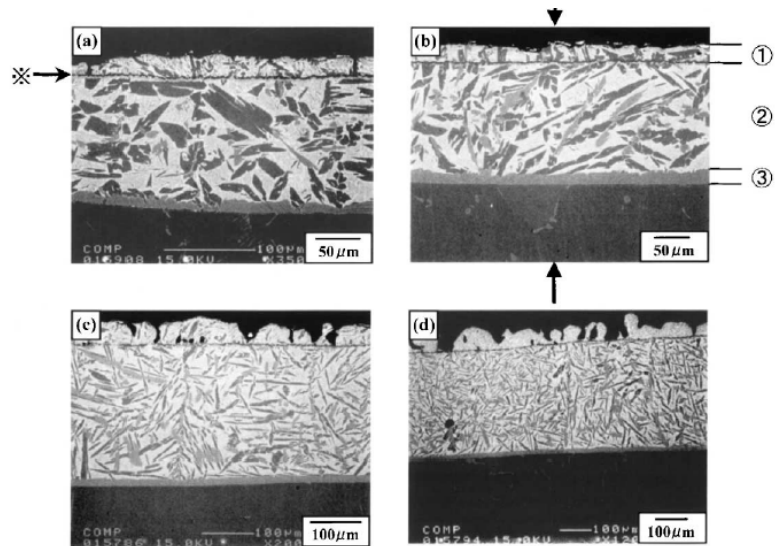


Fig 3.4.1 cross sectional microstructures of the TiAl alloy after the Cr pack diffusion treatment at 1573 K for different times: (a) 2h , (b) 5h, (c) 10h , (d) 20h.

In Fig 3.4.2 (1) indicates an outermost layer, (2) an outer layer, (3) an intermediate layer, and (4) a diffusion zone.

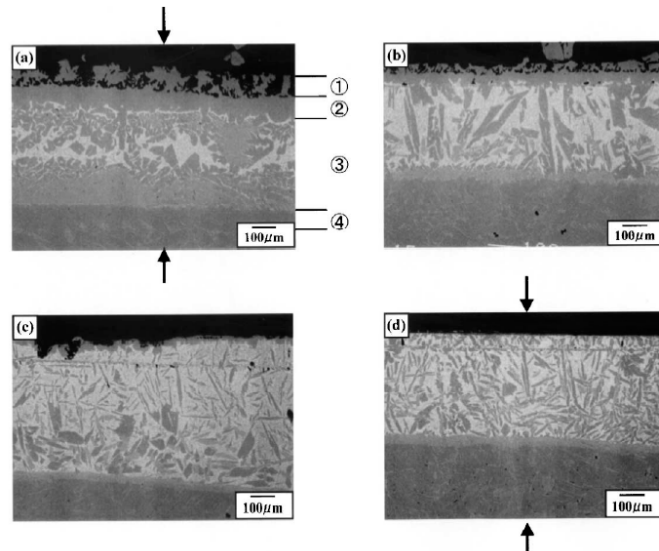


Fig 3.4.2 - Cross sectional microstructures of the TiAl alloy after the Al pack diffusion treatment up to 10h at different temperatures : (a) 1273 , (b) 1373 , (c) 1473 , (d) 1573 ,

The cross sections of the coating layer can be approximately divided into two groups, group A at 1273 and 1373 K, and group B at 1473 and 1573 K. The microstructure of the coating in group A was similar to that shown in Fig. 3.4.2 (b), after only the Cr-diffusion treatment, although the structure became more complex and the line precipitates still exist.

While in group B the outermost and outer layers, and , were newly formed on the intermediate layer, and the line precipitate of α_2 - Ti_3Al had disappeared. Irregular shapes characterized the outermost layer, and the intermediate layer contains relatively large precipitates. A diffusion zone grew between the intermediate layer and alloy substrate.

Fig. 3.4.3 shows changes in mass gain with oxidation time at 1173 K in air under a thermal cycling condition for the TiAl alloy, which was first Cr diffusion treated at 1573 K for 5h, followed by an Al diffusion treatment for 10h at different temperatures.

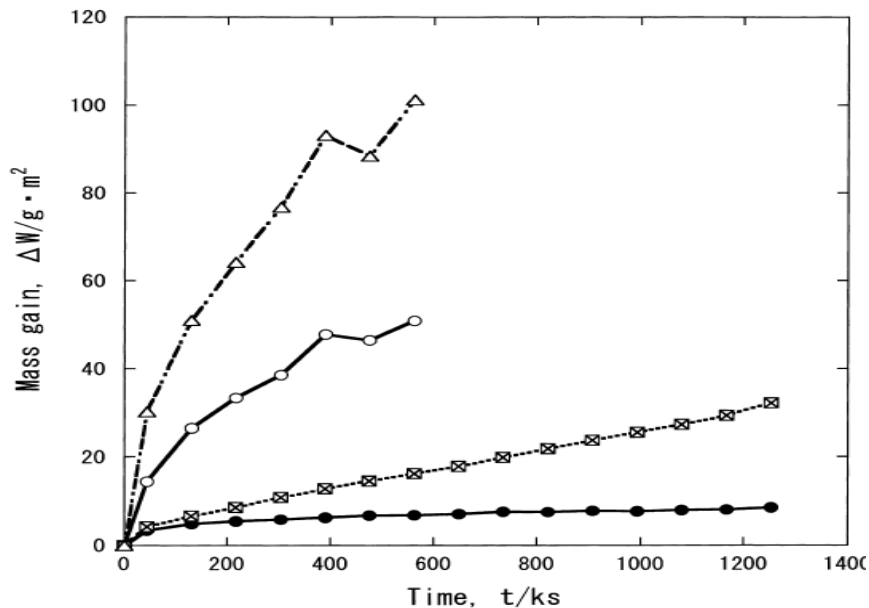


Fig. 3.4.3 - Changes in mass gain with oxidation time at 1173 K in air. Al-diffusion temperatures are 1573 K (●), 1473 K (■), 1373 K (○), and 1273 K (▲)

Fig. 3.4.4(a) and 3.4.4 (b) show cross-sectional microstructures of the TiAl after oxidation at 1173 K for 160 and 347 h, respectively, where the TiAl in Fig. x(a) was treated by the Cr diffusion at 1573 K followed by the Al-diffusion at 1573 K and the TiAl in Fig. x(b) by the Cr diffusion at 1573 K followed by the Al diffusion at 1273 K.

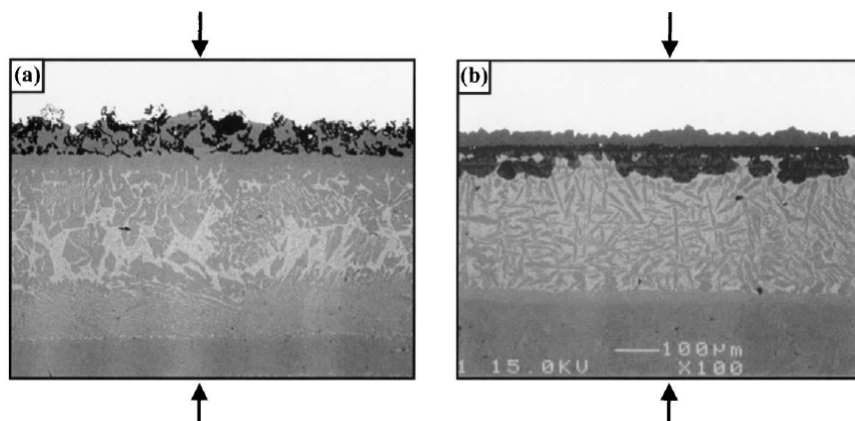


Fig. 3.4.4(a) 3.4.4(b) . Cross-sectional microstructures of the coated TiAl alloy after oxidation at 1173 K. Al-diffusion temperatures and oxidation times are (a) 1573 K for 350h and (b) 1273 K for 155h.

As shown in Fig. 3.4.4 (a), oxide formed on the coating surface, accompanied with an embedded oxide within the outermost layer. The nodules covered by an external scale intruded into the coating layer, as shown in Fig. 3.4.4 (b).

3.5 LONG TERM OXIDATION PROPERTIES OF AL-TI-CR TWO PHASE ALLOYS AS COATING MATERIALS FOR TiAl ALLOYS ^[15]

Both Al-21Ti-23Cr ($L_{12}+Cr_2Al$) and Al-37Ti-12Cr ($\gamma+TiAlCr$) two-phase alloys have been accepted as the most appropriate coating materials in the Al-Ti-Cr alloy system to improve the high-temperature oxidation resistance of TiAl alloy, taking into consideration their oxidation resistance, resistance to thermal stress, and chemical compatibility with TiAl alloys. In this study, thermal stress analyses were performed on the basis of the thermal expansion coefficient and tensile and compressive strength of coating and substrate materials. Also the reaction properties between the alloys of interest in this paper and TiAl substrate were studied by bonding the two materials. This elucidates the long-term oxidation properties in L_{12} -based and γ -based alloys. There was no significant difference in short-term oxidation resistance between the L_{12} -based and γ -based alloys because both alloys could form a stable Al_2O_3 layer. However, although both alloys show similar resistance to thermal stress, it was confirmed that the L_{12} -based two-phase alloy has much better oxidation properties than the γ -based two-phase alloy in long-term oxidation as it is considering the interface reaction properties with TiAl alloy.

To protect the substrate effectively in the air, the coating material should be selected by considering not only the oxidation properties but also the resistance to thermal stress and chemical compatibility with the substrate. This accelerates studies on L_{12} -based and γ -based alloys in the Al-Ti-Cr alloy system as coating materials for the TiAl alloy [16]. Because the L_{12} single phase has a very porous microstructure and the γ single phase is not capable of forming a protective Al_2O_3 scale when exposed to the air above 800 °C, it is desirable to adopt both L_{12} -based and γ -based alloys as two-phase alloys of $L_{12}+Cr_2Al$ [16,17] and $\gamma +TiAlCr$ [17] respectively.

Many studies were performed for the application of L_{12} -based and γ -based two-phase alloys as coating materials for TiAl, and showed that these coating materials were very effective in improving the oxidation properties of the TiAl alloy [17,18].

Although a lot of works on Al-Ti-Cr coating provided the key to enhancing their poor oxidation properties above 800 °C, their practical application has not yet been approved because not much is known about their long-term oxidation properties, and in particular, the changes of performance and reliability after long term exposure to high temperature. The difference in composition between coating and substrate results in diffusion at the coating/substrate interface, and this consequently widens the diffusion layer in the coating layer. Therefore, the diffusion layer plays a more dominant role in the long-term oxidation properties, and it might be possible to infer long-term oxidation properties through studying the diffusion layer.

Long-term oxidation properties of L_{12} -based and γ -based coating materials were investigated by bonding the Ti-48Al alloy with the Al-21Ti-23Cr ($L_{12}+Cr_2Al$) two-phase alloy and the Al-37Ti-12Cr ($\gamma+TiAlCr$) two-phase alloy and observing the resulting diffusion layer. Additionally, the microstructures and oxidation properties of the diffusion layer were also studied.

The Ti-48Al alloy was bonded with Al-21Ti-23Cr alloy and Al-37Ti-12Cr alloy, respectively, using a spark plasma sinterer (denoted as SPS henceforth) at 1000 °C for 5 min. Then, these bonded alloys were held at 1000 °C for 100 h to investigate interface properties and the diffusion layer. Additionally, the Al-39Ti-5Cr alloy and Al-47Ti-3Cr alloys, which formed at the Ti-48Al alloy/Al-21Ti-23Cr alloy interface and at the Ti-48Al alloy/Al-37Ti-12Cr alloy interface, respectively, were exposed isothermally at 1000 °C to get more information on oxidation properties of the diffusion layer in each alloy.

Oxidation properties of L₁₂-based and γ -based two phase alloys

An isothermal oxidation test was performed at 1000 °C to compare short-term oxidation properties for L₁₂-based two-phase (Al-21Ti-23Cr) and γ -based two phase (Al-37Ti-12Cr) alloys at the bulk state. Fig. 3.5.1 shows the oxidation kinetics at 1000 °C for the Ti-48Al, Al-21Ti-23Cr, and Al-37Ti-12Cr alloys.

When the L₁₂-based two-phase and γ -based two-phase alloys were exposed to air at the bulk state, both of them showed a very small change in the mass gain as compared to the Ti-48Al alloy, but the difference in a mass gain between the two alloys was not observed. It was also reported that the TiAl alloy with the surface coating of L₁₂-based alloy and γ -based alloy led to the drastic reduction of a mass gain during oxidation through protecting the TiAl substrate effectively in the air [5-7].

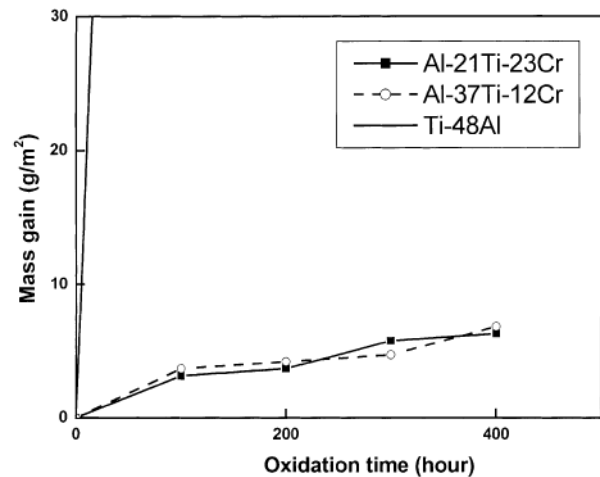


Figure 3.5.1- Oxidation behaviour at 1000 °C of Ti48Al and two AlTiCr alloys

This clearly shows that both the L₁₂-based two-phase and γ -based two phase alloys exhibited remarkable oxidation resistances not only at the bulk state but also at the thin-film state.

The Ti-48Al alloy was bonded with the L₁₂-based two-phase (Al-21Ti-23Cr) and γ -based two-phase (Al-37Ti-12Cr) alloys using SPS at 1000 °C and then held at 1000 °C for 100 h. Fig. 3.5.2 shows cross-section microstructures at the interface between the Ti-48Al alloy and each coating material.

It was found that the difference in composition between the Ti-48Al alloy and the coating materials caused the formation of a diffusion layer at the interface.

A composition analysis on the centre of the diffusion layer using EDS revealed that the diffusion layer between the Ti-48Al alloy and L₁₂-based two-phase alloy had a composition of Al-39Ti-5Cr, and the diffusion layer between Ti-48Al alloy and γ -based two-phase alloy had a composition of Al-47Ti-3Cr.

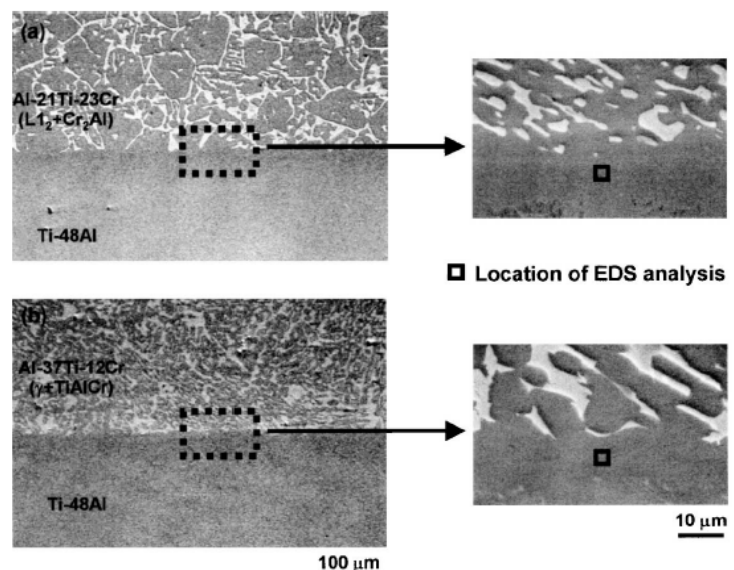


Figure 3.5.2 -Formation of a diffusion zone between and substrate

The diffusion layer could play an important role as a barrier to prohibit oxygen diffusion into the substrate, especially when the alloy was held to a long term exposure. Thus, to get more information on the oxidation properties of the diffusion layer, an oxidation test was performed for the Al-39Ti-5Cr and Al-47Ti-3Cr alloys.

Fig. 3.5.3 shows the oxidation kinetics at 1000 °C for the Al-39Ti-5Cr and Al-47Ti-3Cr alloys, corresponding to the composition of the diffusion layers between the Ti-48Al alloy and the L₁₂-based two-phase alloy and between the Ti-48Al alloy and γ -based two phase alloy respectively.

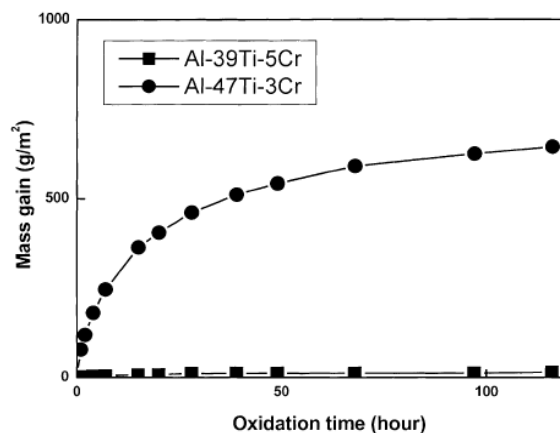


Figure 3.5.3 -Great influence of the chrome content on to the oxidation properties

As seen in the Fig 3.5.3 , the Al-39Ti-5Cr alloy shows better isothermal oxidation resistance than the Al-47Ti-3Cr alloy. Therefore, it is elucidated that the diffusion layer between the Ti-48Al alloy and the L₁₂-based two-phase alloy reveals better oxidation resistance.

Fig. 3.5.4 shows the results of XRD analysis for the Al-39Ti-5Cr and Al-47Ti-3Cr alloys after exposure at 1000 °C for 100 h. The XRD analysis confirmed the oxidation layer for the Al-39Ti-5Cr alloy and for the Al-47Ti-3Cr alloy consisted of Al₂O₃ and TiO₂ and rather pure TiO₂ respectively.

It was found that the diffusion layers of the two specimens were extended to about 10 μ m during holding at 1000 °C for 100 h through composition analysis at the interface.

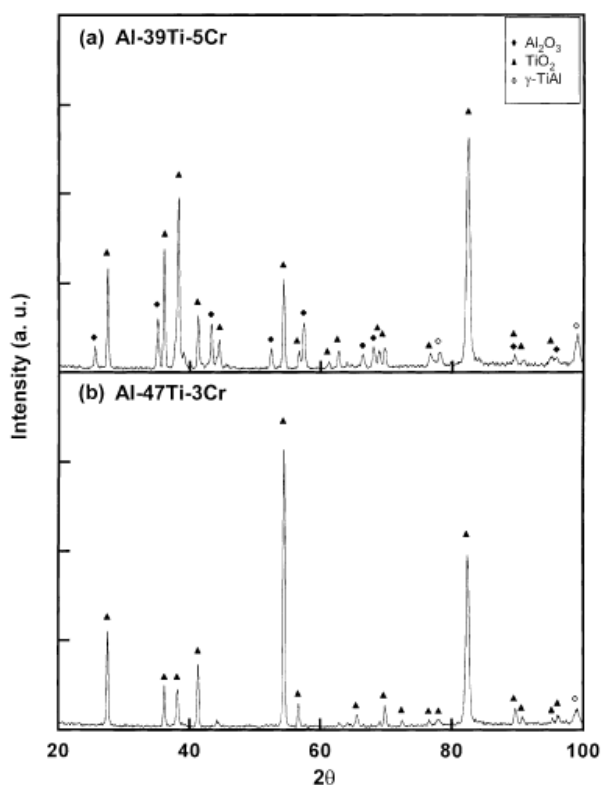


Figure 3.5.4-Diffraction pattern of Al39Ti5Cr and Al47Ti3Cr after 100h of oxidation at 1000 °C

Because it is generally accepted that $x \propto \sqrt{Dt}$ where x and t represent diffusion distance and diffusion time respectively, it is expected that the region of the diffusion layer will be expanded to about 100 μm when exposed to 10,000 h in the air.

Thus, it could be supposed that the diffusion layer might play an important role in the long-term oxidation properties if exposed to more than 10,000 h.

The study on the phase diagram in the Al–Ti–Cr ternary system [19] established that Al–39Ti–5Cr alloy and Al–47Ti–3Cr alloy were located in the γ +TiAlCr two-phase region, and the amount of Al content and volume fraction of TiAlCr phase in the Al–39Ti–5Cr alloy were larger than those in the Al–47Ti–3Cr alloy, as shown in Fig. 3.5.5 (given at 1000 °C).

Therefore, as reported by Brady et al. [19], Al–47Ti–3Cr alloy was more reactive with Al_2O_3 scale than the Al–39Ti–5Cr alloy, and this could prove that Al–39Ti–5Cr alloy is more effective in prohibiting the oxygen diffusion into the substrate.

A comparative study on oxidation properties and the reactivity with Al_2O_3 for the Al–39Ti–5Cr alloy and the Al–47Ti–3Cr alloy provides a key argument for selecting the desirable composition in the diffusion layer for improving the long-term oxidation properties.

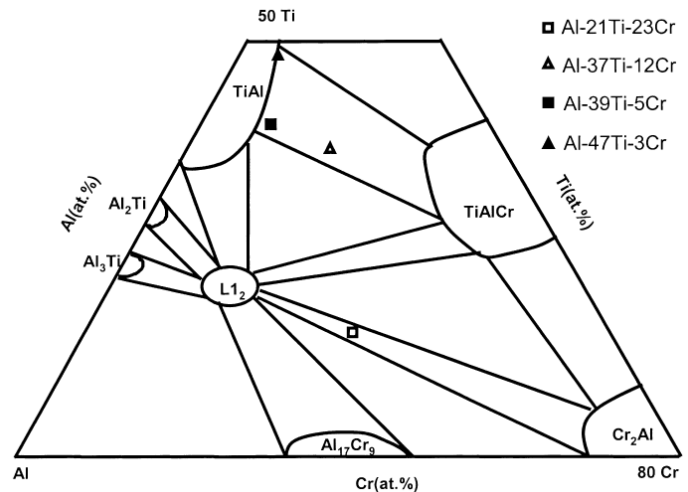


Figure 3.5.5-Partial TiAlCr ternary phase diagram [19] at 1000 °C

Consequently, it could be suggested that the composition of Al–39Ti–5Cr in the diffusion layer is more effective rather than that of Al–47Ti–3Cr for improving the oxidation resistance.

To provide more detailed information on their resistance to thermal stress, tensile and compressive tests were performed at R.T. and 1000 °C respectively, and this was compared to the thermal stress originated from the difference in the thermal expansion coefficient and the temperature change between R.T. and 1000 °C.

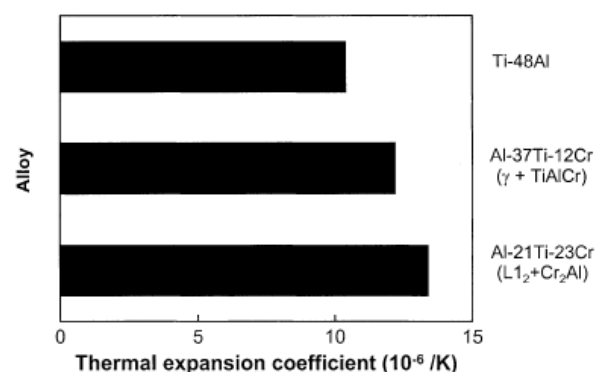


Figure 3.5.6 - Thermal expansion coefficients for various TiAl alloys

Mechanical properties in the diffusion layer were also oversimplified as compared to those in the coating layer in this study. From this result, it is considered that the γ -based two-phase alloy is a little more resistant to thermal stress than the L₁₂-based two-phase alloy because γ -based two-phase alloy has a closer thermal expansion coefficient with Ti–48Al. However, because both the L₁₂-based and γ -based alloys are very brittle under tensile stress despite good resistance to

compressive stress, tensile stress for the two alloys has more dominant effects in forming cracks, which can make it difficult to distinguish the difference in the resistance to thermal stress for the $L1_2$ -based and γ -based alloys.

On the other hand, the repeated temperature change and the increased exposure time increase the possibility of developing a crack by thermal stress, and this crack will provide the path for oxygen diffusion. Hence, oxidation properties of the diffusion layer might make more important contributions to long-term oxidation properties when oxygen invades the cracked coating layer. Although the resistance to thermal stress for the γ -based two-phase alloy is better than that for the $L1_2$ -based two-phase alloy, oxidation properties of the diffusion layer rather than the resistance to thermal stress mainly controlled the long-term oxidation properties because both alloys have very low resistance, especially under tensile stress. In this case, the $L1_2$ -based two phase alloy has better oxidation resistance than the γ -based two-phase alloy with the increased exposure time when the oxidation properties of the diffusion layer and the reactivity with Al_2O_3 scale are considered. Therefore, an inference about the long-term oxidation properties based upon the speculation mentioned above can provide the possibility for the practical application of the $L1_2$ -based two-phase alloy as a suitable coating material of the TiAl alloy.

3.6 INFLUENCE OF SILICONIZING ON THE OXIDATION BEHAVIOUR OF A γ -TiAl BASED ALLOY ^[20]

Ti-48Al-1.3Fe-1.1V-0.3B (at.%) alloy was siliconized to improve its oxidation resistance by burying it in Si powder and heating at 1073, 1123, 1173 and 1273 K for 5h in a vacuum. The isothermal oxidation behaviour of all the treated specimens was tested at 1173 K up to 97h in air using a thermobalance. To evaluate the practical performance of this measure, the cyclic oxidation behavior of the specimen, siliconized at 1273 K, was also examined at 1123 K for 350 h in a simulated exhaust gas. The element distribution, phase composition, and morphology of the Si-modified layer, and the oxide scale were characterized by AES, XRD, GAXRD and SEM. The results indicated that the TiAl alloy siliconized above 1173 K shows excellent isothermal and cyclic oxidation resistance in air or simulated exhaust gas. When siliconizing temperature is below 1123 K, however, this beneficial effect was limited to the early stage of oxidation. A Si-rich layer which was identified as Ti_5Si_3 and the following an Al-rich zone are the major constituents in the Si-modified layer on the TiAl substrate if the siliconizing temperature is above 1173 K. The thickness of the above constituent layers increases with rising siliconizing temperature. Existence of Si and Al with high concentrations is detected in the oxide scale even after long-term oxidation. It is concluded that the existing Si-rich layer, probably amorphous silica, and large amounts of Al_2O_3 in the oxide scale along with the remaining of the newly formed phase such as Ti_5Si_3 are responsible for the significant improvement in the oxidation resistance.

From the thermodynamic viewpoint of the Ti-Al-O system, it is difficult to form a dense and protective Al_2O_3 layer in the oxide scale in air for the γ -TiAl based alloy whose Al content is less than 50 at.% partly because of the almost similar equilibrium oxygen partial pressures of Ti/TiO and Al/ Al_2O_3 [21]. On the other hand, it was reported that Ti-Si based intermetallic alloys show good oxidation resistance in a temperature range 1300–1500 K which is well above the application temperature for TiAl alloys [22]. In addition, a previous investigation demonstrated that the oxidation resistance of a γ -TiAl based alloy can be improved significantly by Si implantation, which can add a small amount of Si relative to bulk alloying and thus no Ti-Si new phase layer can be formed [23]. Therefore, it is worthwhile to study the influence of Si addition to a γ -TiAl based alloy on its oxidation behavior by other measures such as siliconizing. Siliconizing readily allows massive Si diffusion to TiAl surface. Meanwhile, the new phase formation in the modified layer during the processing would be favoured, since this treatment was operated at high temperature. If the surface layer of a TiAl based alloy can be transformed to Ti-Si intermetallic-based alloy, its oxidation resistance would be much improved. Under the above consideration, the present paper deals with the influence of siliconizing on the oxidation behaviour of a TiAl-based alloy.

The chemical composition of the specimen is Ti-48Al-1.3Fe-1.1V-0.3B (at.%). The phases of the specimen detected by X-ray diffractometry (XRD) are mainly γ -TiAl and a few α_2 -Ti₃Al. The specimen surface was ground with a series of SiC paper of up to grit 1000 and then polished with alumina powders of 0.3 μ m in size.

The specimens were ultrasonically washed in acetone and ethanol bath, and dried in air before siliconizing.

The siliconizing treatment was performed at 1073, 1123, 1173 and 1273 K for 5h by burying the specimen densely in Si powder in a carbon crucible. A quartz furnace tube containing the carbon crucible was pumped to a vacuum lower than 10^{-5} Torr, and then heated to a specified temperature for a specified period and cooled. Finally, the siliconized specimen was removed from the Si powder pack, cleaned and washed again for the next-step examination.

The isothermal oxidation test was performed at 1173 K for 98 h in static laboratory air using a thermogravimetric apparatus.

The specimen was furnace cooled at the end of oxidation test. The cyclic oxidation of the alloy, siliconized at 1273 K for 5h, was conducted at 1123 K for 350 h in a simulated exhaust gas with a composition: 10%O₂ + 7%CO₂ + 6%H₂O + bal.N₂ (vol.%).

Auger electron spectroscopy (AES) was used to profile the element distribution in the siliconized layer and the scale. The phase constitution in the siliconized layer and oxidation products were identified by X-ray

The oxidation kinetic results are shown in Fig. 3.6.1(a) and Fig 3.6.1(b).

Generally, the isothermal oxidation resistance of the TiAl alloy was significantly improved for at least 98 h by the siliconizing under all the conditions.

In particular, the oxide growth rate of the alloy processed at 1173 and 1273 K is extremely low during all the exposing time (Fig. 3.6.1(a) and Fig 3.6.1(b)).

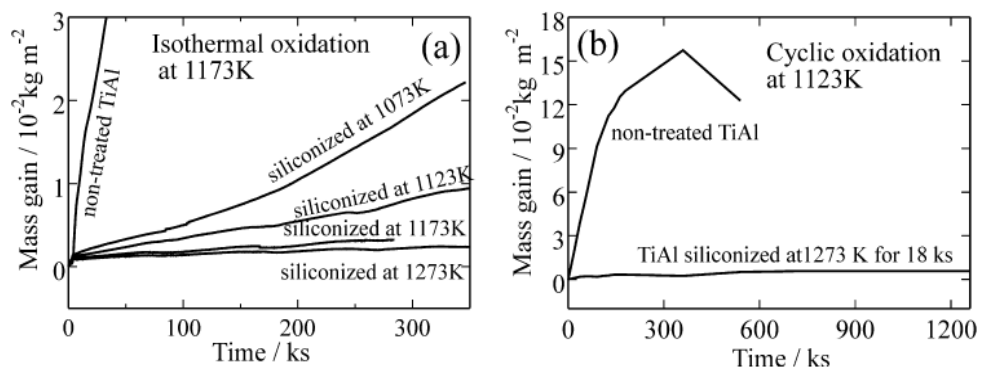


Figure 3.6.1-Oxidation behaviour for bare and siliconized TiAl with various siliconizing conditions

The near linear reaction of the alloy siliconized at 1123 K and the accelerated rate of the alloy treated at 1073 K from 33 h exposure indicate that it is effective only in the early stage of the oxidation for these two cases.

The effects of siliconizing on the oxidation resistance strongly depend on the processing temperature, as reflected by Fig. 3.6.1 (a). The oxidation rate of the siliconized TiAl alloys becomes lower as the siliconizing temperature was raised from 1073 K to 1273 K.

Fig. 3.6.1 (b) shows the cyclic oxidation behaviour of the alloy treated at 1273 K together with the non treated alloy. The non-treated alloy shows rapid mass gain until 100h followed by rapid mass loss due to the scale spallation. In contrast, the siliconizing at 1273 K gives significant resistance to the cyclic oxidation throughout 350h exposure, suggesting a high possibility of its practical application.

The element distribution in the siliconized layer is shown in Fig. 3.6.2.

Si-rich outer layers are formed with the maximum Si concentration of about 45 at.% for the four siliconizing conditions and their thickness area bout 0.5, 1.0, 1.3 and 6.0 μm , respectively, increasing with an increase in the siliconizing temperature.

Ti shows higher concentration than Al in the Si-rich layer and the suppressed Al presence in this region resulted in the following Al-rich zone on the original TiAl substrate.

Small amounts of O can be seen in the modified layer due to its diffusion from the low vacuum environment. In particular, Fig. 3.6.2 (d) suggests the formation of an oxide layer between the siliconized layer and the substrate.

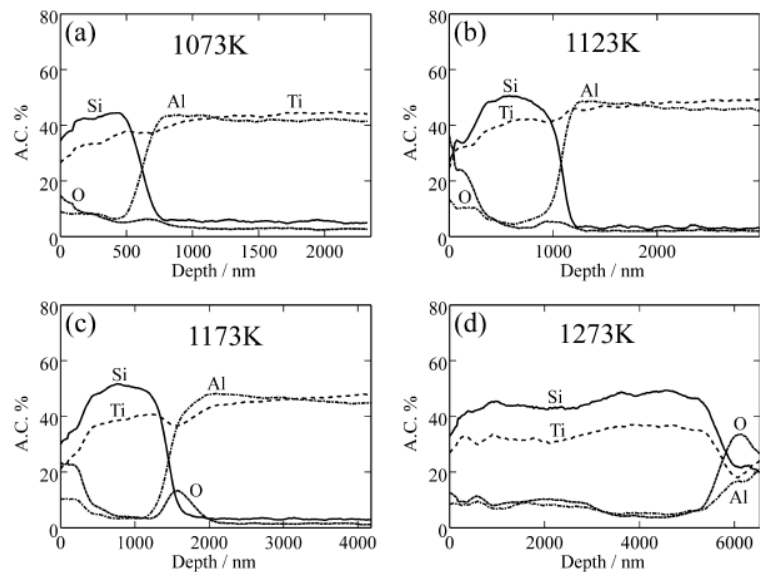


Figure 3.6.2- Superficial elements distribution versus various siliconizing temperatures

The phase constitution in the siliconized TiAl alloy was examined by XRD and GAXRD, and the results are presented in Fig. 3.6.3. Very weak Ti_5Si_3 peak along with the strongest γ -TiAl peak due to the substrate appeared in the spectrum of 1073 K siliconized alloy (Fig. 3.6.2 (d)).

It is confirmed that the formation of Ti_5Si_3 became more evident as the siliconizing temperature increased to 1173 and 1273 K whose spectrum correspond to stronger Ti_5Si_3 intensity (Fig. 3.6.3 (a)).

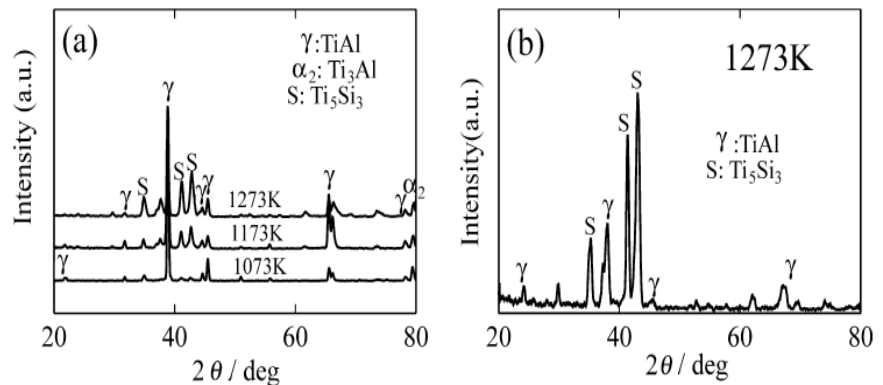


Figure 3.6.3-Diffraction pattern after siliconizing at 1173 K and 1273 K

The GAXRD pattern of the alloy siliconized at 1273 K shows the strongest peak of Ti_5Si_3 , indicating clearly a definite Ti_5Si_3 layer formed in the outer part of the modified layer (Fig. 3.6.3 (b)). By connecting this result with the element distribution profiled by AES in Fig. 3.6.3 (d), it is concluded that this Si, Ti enriched outermost layer is mainly composed of Ti_5Si_3 phase.

The surface and cross-section morphology of the siliconized layer is illustrated in Fig. 3.6.4. Very fine grain and originally polished mark can be observed in the siliconizing scale at 1073 K showing the very slow growth rate of the possible phase transformation (Fig. 3.6.4 (a)). As the processing

temperature risen to 1173 K, relatively large grain size indicates that the siliconizing proceeds rapidly and thus considerable change occurred in the substrate by this treatment. Further enlarged grains together with irregularly shaped products characterized the scale surface siliconized at 1273 K and Ti_5Si_3 is assumed as the main product (Fig. 3.6.4 (c)).

A generally smooth surface was shown without remarkable extrusion or crack. Its cross-section morphology in Fig. Fig. 3.6.4 (d) clearly revealed a newly formed modified layer composed mainly of small and compact particles with different orientations from the substrate. The area beneath this small particle layer and above the TiAl substrate is considered to be the Al- rich zone.

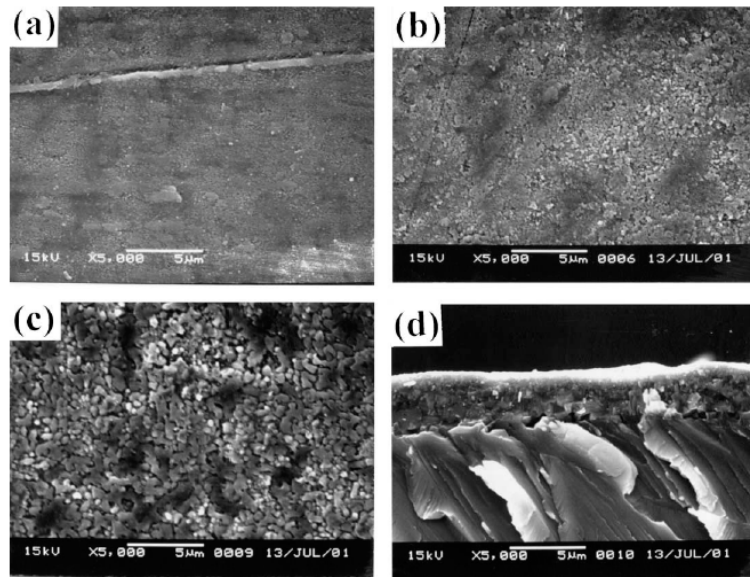


Figure 3.6.4 Surface (a,b,c) and cross-section (d) morphology of the TiAl alloy siliconized at (a) 1073 K (b) 1173 K (c) 1273 K (d) 1273 K

Fig. x shows the element profiles in the scale formed by the isothermal oxidation at 1173 K for 97 h in air for the alloy siliconized at 1273 K. The scale is about 4mm thick according to the SEM observation.

This agrees well with Fig. 3.6.5, where the scale is rich in Ti oxide and the fraction of Si-oxide increases toward the substrate. Contrarily, the amount of Al-oxide is small and almost constant in the scale, except for the very thin surface layer.

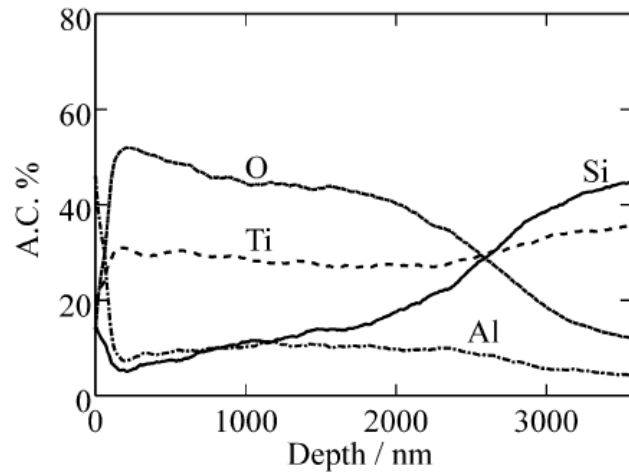


Figure 3.6.5 - AESdepth profiles for the oxide scale formed by the isothermal oxidation at 1173 K for 97h in air of the alloy siliconized at 1273 K for 5h

As revealed in Fig.3.6.6 (b) , TiO_2 (rutile) is the principal oxide phase together with substantial amounts of Al_2O_3 in the most external part of the oxide scale. However, referring to the element constitution in the scale shown in Fig. 3.6.5, Si is thought to be present as amorphous SiO_2 .

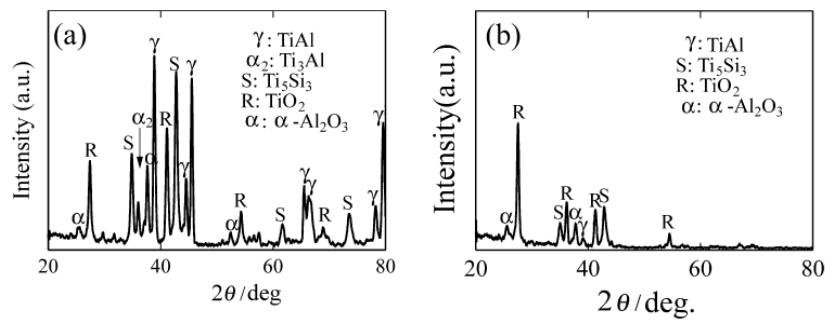


Figure 3.6.6 XRD(a) and GAXRD(b) spectra of the TiAl alloy siliconized at 1273 K for 5h and isothermally oxidized at 1173 K for 97 h in air.

Fig. 3.6.6 (a) reveals that the oxides loosely piled each other and extended out the surface. Relatively large oxide grain comprised of the rough scale surface.

For the alloy siliconized at 1273 K under same oxidation condition, the surface and cross-section morphologies of the scale are presented in Fig. 3.6.7 (b) and Fig. 3.6.8, respectively.

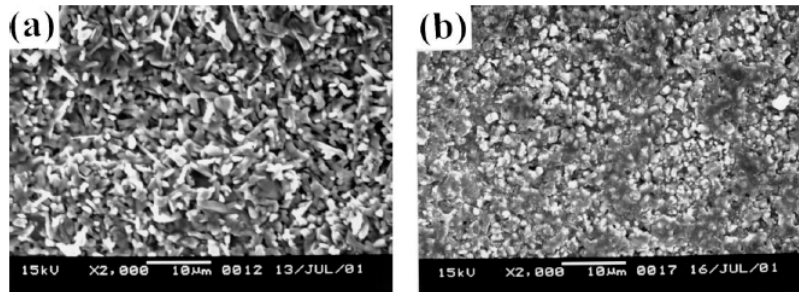


Figure 3.6.7 - (a) and (b) outer surface of the scale on the alloy siliconized at 1023 K and 1273 K for 5h after oxidation at 1173 K for 97 h in air

In Fig. 3.6.7 (b), it can be seen that the smooth scale surface consists mainly of fine grains which are thought to be TiO_2 and Al_2O_3 , and vitreous areas are thought to be amorphous SiO_2 . The cross-section shows that the scale is about $4\mu\text{m}$ thick, dense and very much adherent to the substrate. No large pores or cracks can be seen within the scale.

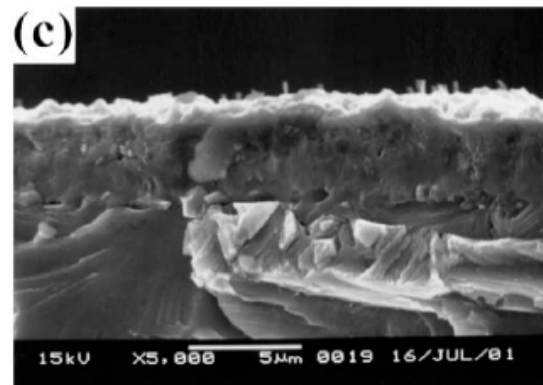


Figure 3.6.8 – cross section on the alloy surface siliconized at 1273 K for 5 h after oxidation at 1173 K for 97 h in air

It is important to remark that the modified layer formed by this measure has excellent adherence to the substrate TiAl alloy due partly to the elemental constitution continuously varying from outer surface to internal alloy (Fig. 3.6.2). As indicated in Fig. 3.6.4 (d), this newly formed Ti–Si intermetallic coating was naturally grown from the TiAl alloy through phase transformation at elevated temperature, hence this modified layer is well cooperated with the TiAl alloy. In this study, it was found that, when the siliconizing temperature is above 1173 K, along the direction from surface to the substrate, the modified layer is consisted of the following sub-layers: Ti_5Si_3 layer/Al-rich zone/TiAl substrate, cf. Fig. 3.6.2.

The thickness of the sub-layer is mainly depended on the siliconizing temperature. On the other hand, if the siliconizing temperature is too low, for example at 1073 or 1123 K, the amount of the newly formed Ti_5Si_3 or Al enriched phase would be too small to resist long-term oxidation, resulting in a limited effect as Fig. 3.6.1 (a) shows.

After long-term oxidation the remaining Si enriched layer with very high concentration could continue to resist the further oxidation as verified by the excellent isothermal and cyclic oxidation behaviour for at least 349.2 h in Fig. 3.6.1. This evidence also suggests that the following oxidation of this alloy will still maintain low rate as that of the oxidation of Ti_5Si_3 . The oxidation behaviour of Ti_5Si_3 was investigated and the detail is shown in the literature [23]. It reports that the oxidation kinetics of Ti_5Si_3 follows nearly cubic laws at 1400 and 1500 K and its oxide scale consists of another TiO_2 layer and an inner amorphous SiO_2 layer.

For the siliconized TiAl alloy, additionally, the formation of large amounts of Ti_5Si_3 would result in the internal Al-rich zone above TiAl substrate. The Al enriched layer with such thickness is also an important factor improving the oxidation resistance through favouring the formation of Al-oxide. Compared to the Ti_5Si_3 oxidation, for the siliconized TiAl alloy, the presence of Al and this Al-rich zone beneath the Ti_5Si_3 modified layer resulted in large amounts of Al_2O_3 .

In general, in the oxide scale, the amorphous SiO_2 layer together with Al_2O_3 layer would effectively protect the TiAl alloy during the high temperature oxidation and eventually have resulted in the excellent oxidation resistance.

3.7 THE IMPROVMENT OF HIGH TEMPERATURE OXIDATION OF Ti-50Al BY SPUTTERING AL FILM AND SUBSEQUENT INTERDIFFUSION TREATMENT [24]

It is well known that the TiAl₃ intermetallic shows much better oxidation resistance than γ -TiAl based alloys, because the former has greater aluminium content, resulting in a protective Al₂O₃ layer in the oxidation scale [25,26,27,28].

Therefore, a layer of TiAl₃ formed on a γ -TiAl substrate can increase the high temperature oxidation resistance of γ -TiAl. The reported methods for forming a TiAl₃ layer on γ -TiAl substrate to resist the high temperature oxidation include aluminium cladding [25], aluminium film deposition by Ion-Beam-Assisted-Deposition [26], and pack cementation aluminizing [29].

However, the improvement of the oxidation resistance is limited due to the poor adhesion of these protective coatings to the substrate, and the intrinsic brittleness of the coatings.

Here various thicknesses of pure Al films were first deposited on Ti-50Al alloy by RF magnetron sputtering.

Then a subsequent interdiffusion treatment (at 600 °C for 24–72 h in a high vacuum of about 3×10^{-7} Torr) was employed to form a TiAl₃ layer on the surface and to increase the adhesion between the thin film and Ti-50Al substrate.

Al films with different thicknesses of 0.2–5 μm were sputtered on the Ti-50Al substrate by an RF magnetron sputtering apparatus.

Fig. 3.7.1 (a) and Fig 3.7.1 (b) shows the SEM images of top-viewed and cross sectional morphologies of as-sputtered specimens with a 0.5 μm Al film thickness, respectively. From Fig. x, the Al film was found to be relatively dense, with extremely small grain size and no visible cracks. In Fig. 3.7.1 (b), the Al film and the substrate are separated by a crack that occurred when the specimen was cut for SEM cross-sectional observation.

This feature indicates that the as-sputtered Al film does not have good adhesion to the substrate.

However, stress inherent in the film increases with increasing the film thickness, resulting in the poor adhesion of coating to substrate. Once the thickness of Al film is over 5 μm , small parts of the film spall out from the Ti-50Al substrate. For this reason, in this study the thicknesses of as sputtered Al films are all less than 5 μm .

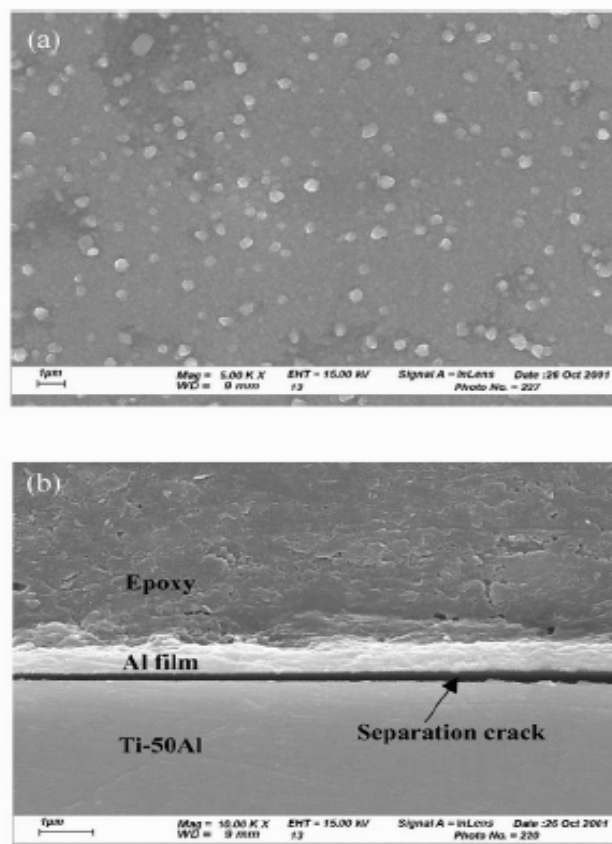


Figure 3.7.1 SEM morphologies of as-sputtered Ti-50Al specimen with 0.5 μm Al film. (a) Surface morphology and (b) cross sectional morphology

Fig. 3.7.2 shows the SEM image of the cross-sectional microstructure of Ti–50Al with a 5 μm thickness of Al film via interdiffusion treatment at 600 °C for 24 h in a vacuum :

A layer on the outer surface of the substrate can be seen to have a uniform thickness, and no cracks or voids are found at the interface. Thus, this layer exhibits good adhesion with the substrate.

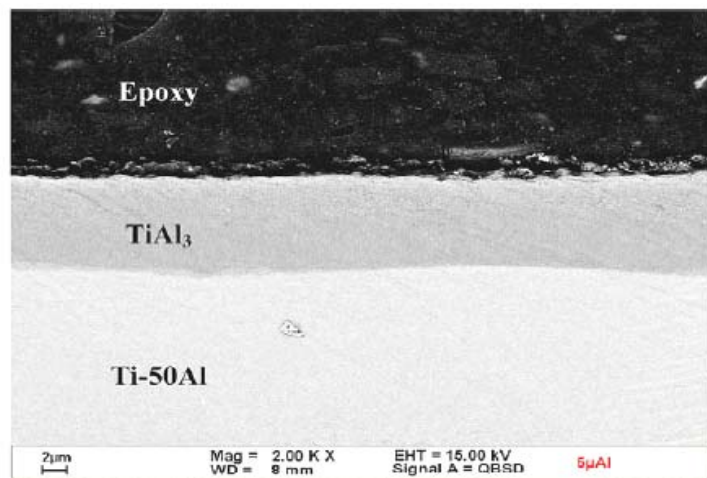


Figure 3.7.2 SEM cross-sectional morphology of Ti–50Al specimen with 5 μm Al film after interdiffusion treatment at 600 °C for 24 h in high vacuum.

The formation of this TiAl₃ layer, according to the diffusion couple test [30] and the Ti–Al phase diagram [31], are due to the following reaction



The formation of TiAl₃ ceases until all the sputtered Al film is exhausted during the interdiffusion treatment. This means that the thickness of the TiAl₃ layer formed by interdiffusion treatment is highly dependent on the thickness of sputtered Al film. It was found that, for a 5 μm thickness of Al film, the thickness of the TiAl₃ layer can be extended to about 8 μm by the reaction of Ti–50Al and Al film.

From the diffusion couple test of Ti–50Al and Al, the TiAl₃ layer can grow rapidly and obey the parabolic time dependence [30]. At the same time, only the thermodynamic stable phase(s) is presented in the end-product [32,33,34]. This feature shows why this TiAl₃ layer will further react with γ-TiAl to form TiAl₂ after 900 °C oxidation, as discussed later.

The cyclic oxidation tests were carried out at 900 °C in static air for 80 h. Each cycle consisted of heating up to 900 °C, holding at 900 °C for 5 or 10 h and then cooling to room temperature. Only the time period of the specimen exposed at 900 °C is counted in the cyclic oxidation test. The oxidation weights were measured from the weight change of the tested specimens, including the remaining and exfoliated scales.

Fig. 3.7.3 shows the (weight change per unit area)² versus the oxidation time at 900 °C air for Ti–50Al specimens with and without Al film. We can note that the thickness of Al film is a major factor in the improvement of oxidation resistance of γ -TiAl. Clearly, Ti–50Al specimens with 3 and 5 μm Al films have excellent oxidation resistance at 900 °C.

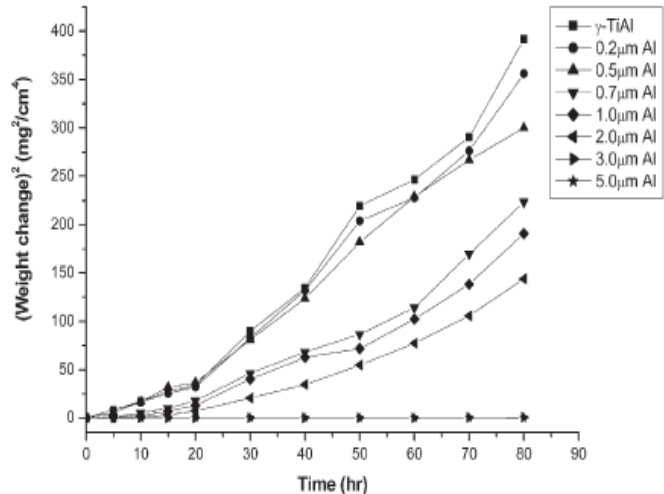


Figure 3.7.3 Cyclic oxidation tests in static air at 900 °C for Ti50Al specimens with various thicknesses of Al films which have been interdiffusion treated at 600 °C for 24 h in vacuum.

This comes from the fact that they have a sufficient thickness of TiAl_3 layer, which can form an adhesive and continuous Al_2O_3 scale on the outer surface during cyclic oxidation. At the same time, no scale spalling occurs during the cyclic oxidation for specimens with 3 and 5 μm Al films. On the other hand, the specimens with thinner Al film, especially with thickness minor than 1 μm (including the bare Ti–50Al) have the scale spalling during the oxidation.

Fig. 3.7.4 shows the calculated K_p values versus Al film thickness.

The K_p value for the cyclic oxidation of 3 μm Al film at 900 °C is $0.00709 \text{ mg}^2/(\text{cm}^4 \text{ h})$, in contrast to $4.899 \text{ mg}^2/(\text{cm}^4 \text{ h})$ for the bare Ti–50Al. The K_p value for the former one is about 1/700 of the latter one. K_p value for the cyclic oxidation of 5 μm Al film at 900 °C can be further reduced to $3.2 \times 10^{-4} \text{ mg}^2/(\text{cm}^4 \text{ h})$, which is about 1/15,000 of K_p value for the bare Ti–50Al.

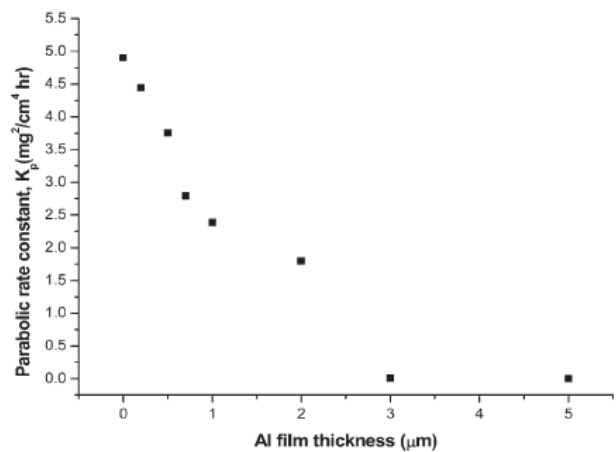


Figure 3.7.4 Effect of the thickness of Al film on the cyclic oxidation resistance (parabolic rate constant K_p) of Ti–50Al specimens oxidized in 900 °C air. The K_p values are calculated from Fig. 3.7.3

However, the improvement of oxidation resistance is limited when the Al film thickness is less than 2 μm . This may be because the thickness of TiAl_3 layer is not thick enough to protect against the diffusion of oxygen into the substrate.

Isothermal oxidation tests were performed by TGA at 900 °C for 70 h to compare oxidation properties of Ti-50Al with and without Al film, as shown in Fig. 3.7.5. With XRD investigations for specimens with a 1 μm Al film, the peaks for Al₂O₃, TiO₂ and TiAl₂ phases are identified. This indicates that the formed oxides consist of a mixture of Al₂O₃ and TiO₂. Moreover, the appearance of TiAl₂ peaks indicates that TiAl₃ has reacted with γ-TiAl to form TiAl₂ at 900 °C oxidation.

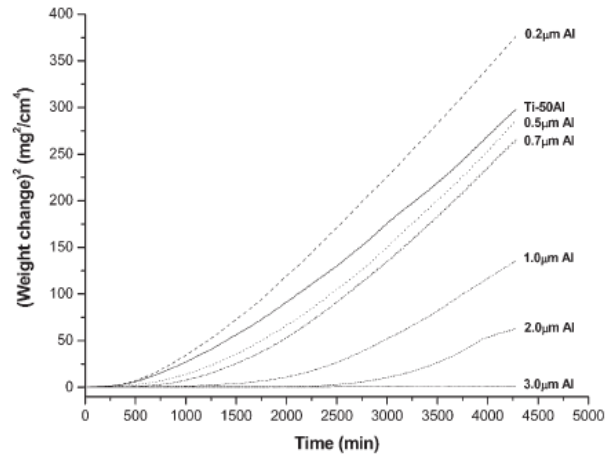


Figure 3.7.5 TGA isothermal oxidation tests in static 900 °C air for Ti-50Al specimens with various thicknesses of Al films.

When the thickness of Al film increases, i.e. the TiAl₃ layer becomes thick, the peak intensities for Al₂O₃ and TiAl₂ become strong, whereas those for TiO₂ become weak. For the Ti-50Al specimen with 5 μm Al film, the XRD spectrum shows only Al₂O₃ and TiAl₂ peaks, implying that a protective alumina scale, instead of a fragile TiO₂.

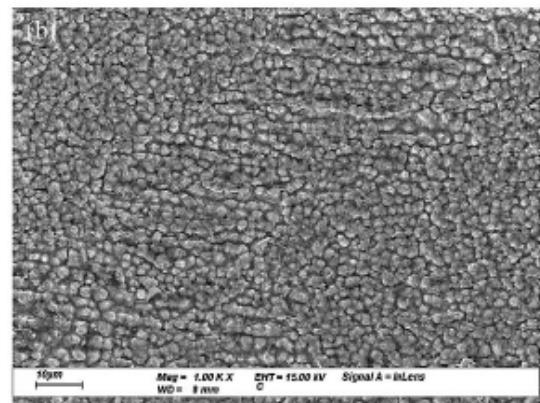
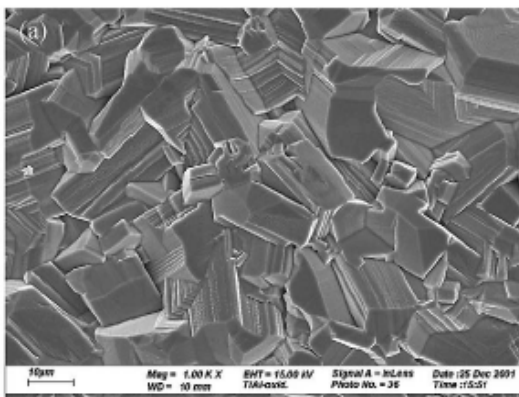


Fig. 3.7.6. SEM surface morphologies of the oxidation scale after 900 °C × 80 h oxidation for (a) 0.5 μm Al film and (b) 3 μm Al film. The specimens were interdiffusion treated in high vacuum before the oxidation.

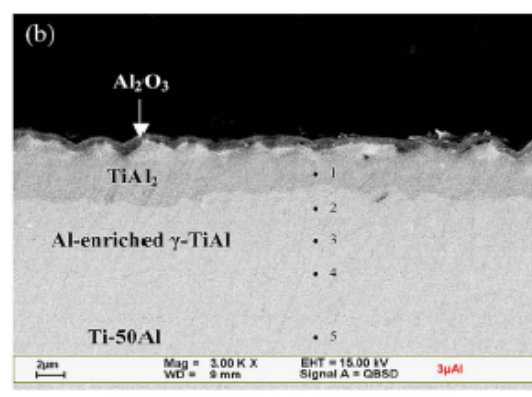
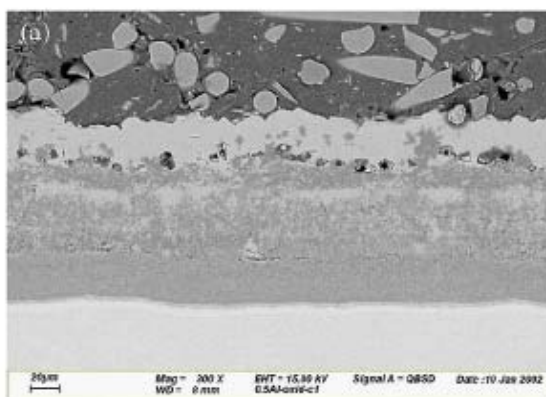


Fig 3.7.7- SEM cross-sectional images of the specimens of Fig. 3.7.6 for (a) 0.5 and (b) 3 μm Al film.

TiAl₃ can totally react with γ -TiAl to form TiAl₂ phase after oxidation at 900 °C for 80 h in air, however, with increasing oxidation time, the thickness of the TiAl₂ layer decreases due to the solid-state diffusion with Ti–50Al at high temperature.

In order to realize the stability of the TiAl₂ phase, Ti–50Al specimens with 5 μ m Al film via interdiffusion treatment and then oxidation at 900 °C for various times were investigated and their cross-sectional SEM images are shown in Fig. 3.7.8.

From Fig. 3.7.8(a), it can be seen that in the initial period of oxidation time (1h at 900 °C), a mixture of TiAl₃ outer layer and TiAl₂ inner layer coexists. This indicates that TiAl₂ is reacted from TiAl₃ and γ -TiAl.

Comparing the thickness of the TiAl₂ layer to that of TiAl₃ layer, as shown in Fig.3.7.8(a), one can find that the reaction rate between TiAl₃ and γ -TiAl is rapid and it is completed within 5 h.

This result is similar to the case of the diffusion couple [30] in which the TiAl₂ formation requires about 4 h at 750 °C.

After 300 h oxidation, as shown in Fig. 3.7.8 (f), the thickness of the TiAl₂ layer is reduced to only about 5.5 μ m in thickness.

Because the TiAl₂ can be exhausted eventually, and from the thickness measurement of the TiAl₂ layer of Fig. 3.7.8 (b)–(f), one can estimate that the exhaustion time of the TiAl₂ layer at 900 °C for a specimen with a 5 μ m Al film is about 700 h.

The EDXS results of points 1 and 2 (Fig 3.7.8 (f)) indicate that this layer is a Ti–Al–O compound with its composition approximating Ti₃₇Al₅₃O₁₀. Since this compound has not been reported yet, further study is needed to identify its exact composition and structure

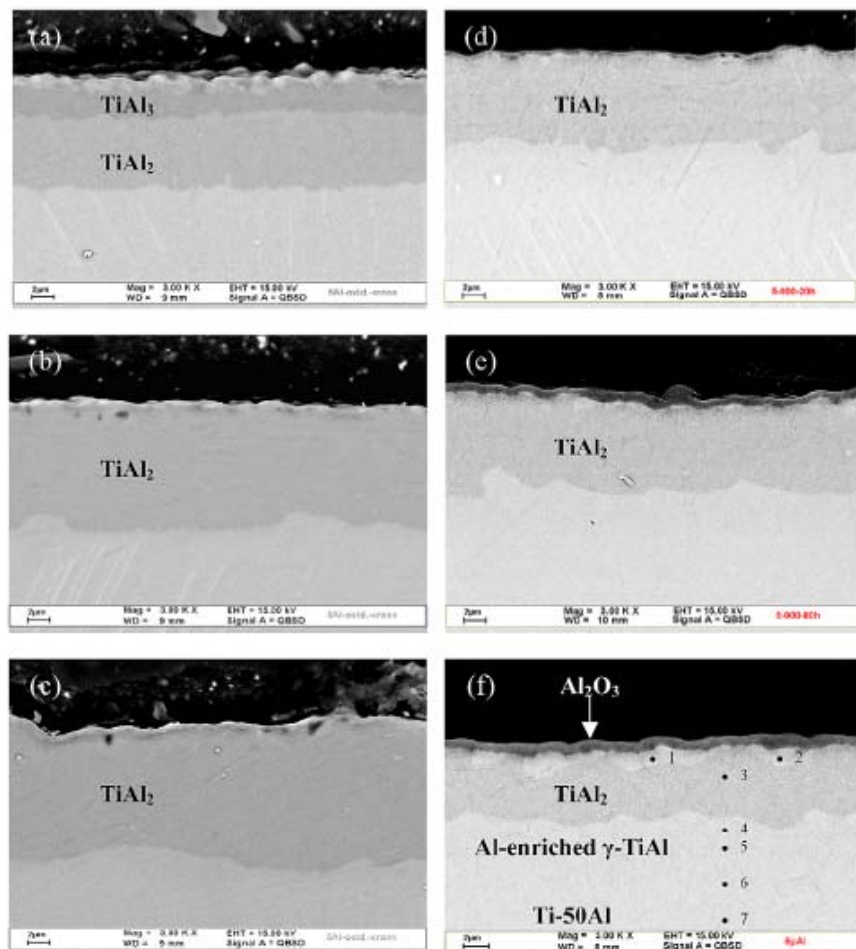


Figure 3.7.8 SEM cross-sectional images of Ti–50Al specimens with 5 μ m Al films which have been interdiffusion treated, and then oxidized at 900 °C in air for (a) 1 h (b) 5 h (c) 10 h (d) 20 h (e) 80 h and (f) 300 h. The EDS analysis for the composition of points 1–7 shown in (f) is listed in Table 3.7.1.

Location	Composition			
	Ti (at. %)	Al (at. %)	O (at. %)	Phase
Point 1	36.03	52.85	11.11	Ti–Al–O compound
Point 2	36.46	53.51	10.03	Ti–Al–O compound
Point 3	33.66	66.34	–	TiAl ₂
Point 4	41.14	58.86	–	Al-enriched γ -TiAl
Point 5	43.55	56.45	–	Al-enriched γ -TiAl
Point 6	45.56	54.44	–	Al-enriched γ -TiAl
Point 7	49.75	50.25	–	Ti–50Al

Figure 3.7.9 - Atomic compositions (from EDXS analysis) referred to the positions of Fig 3.7.8

As conclusion we can say that cyclic and isothermal oxidation tests show that the Ti–50Al with 3–5 μm Al film can dramatically reduce the oxidation at 900 °C in air, at which the parabolic oxidation rate constant K_p of specimen with 5 μm Al film is only about 1/15000 of that of bare Ti–50Al. XRD and SEM results indicate that the TiAl₃ layer can promote the formation of a protective Al₂O₃ scale on the surface as well as react with γ -TiAl to form TiAl₂ during the oxidation.

4 OXIDATION RESISTANCE IMPROVEMENT VIA LASER ABLATION

As seen in Chapter 1 is evident that the stability of Al_2O_3 is only slightly higher than that of TiO (which becomes oxidized to TiO_2 as found in actual scales), i.e. , only slight differences in the Ti and Al activities may turn the stabilities of the oxides formed on the respective substrate.

This fact leads to the primary oxidation of Ti in our alloy (Ti 30.5Al 9W 0.4Si).

The oxidation , such as other chemical reactions , is driven by two factors : thermodynamic and kinetic.

We can change the thermodynamic by changing the composition (adding Al) but this method can have detrimental effects on mechanical properties.

We can improve the oxidation resistance by increasing the diffusivity of aluminium.

As reported in the Wagner's scaling model [36] the suppression of internal oxidation of Al to form discrete Al_2O_3 platelets in the substrate is also effective to make a continuous Al_2O_3 layer on the specimen surface : the criterion for the transition from internal to external scaling is given by Eq 4.1

$$N_{Al} > \left(\frac{\pi g}{3} * N_o * \frac{D_o V_M}{D_{Al} V_{OX}} \right)^{0.5} \quad \text{Eq 4.1}$$

Where N_{Al} is the Al content , N_o is oxygen solubility in the alloy substrate ; D_{Al} and D_o are diffusivities of Al and oxygen , respectively. V_M and V_{OX} are volumes of TiAl and Al_2O_3 per mole of Al , respectively, "g" is a conversion factor from internal to external oxidation [36].

If aluminium diffusivity becomes higher then N_{Al} decreases , leading to a alumina richer scale.

If the diffusivity of the mainly oxidized element is sufficiently high then a appropriate concentration at the oxidation interface can be maintained : in other words the atom flux from the bulk material must support the oxidation of this element.

If this condition is not satisfied the multi element oxidation will appear.

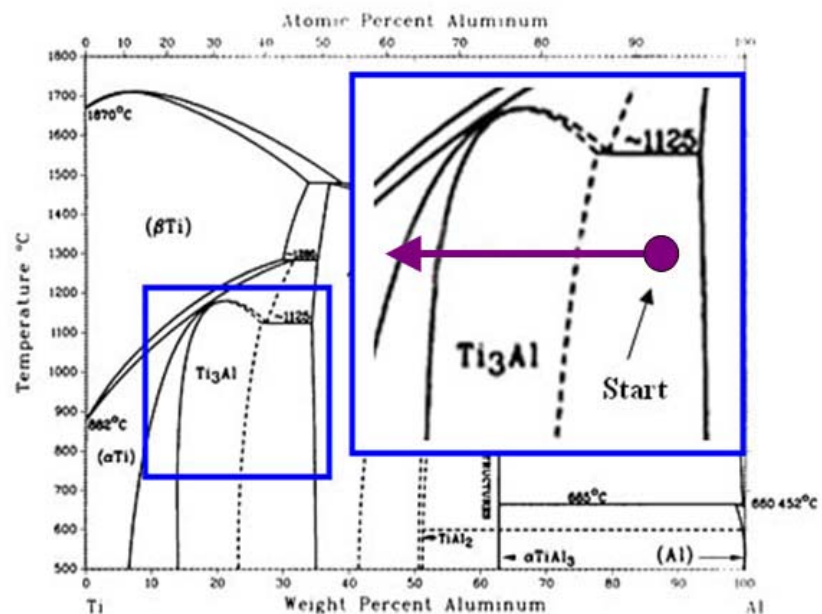


Figure 4.1- Binary TiAl phase stability diagram

If the aluminium diffusivity is enough then the oxidation interface composition point don't move from the starting point , as shown in Fig 4.1.

On the other hand if the diffusivity is low then the aluminium depletion behind the oxidation front will lead to $\alpha_2\text{Ti}_3\text{Al}$ and $\beta\text{-Ti}$ formation , with detrimental effects on the resulting oxidation resistance.

We can increase the aluminium diffusivity with surface nanocrystallization.

A previous work [44] demonstrates the possibility to improve the oxidation resistance of an $\gamma\text{-TiAl}$ alloy through nanocrystallization via Vacuum Plasma Spray (VPS) ablation : a VPS torch can produce temperatures up to 15000 °C and the successive surface cooling can produce a ultra-fine grained structure , activating a lot of new “ diffusion paths “ at the grain boundaries. The nanocrystallization is a “ general “ methodology to improve oxidation resistance and its applicability is confirmed on Ni-base superalloys [45] and on MCrAlY [46] coatings.

In a multi-grain bulk material the atoms diffuse through the grain and at the grain boundaries; We can at this point define two diffusivities :

“ through the grain $\rightarrow D_G$ “ and “ at the grain boundary $\rightarrow D_{BG}$ “

As seen in fig x we will represent our material with hexagonal grains.

We will also assume a thickness of 0.5 nm for the grain boundary [47]

At this point the “ global diffusivity “ can be written [47] as the area-weighted average diffusivity between grain and grain boundary , as seen in Equation 4.2

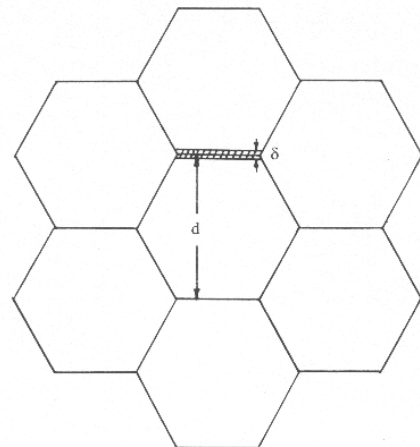


Figure 4.2- Schematization of the alloy with an hexagonal grain structure

$$D_{eq} = \frac{D_{gb} * A_{gb} + D_g * A_g}{A_{gb} + A_g} = \frac{\sqrt{3}\delta d D_{gb} + \frac{\sqrt{3}}{2} (d - \delta) d D_g}{\sqrt{3}\delta d + \frac{\sqrt{3}}{2} (d - \delta) d} \quad \text{Eq 4.2}$$

Because usually $D_{BG} > D_G$ the global diffusivity will be increased.

Aluminium diffuses easily at the grain boundary that titanium and for this reason the nanocrystallization “helps” the aluminium oxidation because the aluminium global diffusivity was more increased than the titanium global diffusivity

The nanocrystallization was obtained with laser ablation. The laser was a Kr-F device. The experimental geometry is represented in Fig 4.3. The process was conducted in air. The laser beam “scans” the sample

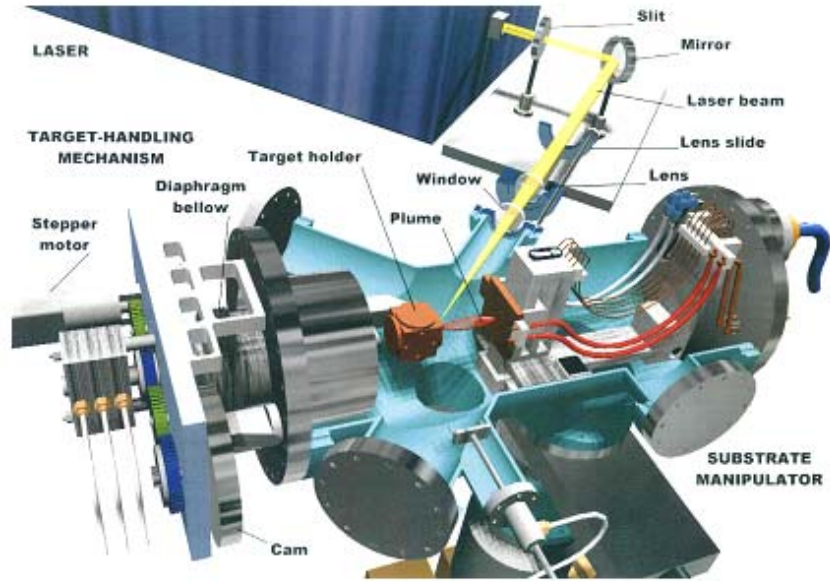


Figure 4.3 -Schematization of the laser apparatus

4.1 THE NANOCRYSTALLIZATION VIA LASER ABLATION

Considering a little solid element in a molten bed [40], if some atoms are getting together to form a little solid sphere then the free energy becomes equal to

$$G'' = V_S G_{VS} + V_L G_{VL} + A_{SL} \gamma_{SL} \quad \text{Eq 4.3}$$

Where V_S is the volume of the solid cell, V_L the volume of the liquid phase, A_{SL} the area of the solid/liquid interface, G_{VS} and G_{VL} the free energy densities (for a specified volume unit) for the solid and the liquid phase, respectively.

“ γ_{SL} ” is the free energy associated to the physical discontinuity between the solid and the liquid interface.

If no any solid cell is present then the free energy becomes equal to

$$G' = (V_S + V_L) G_V^L \quad \text{Eq 4.4}$$

After the formation of a solid sphere in the molten bed the free energy variation is :

$$\Delta G = -V_S \Delta G_V + A_{SL} \gamma_{SL} \quad \text{Eq 4.5}$$

For an assigned ΔT the free energy variation becomes equal to :

$$\Delta G_V = \frac{L_V \Delta T}{T_m} \quad \text{Eq 4.6}$$

Where L_v is the free energy variation associated to the solidification process and T_m the melting temperature. If γ_{SL} can be assumed as isotropic then the cluster form during solidification is a sphere with radius equal to "r" and Eq 4.5 becomes :

$$\Delta G_r = -\frac{4}{3}\pi r^3 \Delta G_v + 4\pi r^2 \gamma_{SL} \quad \text{Eq 4.7}$$

The free energy of a solidification cluster with radius equal to "r" is represented in Fig 4.4 : it's evident that there a critical dimension should be reached .

The critical radius value is

$$r^* = \frac{2\gamma_{SL}}{\Delta G_v}$$

The corresponding free energy value is

$$\Delta G^* = \frac{16\pi\gamma_{SL}^3}{3(\Delta G_v)^2}$$

The cluster that don't reach this value is destined to be re-melted in the liquid phase.

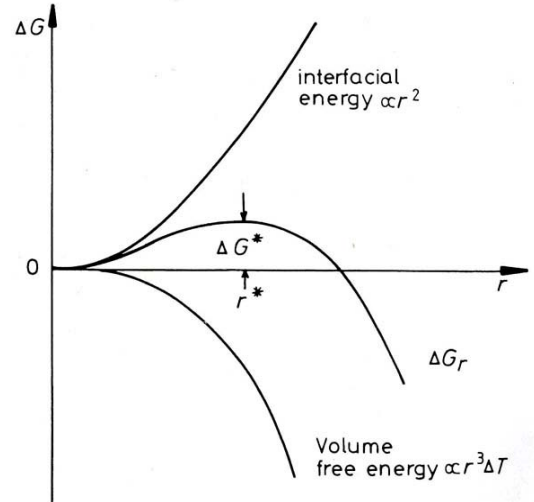


Figure 4.4 - Total free energy variation versus solid cluster radius in a molten bed

The critical value for the radius can be written in this manner:

$$r^* = \left(\frac{2\gamma_{SL}T_m}{L_v} \right) \frac{1}{\Delta T} \quad \text{Eq 4.8}$$

This means that with an high value of ΔT (undercooling) a very fine solidification structure can be obtained. The number of spherical clusters with radius equal to "r" is given by:

$$n_r = n_0 \exp\left(-\frac{\Delta G_r}{kT}\right) \quad \text{Eq 4.9}$$

Where n_0 is the total number of the atoms in our system and K the Boltzmann constant. At the same manner the cluster number with critical radius "r*" is given by

$$C^* = n_0 \exp\left(-\frac{\Delta G^*}{kT}\right) \quad \text{Eq 4.10}$$

All these cluster can reach the stability (for further growth) with one single-atom addition:

If the atom addition has frequency equal to “ f_0 ” then the nucleation speed will be equal to :

$$N_{hom.} = f_0 n_0 \exp\left(-\frac{\Delta G^*}{kT}\right) \left[\frac{cluster}{m^3 s}\right] \quad \text{Eq 4.11}$$

We can now rewrite Eq 4.11 as function of ΔT (undercooling) having :

$$N_{hom.} = f_0 C_0 \exp\left[-\frac{A}{(\Delta T)^2}\right] \quad A = \frac{16\pi\gamma_{SL}^3 T_m^2}{3L_v^2 kT} \quad \text{Eq 4.12}$$

As reported in Fig 4.5 the nucleation speed is more than exponential due to the term ΔT^2 in Eq 4.12.

After ΔT_N we have an “ explosion “ in the nucleation speed. There is a very large variation in the nucleation speed in a relatively small ΔT scatter band.

Turnbull [41] suits for ΔT_N 1/5 of T_m

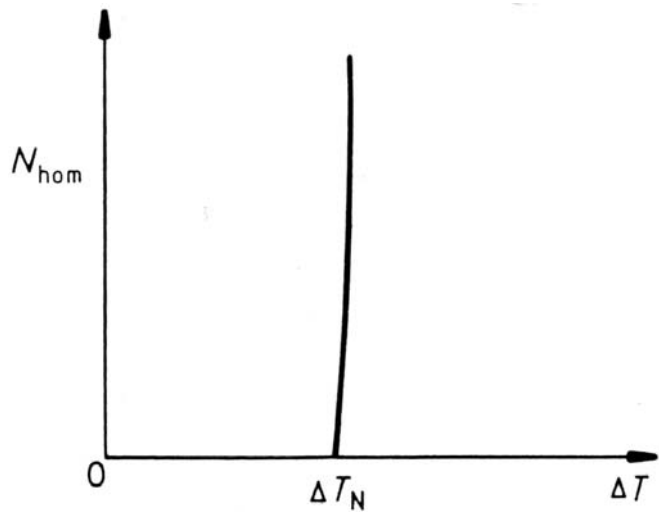


Figure 4.5 - Nucleation speed versus undercooling

The temperature variation during the cooling time is shown in Fig 4.6.

With a special model for this phenomenon a 10^{10} Ks^{-1} cooling rate can be estimated [42]: the result is an extremely fine solidification structure, on the nano-scale.

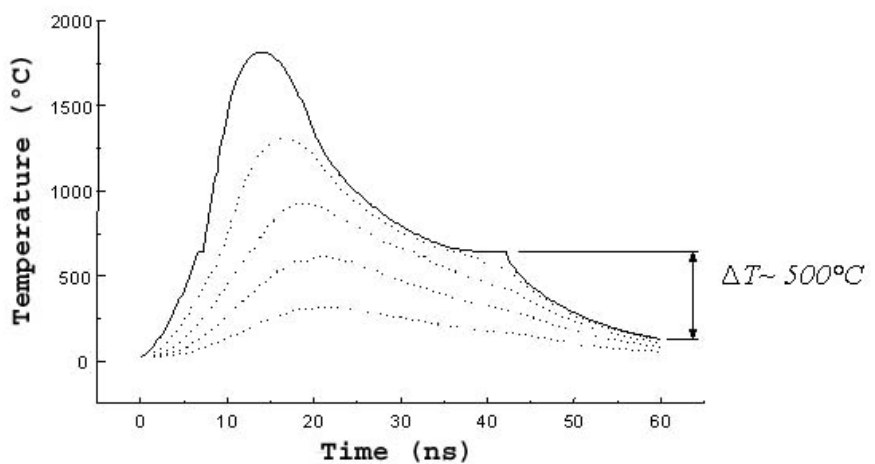


Figure 4.6 - Temperature variation during cooling time

4.2 EXPERIMENTAL

Alloy samples were obtained by cutting a TiAl cylindrical barrel into a 3mm thick discs. The original bar was obtained via plasma melting and successive hot hydrostatic pressing (HIP) for 4 h at 1260 °C and 172 MPa.

A thermal treatment was conducted as follows in order to obtain a lamellar structure: 1h at 1350 °C → 6 h at 1000 °C

The composition of our alloy is given in Table 4.1

Element	Ti	Al	W	Y	Si
Wt %	bal	30.5	9	traces	0.4

Table 4.1- Alloy composition

As shown in Fig 4.1 the composition point is in the γ - α_2 zone . The alloy is optimized for the oxidation resistance due the high W content which reduces the diffusivity of oxygen and its solubility [48,49]

This alloy is better than an Ti50Al alloy even if it in the γ -TiAl₂ field is and the brittleness is relatively low.

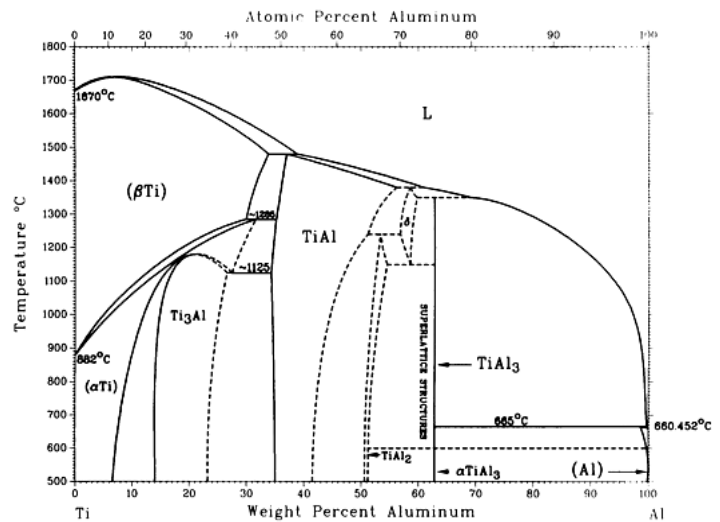


Figure 4.1- Binary Ti-Al phase equilibrium diagram

As shown if Fig 4.2 the structure is near to fully lamellar.

The grain size is ranging between about 1 mm at the center of the barrel and 50 micron neat to the external surface

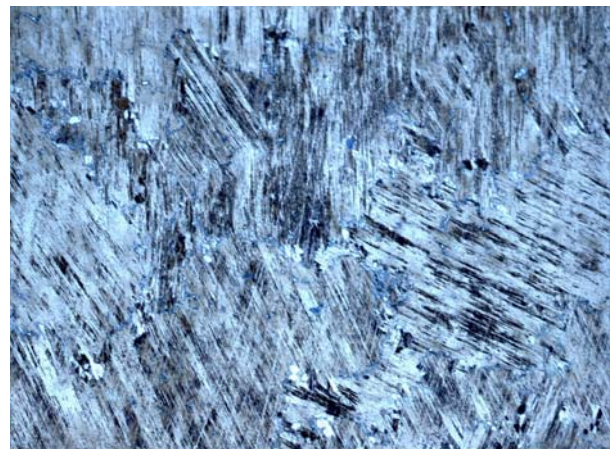


Figure 4.2 - Optical microscope image of the Ti 30.5Al 9W 0.4Si alloy (untreated)

The ablation conditions are given in Table 4.2

Parameter	High energy	Low energy
Energy [mJ]	300	150
Irradiated Surface [mm ²]	13.57	13.57
Energy density [mJ / mm ²]	22.11	11.05
Frequency [Hz]	20	20
Scanning speed [mm/s]	1.5	1.5
Focal length [mm]	600	600

Table 4.2 Conditions of the laser ablation process

The effect of the laser ablation is visible in Fig 4.3. The scanning lines are generated due the local heating process , conducted in air. Their thickness is low in order to observe a cross section. Both “high energy” and “low energy “ samples displayed this effect.

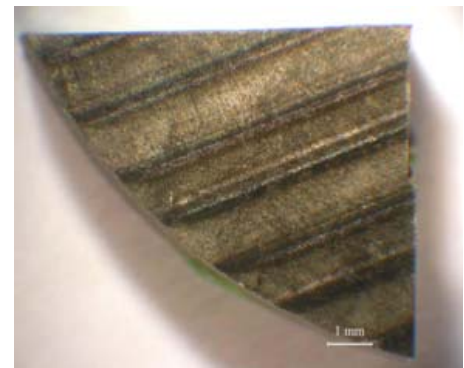


Figure 4.3 - Optical image of an high energy ablated sample

The laser ablation generates during sample scanning an oxidative process (in both cases of high and low energy treatment) on the surface : the oxide thickness is too low and cannot to be measured . The most dark lines on the sample surface are locations with higher oxidation grade : this is well visible in Fig 4.4.

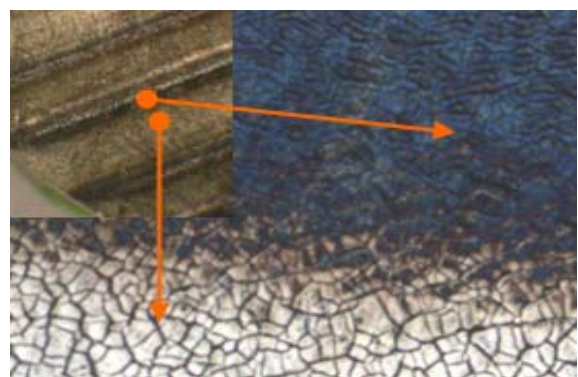


Figure 4.4 - Optical image of an high energy ablated surface; the orange dot at arrow's starting point indicates the "macroscopic" position on the sample

4.3 RESULTS AND DISCUSSION

The effect of the laser ablation is visible in Fig 4.5

The “transformed zone” of the high energy sample is about 3 micron thick but the “transformed zone” of the low energy sample is not very well visible : this is probably due to the very low physical-chemical changes generated by the laser treatment.

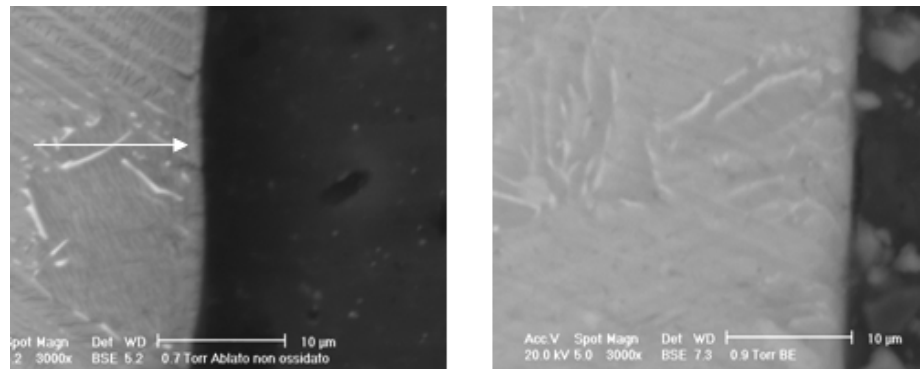


Figure 4.5 – SEM surface cross-section image of an high energy (left) and of an low energy (right) ablated sample

On the high energy treated surface some micro-cracks were found as shown in Fig 4.6. The length microcrack’s was about twice greater than the modified thickness. The micro-cracks are probably originated during the cooling time due the high stress gradient. The micro-crack can securely act as diffusion path for oxygen , reducing the oxidation resistance.

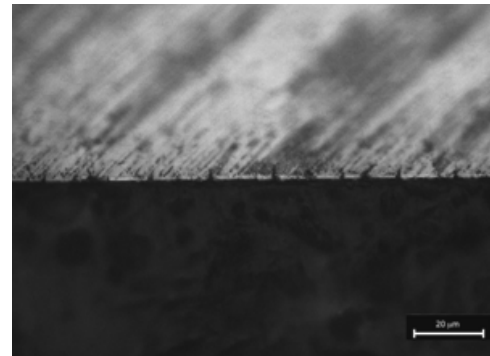


Figure 4.6 - SEM image of the microcracks originated after the ablation process

The laser ablation has still an effect on the chemical composition : a relatively high Al atoms number evaporates from the surface leading to a superficial Al depletion zone; this is more evident for the high energy (AE) samples.

The aluminium evaporation can be viewed with EDXS microprobe , as shown in Fig 4.7

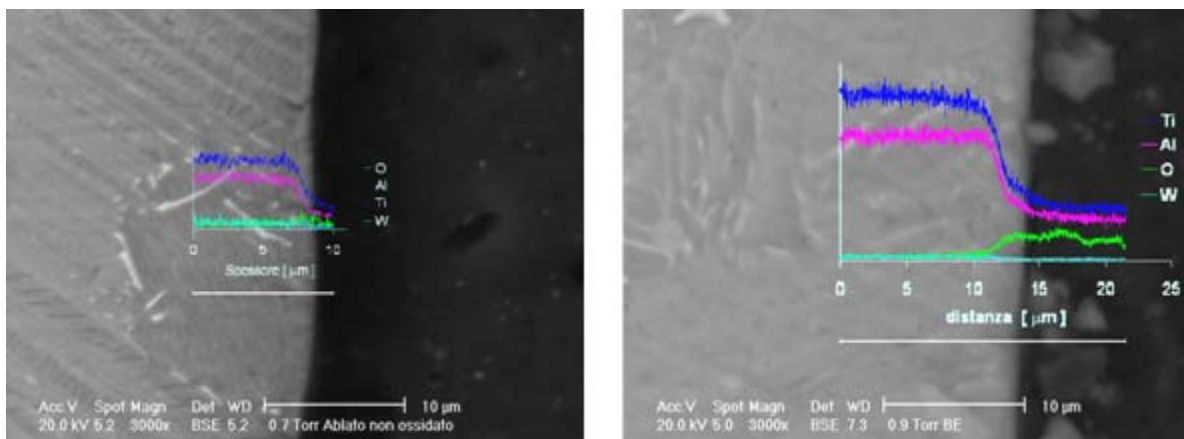


Figure 4.7 - Concentration profiles near surface (from EDXS linescan) in the as-treated condition : high (left) and low (right) laser ablation generates an aluminium loss via evaporation

The white line in Fig 4.7 under the concentration graph indicates the measuring line for the EDXS microprobe.

In the “as-treated” samples α_2 -Ti₃Al and γ -TiAl were found : an ulterior volume percentage of α_2 -Ti₃Al is probably generated by the aluminium loss due the heat- induced evaporation.

On an high energy ablated sample the aluminium concentration at the surface drops to 28.2 [at%] : in the untreated condition the aluminium concentration is equal to the nominal value (46 [%at]). The laser ablated layer is in the α_2 -Ti₃Al field (Fig 4.1)

In the high energy samples still β -Ti was found (with TEM – SAED analysis). In both of the high energy and low energy cases the resulting solidification microstructure was on the nano-scale : the grains were averagely 15 nm large , as shown in Fig 4.8.

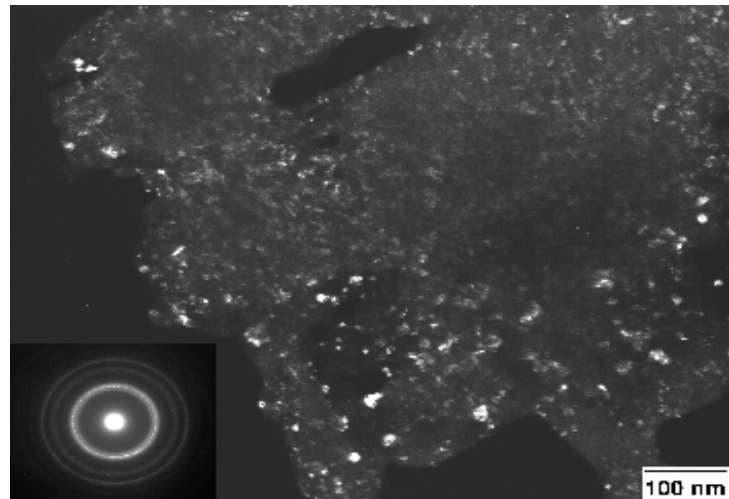


Figure 4.8- TEM image of an high energy ablated sample

As displayed in Fig 4.9 the main phases in the alloy after the laser ablation are : β -Ti , γ – TiAl , α_2 -Ti₃Al. The high energy laser treatment seems leading to an higher α_2 -Ti₃Al fraction as the low energy treatment. β -Ti was found only in the high energy ablated samples in TEM analysis.

In case of laser ablation (and subsequent oxidation) XRD spectra are not useful for quantitative analysis due the layered structure near to the surface.

In this situation a better examination can be performed with EDXS

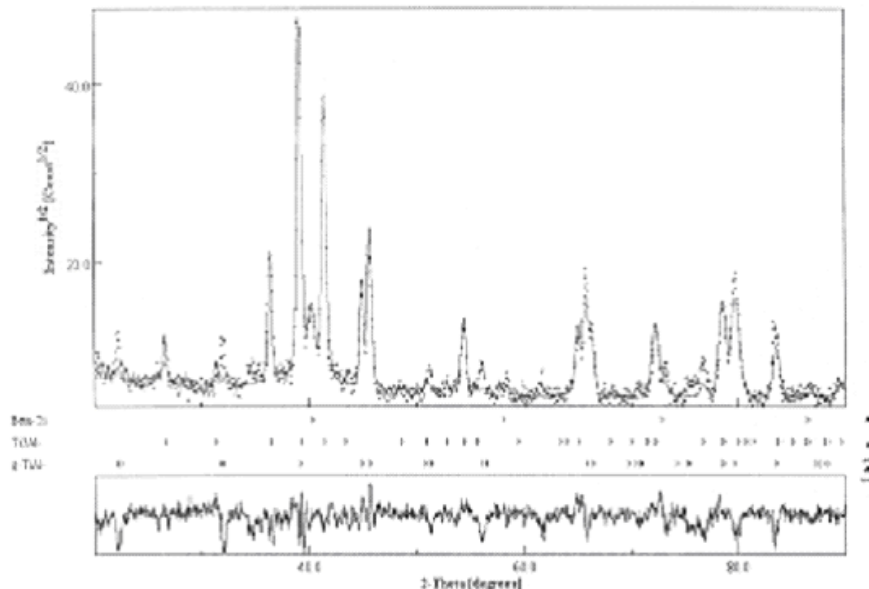


Figure 4.9- XRD diffraction pattern of an laser ablated sample

linescans after the phases identification through XRD analysis. In all the cases the α_2 -Ti₃Al seems to be progressively the main phase beneath the oxide scale : this is due to the formation of an aluminium depletion zone during oxidation.

The oxidation tests were conducted at 750 °C and 900 °C in air in a tubular furnace.

Low energy treated samples showed better oxidation resistance than high energy treated samples at both testing temperatures.

This is probably due to the higher aluminium loss during laser ablation.

The low energy ablation gave better oxidation resistance than the bare alloy: the corresponding oxidation kinetic was reduced to about 50-60 percent of the original value.

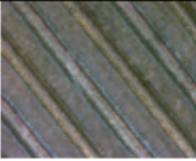
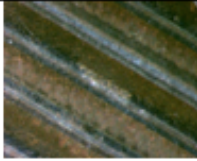

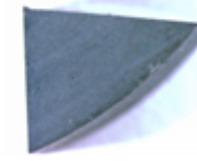



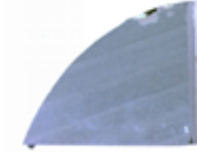
Oxidation test at 750°C		
Time	AE Surface	BE Surface
24 h		
94 h		
240 h		
430 h		

Figure 4.9 - Optical images collection of the 750 °C oxidation test

In the oxidation test at 900 °C good oxidation resistance was observed until 100 h for high energy treated samples and until 250 h for low energy treated samples (Fig 4.10)

An appreciable oxidation resistance improvement was obtained only on low energy treated samples , on the other hand high energy ablation produced detrimental effects.



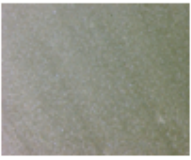


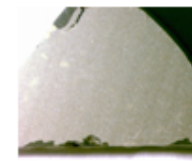
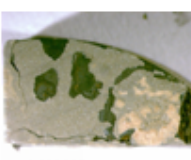
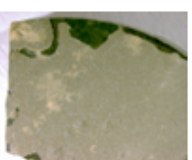
Oxidation test at 900°C		
Time	AE Surface	BE Surface
24 h		
96 h		
257 h		
497 h		

Figure 4.10 - Optical images collection of the 900 °C oxidation test

As shown in Fig 4.11 the crack pattern in the high energy ablated samples act as preferential site for oxide growth , favouring the oxygen diffusion trough the modified layer.

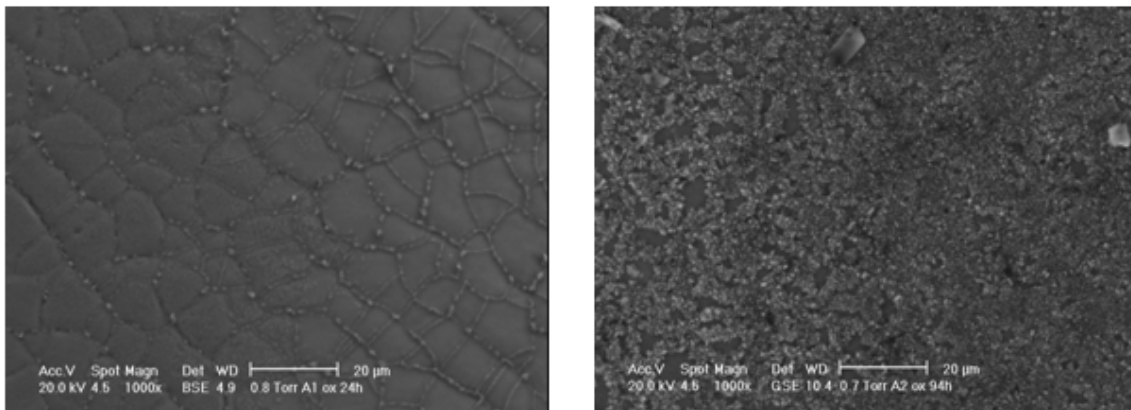


Figure 4.11- SEM surface of an high energy treated sample exposed to oxidation for 24h at 750 °C (left) and 94h at 750 °C (right)

The next image (Fig 4.12) shows the surface of an low energy treated sample exposed to oxidation for 24h at 750 °C (left) and 94h at 750 °C (right) : here no preferential oxidation at the crack line is observed ; the oxidation seems to be uniform on the external surface.

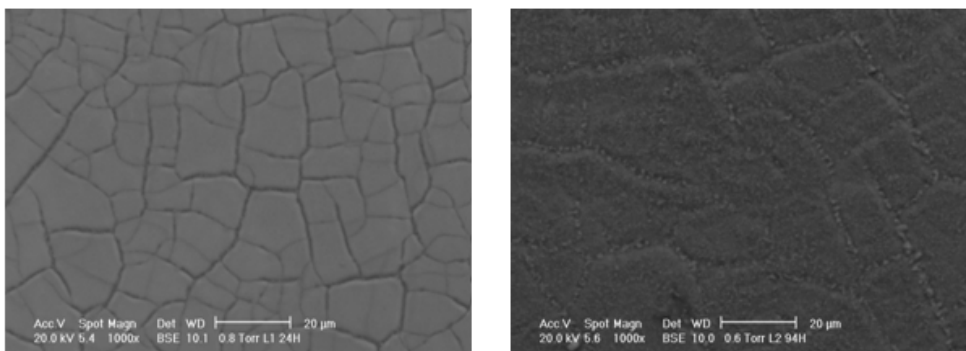


Figure 4.12- SEM surface of an low energy treated sample exposed to oxidation for 24h at 750 °C (left) and 94h at 750 °C (right)

The external scale appearance was approximately the same for both high energy and low energy treated samples , as shown in Fig 4.13 .

In all the cases the scale seems to be made of relatively large platelets and prismatic TiO_2 crystals . Fig 4.13 shows the surface of an high energy treated sample exposed to oxidation for 497h at 900 °C (left) and of an low energy treated sample exposed to oxidation for 497h at 900 °C (right) .

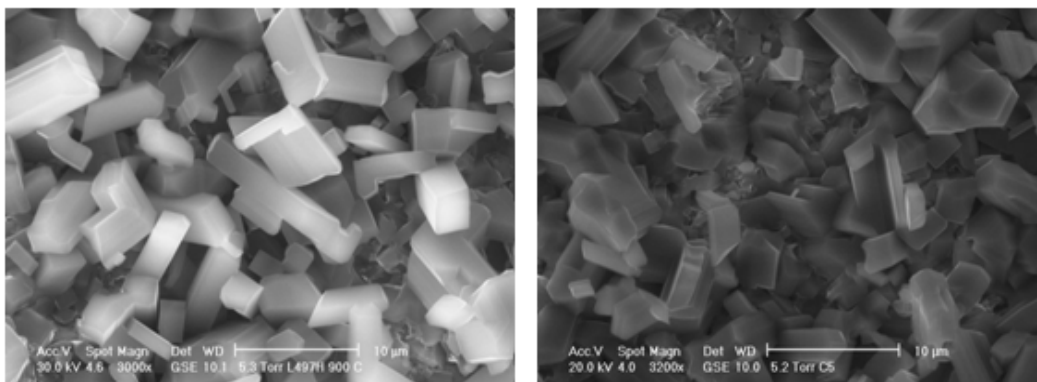


Figure 4.13- SEM image of the external oxide scale of an high energy (left) and low energy (right) ablated sample. The oxidation time is 497 h at 900 °C in both cases

However the nanocrystallization should produce new nucleation sites for oxide growth improving the scale plasticity.

The scale still displays a similar morphology in both cases (high and low energy), as shown in Fig 4.14.

A layered oxide scale was observed.

Fig 4.14 shows the oxide scale cross section of an high (left) and low (right) energy ablated sample , both oxidized for 240h at 750 °C.

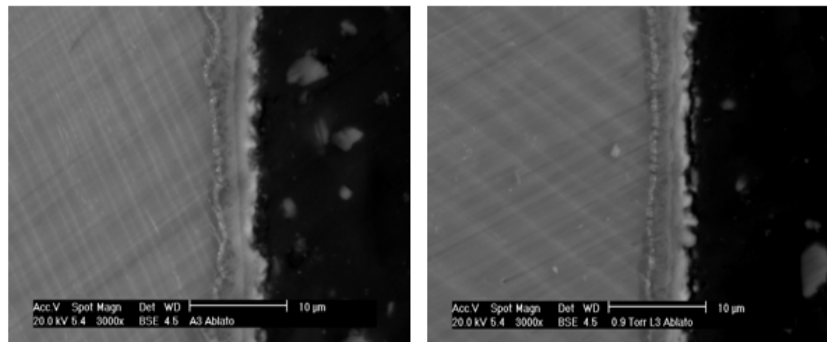


Figure 4.14- oxide scale cross section of an high (left) and low (right) energy ablated sample . oxidation time 240 h at 750 °C in both cases

Fig 4.15 shows the oxide scale cross section of an low energy sample oxidized for 240h at 750 °C ; five different layer are recognizable trough the scale :

- (1) a “bright layer “ with tungsten precipitates
- (2) an aluminium depletion zone
- (3) a titania – alumina mixed layer
- (4) an alumina-rich layer
- (5) an external TiO₂-rich layer

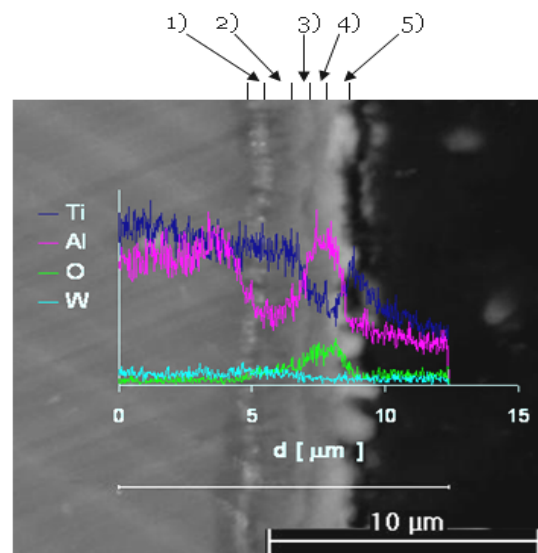


Figure 4.15 - SEM image of the oxide scale cross section of an low energy sample oxidized for 240 h at 750 °C. Qualitative concentration profiles are still displayed

The scale in the laser treated samples is similar to the scale observed on the untreated alloy surface (Fig 4.16) : the alumina rich layer is produced by the selective aluminium oxidation as the oxygen partial pressure drops down to a critical value.

This produces an aluminium local depletion favouring the successive Ti oxidation.

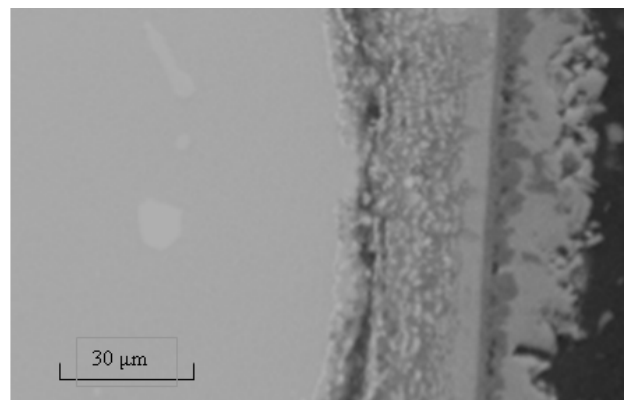


Figure 4.16- SEM image of an untreated sample oxidized for 496 h at 900 °C

At 750 °C both high energy and low energy laser ablation lead to an appreciable oxidation resistance improvement.

In Fig 4.17 the marker “NT” indicates a untreated sample.

At this temperature the low energy treatment puts the oxidation kinetic down to the 60% of the original value

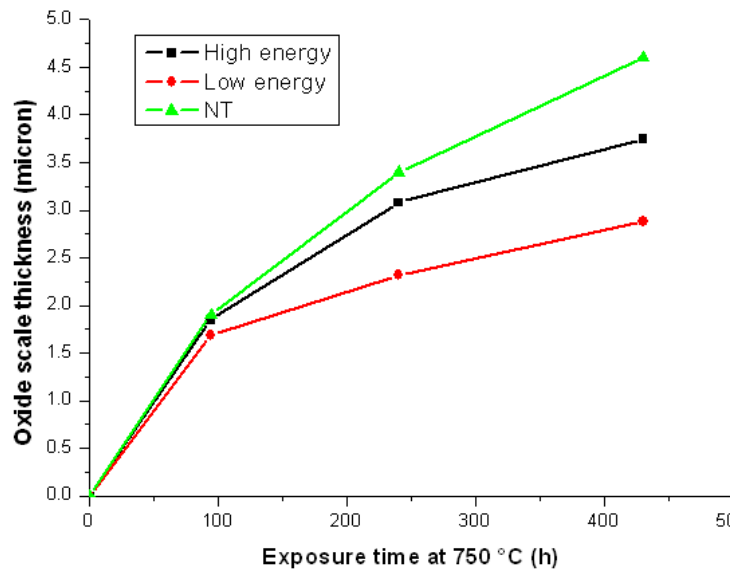


Figure 4.17 - Scale thickness versus oxidation time at 750 °C

At 900 °C the high energy treatment is unable to improve the oxidation resistance , as shown in Fig 4.18.

This is probably due to the aluminium loss via evaporation during laser ablation.

A very slight improvement was been obtained with low energy ablation.

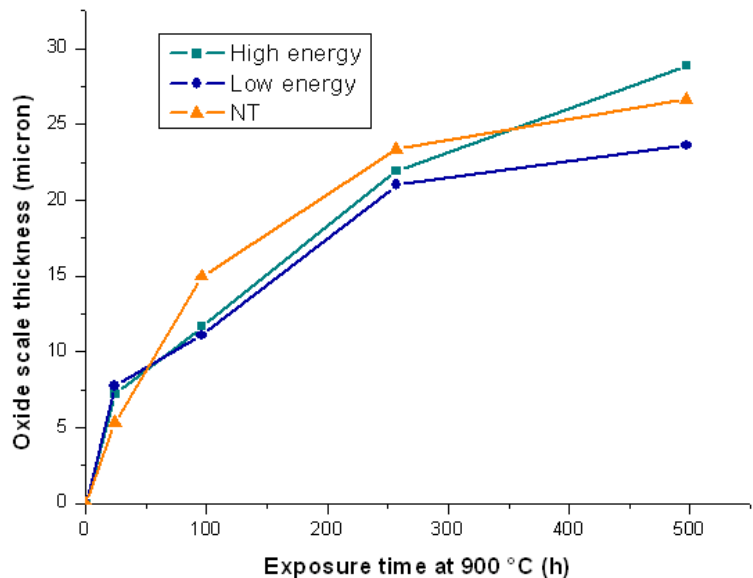


Figure 4.18 - Scale thickness versus oxidation time at 900 °C

Assuming a constant parabolic oxide growth law , we can calculate the value of “ K_p ” (oxidation parabolic parameter) : the values are given in Table 4.3

	750 °C	900 °C
Sample	$K_p [\mu\text{m} / \text{h}^{1/2}]$	$K_p [\mu\text{m} / \text{h}^{1/2}]$
AE	0.173	1.286
BE	0.117	0.969
NT	0.245	1.204

Table 4.3 - K_p values at 750 °C and 900 °C for the untreated and the laser ablated alloy

The corresponding activation energy value for these systems are given in Table 4.4 :

Sample	Q_{att} [kJ / mol]
AE	133
BE	140
NT	105

Table 4.4 – Activation energy for the Arrhenius oxidation law for the untreated and the laser ablated alloy

The activation energy is about 100kJ/mol lower as the typical activation energy for MCrAlY coatings oxidation , which is usually equal to 230-250 kJ/mol.

In order to understand the effect of laser ablation on the oxidation resistance it will be useful to define the oxide ratio (O.R.) as follows:

$$O.R. = \frac{\%Al_2O_3[at]}{\%TiO_2[at]} \quad \text{Eq 4.1}$$

We can write that :

$$\frac{1}{2} * \frac{1 - O.R.}{O.R.} = \frac{[Ti]}{[Al]} \quad \text{Eq 4.2}$$

$$[Al] + [Ti] = 100 \quad (\text{mass balance}) \quad \text{Eq 4.3}$$

substituting :

$$[Al] + [Ti] = 100 \rightarrow [Al] + \frac{[Al]}{[Al]} * [Ti] = 100 \rightarrow [Al] + [Al] * \left(1 + \frac{1}{2} * \frac{1 - O.R.}{O.R.}\right) = 100 \quad \text{Eq 4.4}$$

$$[Al] = 100 * \left(1 + \frac{1}{2} * \frac{1 - O.R.}{O.R.}\right) \quad \text{Eq 4.5(a)}$$

$$[Ti] = 100 - [Al] \quad \text{Eq 4.5(b)}$$

Eq. 4.5(a) allows us to calculate the oxide composition through the scale using the EDXS microprobe linescan as shown in Fig 4.19.

We will use a “ free kinetic “ oxidation model to describe the oxidation process in this TiAl alloy. “ Free kinetic “ means that the oxide growth rate is not determined by an average value of K_p but that the oxide growing rate is calculated as the increment of the scale thickness generated by oxidation of aluminium and titanium , separately.

To perform this task the following data are needed:

- Activation coefficients for the reaction $xM + yO \rightarrow M_xO_y$
- Hellingham diagrams for “thermodynamic limitations” in order to determine the most favoured element for the oxidation process
- Oxide forming functions that correlate the concentration at the oxidation interface and the “ resulting “ oxide
- Expansion factors for the oxidation reaction in order to calculate the scale thickness knowing the total number of oxygen atoms that have been reacted.
- The diffusivities of Al,Ti (necessary to integrate the second Fick’s equation)
- The oxygen diffusivity across the scale

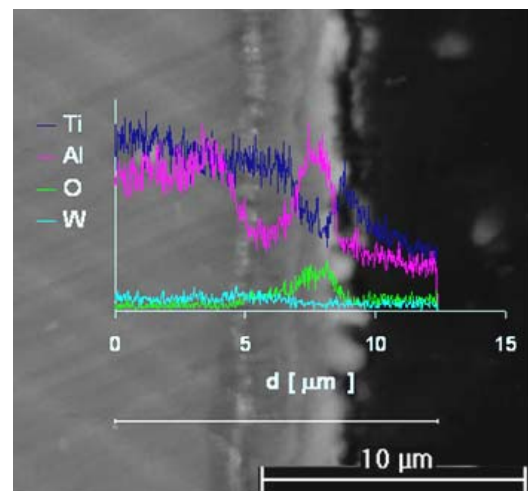


Figure 4.19- EDXS concentration profiles of Al,Ti,O,W across the external oxide scale

The flow diagram of the model is represented in Fig 4.20.

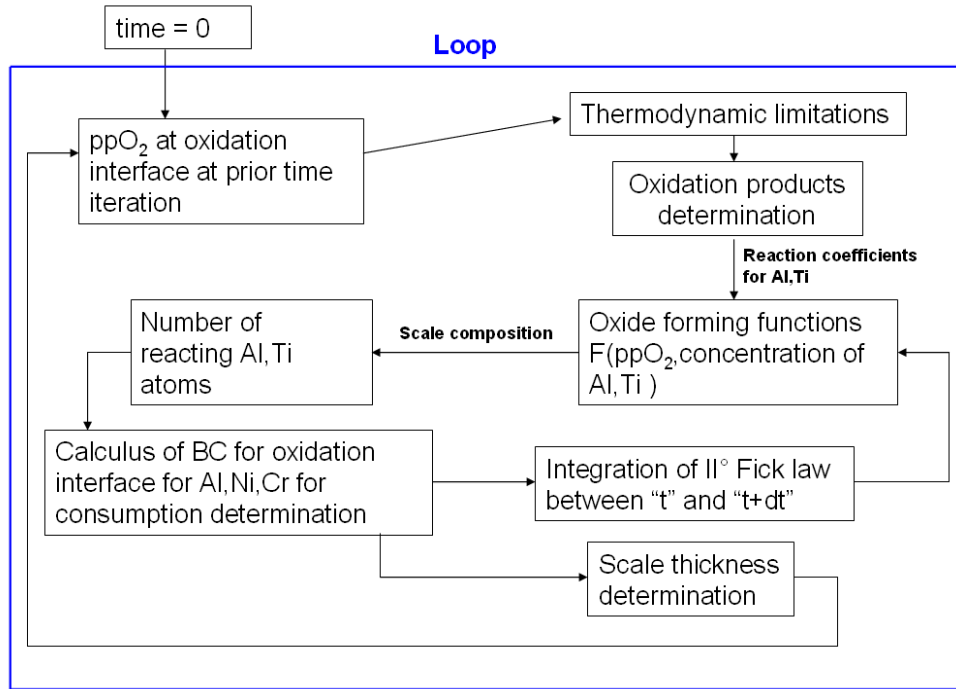


Figure 4.20- Flow diagram of the finite difference oxidative model

These assumptions were made in order to simplify the calculations :

- For the activation coefficients an Arrhenius temperature dependence is assumed :

$$\frac{\partial N}{\partial t} = K_{o,n} * \text{Exp}\left(\frac{-E_{att}}{RT}\right) * [N]^a \quad (\text{Eq 4.6})$$

Where “N” is the number of atoms that can react and [N] their concentration , expressed in at%. “a” is the “ kinetic order factor “ , taken equal to one in this work. $K_{o,n}$ is a constant

- A fully diagonal diffusion matrix in the nanocrystallized layer , in order to describe the nanocrystallized layer with only two “ equivalent “ self-diffusion terms without mixed (non diagonal) terms in the diffusivity matrix

$$[D]^{nano} = \begin{bmatrix} D_{AlAl}^{eq} & \\ & D_{TiTi}^{eq} \end{bmatrix} \quad (\text{“eq” means “equivalent “, as in Formula 4.2 , Chapter 4})$$

- A non-diagonal diffusion matrix in the microcrystalline layer

$$[D]^{micro} = \begin{bmatrix} D_{AlAl} & D_{AlTi} \\ D_{TiAl} & D_{TiTi} \end{bmatrix}$$

- A concentration independent diffusivities set , with an Arrhenius temperature dependence

$$D = D_o * Exp\left(\frac{-E_{att}}{RT}\right) \quad \text{Eq 4.7}$$

- Oxide forming functions defined as follows:

trough the TiO₂ – rich external layer $O.R. = \frac{C_{Al,\xi}^n}{C_{Al,\xi} + C_{Ti,\xi}} + f$ Eq 4.8

trough the Al₂O₃ – rich layer $O.R. = C * \frac{C_{Al,\xi}}{C_{Ti,\xi}}$ Eq 4.9

trough the second mixed layer $O.R. = \frac{C_{Al,\xi}^{n1}}{C_{Ti,\xi}} + C_1$ Eq 4.10

where $n = 0.87$; $n1 = 0.745$; $C_1 = 0.045$; $f = -0.275 + 3.5 * 10^{-4} * T_{max}$ [T_{max}]=[°C]

The symbol “ξ” means that the data is referred to the oxidation interface.

The oxidation test on the untreated alloy [44] were performed at 700 °C , 800 °C and 900 °C ; Our experimental data are :

- The oxide scale thickness
- The composition through the scale (see Fig 4.19 for an example) that allows the calculation of the oxide ratio (O.R.) using Eq. 4.5(a)
- The composition profiles through the substrate (Fig 4.21)

The composition profiles are used for the determination of the diffusivity matrix. See [50] for a more detailed description of the diffusivity calculation methods .

Four “ stop” were made for each testing temperature : 24 h , 100 h , 250 and 500 h.

A best experimental data-fitting diffusivity matrix was chosen for each testing temperature.

The results are represented by Ea. 4.11.

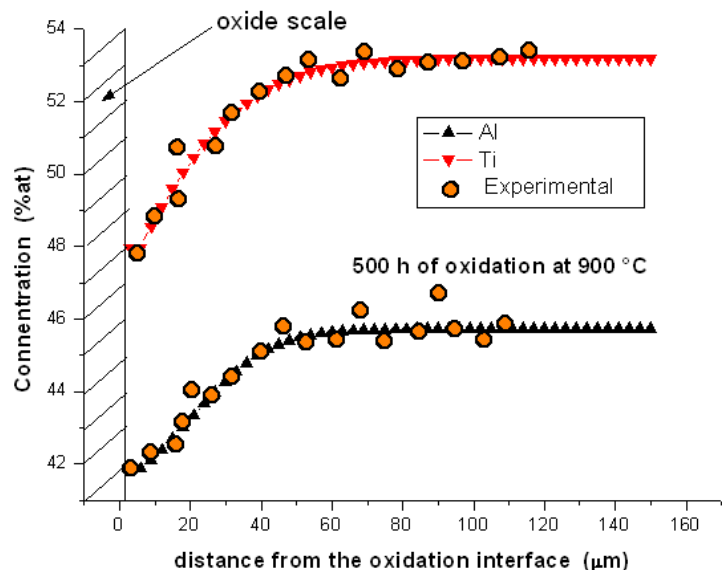


Figure 4.21 - Experimental concentration profiles through the substrate after 500 h of oxidation at 900 °C in air

Generally in a multi-component diffusion problem the diffusivity matrix does not necessarily involves one single solution. In other words a single solution is not guaranteed. This is not a problem if our solution leads to a good prediction of the interdiffusion profiles.

$$\begin{bmatrix} D_{AlAl} & D_{AlTi} \\ D_{TiAl} & D_{TiTi} \end{bmatrix} \left\{ \begin{array}{l} D_{AlAl} = 529675 * 10^{-14} * \text{Exp}\left(\frac{-200637}{RT}\right) [\text{cm}^2\text{s}^{-1}] \\ D_{AlTi} = 99675 * 10^{-14} * \text{Exp}\left(\frac{-200544}{RT}\right) [\text{cm}^2\text{s}^{-1}] \\ D_{TiTi} = 3570268 * 10^{-14} * \text{Exp}\left(\frac{-206892}{RT}\right) [\text{cm}^2\text{s}^{-1}] \\ D_{AlTi} \approx 0 [\text{cm}^2\text{s}^{-1}] \end{array} \right. \quad \text{Eq. 4.11}$$

A calculated concentration profile that will be fitted to the experimental data in order to find the “best” components of the diffusivity matrix should be coupled with the knowledge of the external boundary condition for the oxidation process : in other word we need a boundary condition (defined at every time-iteration) which is able to represent the consumption of aluminium and titanium at the oxidation interface.

An oxidation process causes a metal loss [51] and its value is

$$\xi = -V_M J_{OX} t \quad \text{Eq 4.12}$$

where V_M is the molar volume (partial molar volume) in the bulk (alloy) , J_{OX} is the diffusive flux of the metal and “t” the time

Because of the regression of the oxidation interface the flux of the metal involved in the oxidation process will be greater than the flux from the bulk of our alloy and this can be expressed writing Eq 4.13 [51] :

$$J_{ox} \Big|_{x=\xi-} = \alpha * J_{Al} \Big|_{x=\xi+} \quad \text{Eq 4.13}$$

Where “ $\xi-$ ” and “ $\xi+$ ” represents the “ left “ and the “ right “ side (the proximity-nodes) of the oxidation interface (ξ) , respectively.

“ α ” can be written as [51] :

$$\alpha = (1 - V_{Al} * C_{Al,\xi}) \quad \text{Eq 4.14}$$

and $J_{Al} \Big|_{x=\xi+}$ as :

$$J_{Al} \Big|_{x=\xi+} = -D_{AlAl} \frac{\partial C_{Al}}{\partial x} - D_{AlTi} \frac{\partial C_{Ti}}{\partial x} \quad \text{Eq 4.15}$$

Where V_{AL} is the molar volume of aluminium. We can write a similar equation for the consumption of titanium , which leads to the formation of TiO_2 .

The regression of the oxidation interface is defined through the thickness of the oxide scale (experimentally measured) : this implies now the determinability of the elemental concentration at the oxidation interface through the direct integration of the Fick’s second law .

In order to define at every time step the regression of the oxidation interface we need a time – dependent K_p , due the non-uniformity in the scale composition : this can be easily done by deriving the square-root oxidation law , obtaining Eq 4.16

$$K_p = 2 \frac{ds}{dt} \sqrt{t} \quad \text{Eq 4.16}$$

As displayed in Fig 4.23 the instantaneous value of K_p is influenced by the variations in the O.R. during oxidation.

The use in the FD model of this “ instantaneous K_p “ is limited to the “ calibration stage “ for the determination of the diffusivity matrix.

In this stage the parameter is “ common “ for aluminium and titanium ; The reason is the imposition of the experimental values of the oxide ratio : at this stage the oxide forming functions (Eq 4.8 , Eq 4.9 , Eq 4.10) are unknown without the knowledge of the diffusivity matrix .

After the calculation of the diffusivity matrix and the oxide forming functions (called “ calibration step “) Eq 4.17 and Eq 4.18 are used to determine the number of the reacted atoms instead of the “old instantaneous-common K_p ”.

The corresponding result is a scale thickness prediction which allows the calculation of the “ global instantaneous K_p “

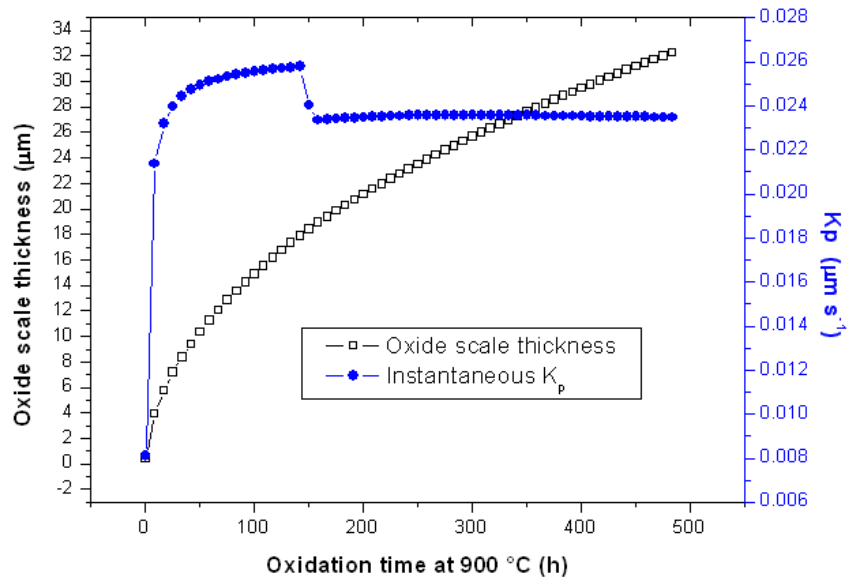


Figure 4.22 - Instantaneous value of K_p for untreated TiAl alloy in the case of oxidation at 900 °C

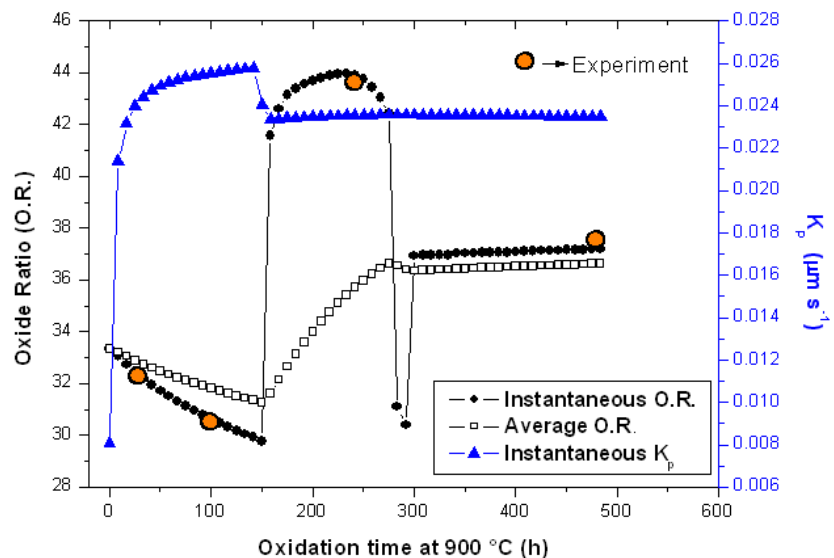


Figure 4.23 - Instantaneous value of K_p , Instantaneous O.R and Average O.R. for untreated TiAl alloy in the case of oxidation at 900 °C

The knowledge of the oxide scale thickness (s) and its composition allows the determination of the p_{O_2} (oxygen partial pressure) at the oxidative interface through Eq 4.17 , where D_{O,Al_2O_3} and D_{O,TiO_2} are the permeabilities [103] [104] of oxygen through pure alumina and titania , respectively.

$$ppO_2 = 0.21[\text{bar}] * \frac{O.R. * D_{O,AL2O3} + (1 - O.R.) * D_{O,TiO2}}{s} \quad \text{Eq 4.17}$$

At this point the number of the reacting atoms is given by :

$$\left\{ \begin{aligned} \frac{\partial N_{Al}}{\partial t} &= \frac{3}{2} * K_{o,n}^{Al} * \text{Exp}\left(\frac{-E_{att}^{Al}}{RT}\right) * [N_{Al}]^a * O.R. \\ \frac{\partial N_{Ti}}{\partial t} &= \frac{1}{2} * K_{o,n}^{Ti} * \text{Exp}\left(\frac{-E_{att}^{Ti}}{RT}\right) * [N_{Ti}]^a * (1 - O.R.) \end{aligned} \right. \quad \text{Eq 4.18}$$

$$\left\{ \begin{aligned} \frac{\partial N_{Al}}{\partial t} &= \frac{1}{2} * K_{o,n}^{Ti} * \text{Exp}\left(\frac{-E_{att}^{Ti}}{RT}\right) * [N_{Ti}]^a * (1 - O.R.) \\ \frac{\partial N_{Ti}}{\partial t} &= \frac{3}{2} * K_{o,n}^{Al} * \text{Exp}\left(\frac{-E_{att}^{Al}}{RT}\right) * [N_{Al}]^a * O.R. \end{aligned} \right. \quad \text{Eq 4.19}$$

Obviously the last set of equations (Eq 4.18 ; Eq 4.19) must satisfy the following condition (written for the node which instantaneously represents the oxidation interface) :

$$\frac{\partial N_{Al}}{\partial t} dt + \frac{\partial N_{Ti}}{\partial t} dt \leq J_{Ox,\xi} * dt \quad \text{Eq 4.20}$$

where $J_{Ox,\xi}$ is the flux of oxygen atoms trough the oxidative interface ;

In order to impose the condition given by Eq. 4.20 a scaling factor is eventually applied to Eq 4.18 and Eq. 4.19 The “ ≤ “ symbol derives from the fact that the oxidation interface moves itself into the substrate. The “external oxidation condition “ is implicit in the model.

For the oxygen diffusion calculation ten nodes were placed across the oxide scale : the oxygen diffusivity trough the scale is calculated as the weighted average diffusivity between the diffusivity of oxygen trough alumina and titania. Eq 4.18 and Eq 4.19 are used to determine the external boundary condition for the second Fick’s law integration.

Thermodynamic limitations are also placed in the Finite Difference (FD) model in order to prevent the formation of the less – stable oxide.

The oxygen partial pressure at which the oxidation process begins can be calculated as the intersection between the free-energy variation line (black line) for each metal and the “ray” emanated from “0” (dashed black line) with the corresponding slope (indicated by the intersection on the Partial pressure of oxygen “ elbow axis “)

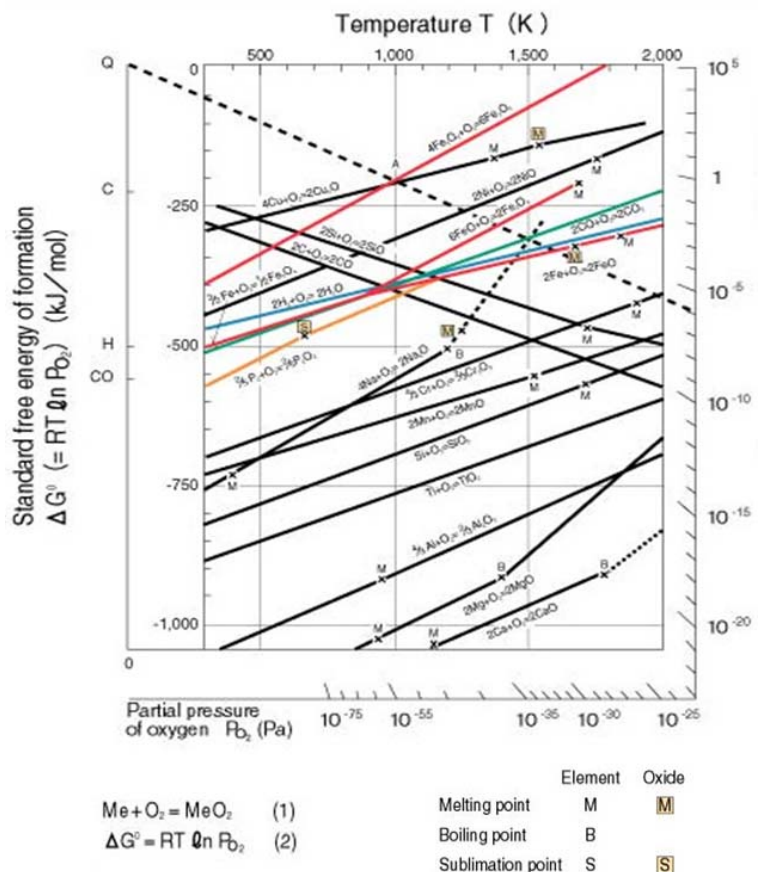


Figure 4.24- Hellingham diagram for the most common metals

Actually, in the assumed oxidative model only the formation of Al_2O_3 and TiO_2 is allowed: from a general point of view we should consider all phases in the Ti-Al-O diagram.

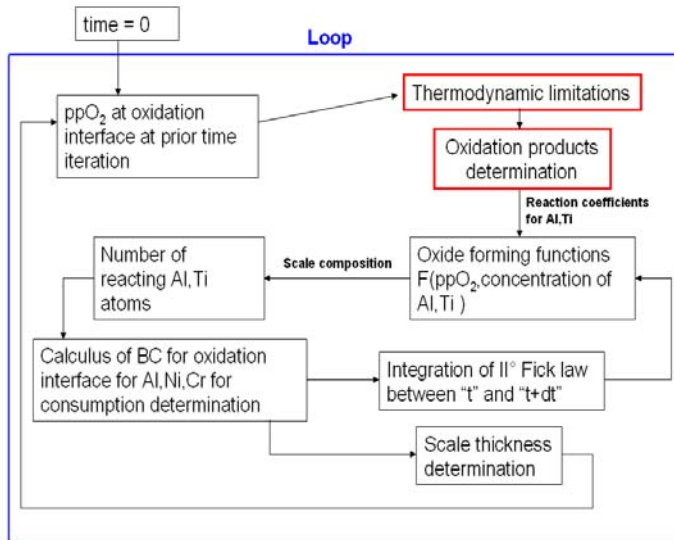


Figure 4.25- Flow diagram of the finite difference oxidative model (thermodynamic steps are highlighted by red squares)

The ppO_2 at the oxidative interface is the most important factor in order to identify the most thermodynamically stable phase.

This step is highlighted in Fig 4.25 by the red squares.

The Al -O binary system

The Ti-Al-O system has been studied by several investigators because of the importance of Ti and its alloys and of intermetallic compounds as structural materials as well as matrix materials for composites with alumina (Al_2O_3) as a reinforcement material.: isothermal sections at several temperatures have been reported.

Studies on the sequence of the product layer in the interfacial reaction zone of the Ti/ Al_2O_3 diffusion couples have been carried out to determine the phase relationships in the Ti-Al-O system.

In the Al-O binary phase diagram (Fig. 4.26), the equilibrium phases are :

- the liquid Al at the Al-rich end
- the liquid Al_2O_3 near the O-rich end
- the fcc terminal solid solution, Al, with a small, unknown solubility of oxygen
- the hexagonal aluminum oxide, $\alpha\text{-Al}_2\text{O}_3$ (α -alumina or corundum) with small, but unknown deviations from the stoichiometric composition
- the gas

The monotectic reaction, $\text{Al}_2\text{O}_3(\text{Liq}) \leftrightarrow \text{Al}(\text{Liq}) + \alpha\text{-Al}_2\text{O}_3$, occurs at $\approx 2046.5 \pm 7.5$ °C where oxygen contents in $\text{Al}_2\text{O}_3(\text{Liq})$, $\text{Al}(\text{Liq})$, and $\alpha\text{-Al}_2\text{O}_3$ are 59.5 ± 0.5 , ≈ 0.1 and ≈ 60 at.%, respectively.

The reaction $\text{Al}(\text{Liq}) \leftrightarrow \text{Al} + \alpha\text{-Al}_2\text{O}_3$ is probably eutectic and occurs at ≈ 660 °C where oxygen concentration in Al and $\alpha\text{-Al}_2\text{O}_3$ are $3 \cdot 10^{-8}$ (maximum) and 60 at.%, respectively.

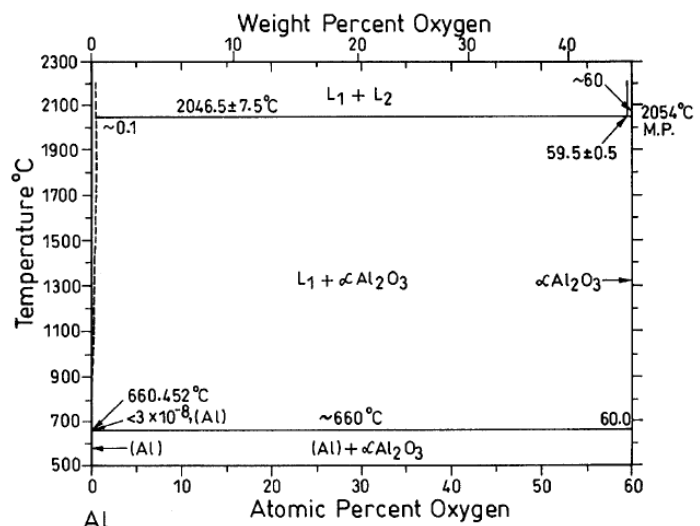


Figure 4.26- Al-O binary phase diagram

Ti-O binary system

In the Ti-O binary phase diagram (Fig. 4.27), the condensed phases are included in the composition range between pure Ti and TiO₂. Oxygen has a high solubility in α-Ti at low temperatures and thus stabilizes α-Ti with respect to the high temperature bcc form, β-Ti. At low temperatures the cph phases, Ti₂O, Ti₃O and possibly Ti₆O, are reported to form.

Ti₂O forms by the peritectoid reaction, α-Ti + Ti₃O₂ ↔ Ti₂O at ≈ 600 °C where oxygen contents of α-Ti, Ti₃O₂, and Ti₂O are 33.3, 40, and 33.9 at.%, respectively.

The formation of Ti₃O occurs by the peritectoid reaction, α-Ti + Ti₂O ↔ Ti₃O at ≈ 500 °C where oxygen contents of α-Ti, Ti₂O, and Ti₃O are ≈ 17, ≈ 25, and ≈ 24.5 at.%, respectively. A peritectic reaction, Liq + α-Ti ↔ γ-TiO occurs at 1770 °C where oxygen contents of the L, α-Ti, and γ-TiO are ≈ 55, 31.4, and 34.5 at.%, respectively. The γ-TiO transforms to β-TiO at ≈ 1250 °C.

The α-TiO forms by the peritectoid reaction, α-Ti + β-TiO ↔ α-TiO at 940 °C where the oxygen contents of α-Ti, β-TiO, and α-TiO are 33.3, 51, and 50 at.%, respectively.

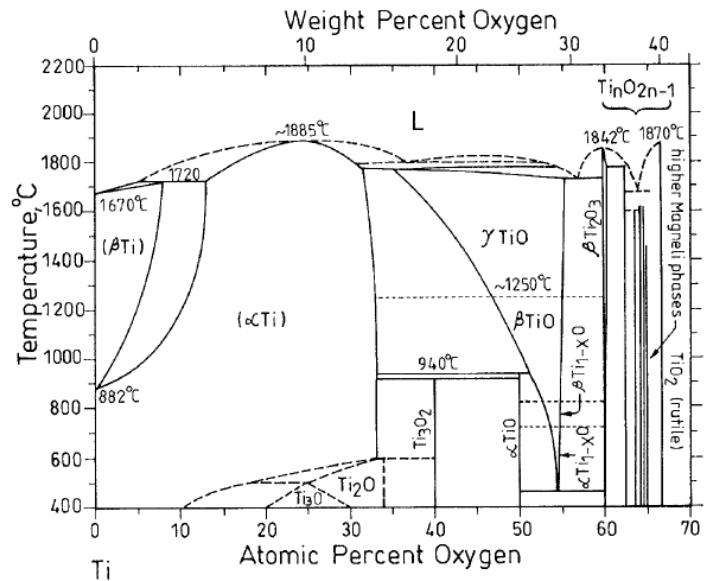


Figure 4.27 - Ti-O binary phase diagram

Ti₃O₂ forms by the peritectoid reaction, α-Ti + α-TiO ↔ Ti₃O₂ at 920 °C where the oxygen contents of α-Ti, α-TiO, and Ti₃O₂ are 32.4, 50, and 40 at.%, respectively. β-Ti₃O₅ forms by a peritectic reaction, Liq + β-Ti₂O₃ ↔ β-Ti₃O₅ where the oxygen contents of Liq, β-Ti₂O₃, and β-Ti₃O₅ are 63, 60.2, and 62.5 at.%, respectively. At 1842 °C and 60 at.% O, β-Ti₂O₃ is formed by the congruent reaction, Liq ↔ β-Ti₂O₃. TiO₂ also forms by a congruent reaction, Liq ↔ TiO₂ at 1870 °C and 66.7 at.% O.

The system Ti-O also forms Magneli phases that are represented by the formula Ti_nO_{2n-1} [67]. A portion of the calculated Ti-O phase diagram showing in detail a cascade of peritectic equilibria with Magneli phases is shown in Fig. 4.28

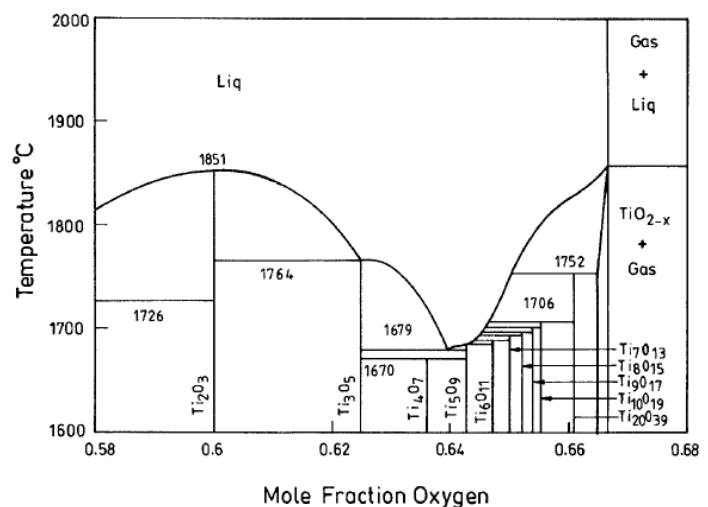


Figure 4.28 Ti-O binary phase diagram showing in detail a cascade of peritectic equilibria [98]

Solid Phases

The crystal structure data of the binary equilibrium phases in the Ti-Al-O system are shown in Table 4.5

There are several thermodynamic evaluations available on the Ti-O phase diagram [68], [69], [70], [71], [72], [73], [74], [75] as well as on the Ti-Al system [68], [69], [76], [77], [78], [79]. The free energies of formation of the main phases in the Ti-Al-O system as given by [80] and [81] are presented in Table 4.6.

Composition	Pearson's Symbol	Space Group	Prototype	Parameters, nm			Compounds	ΔG^0 , at 1000 °C J/g atom	ΔG^0 , at 1100 °C J/mol
				a	b	c			
α -Ti(O,Al)	<i>hP2</i>	<i>P6₃/mmc</i>	Mg	0.29508	...	0.46855	1/3 Ti ₂ O	-146 502.0	...
β -Ti	<i>cI2</i>	<i>Im3m</i>	W	0.33065	1/2 α -TiO	-210 701.0	...
TiAl	<i>tP4</i>	<i>P4/mmm</i>	AuCu	0.4005	...	0.4070	1/2 β -TiO	-210 961.0	-205 907.0
TiAl ₂	<i>tI24</i>	<i>I4₁/amd</i>	Ga ₂ Hf	0.3976	...	2.4360	1/5 Ti ₂ O ₃	-234 463.0	-229 223.0
TiAl ₃	<i>tI8</i>	<i>I4/mmm</i>	Al ₃ Ti	0.3848	...	0.8596	1/8 Ti ₃ O ₅	-234 357.0	-232 032.0
Ti ₃ Al	<i>hP8</i>	<i>P6₃/mmc</i>	Ni ₃ Sn	0.5782	...	0.4629	1/3TiO ₂	-238 276.0	-231 994.0
TiO	<i>cF8</i>	<i>Fm3m</i>	NaCl	0.4180	α -Ti(O) [Ti _{0.915} O _{0.085}]	...	-44 272
Ti ₂ O	<i>hP3</i>	<i>P3m1</i>	CdI ₂	0.296	...	0.483	α -Ti(O) [Ti _{0.67} O _{0.33}]	...	-152 000
Ti ₃ O	<i>hP16</i>	<i>P31c</i>	Ti ₃ O	0.515	...	0.956	1/11Ti ₄ O ₇	...	-231 664
Ti ₂ O ₃	<i>hR10</i>	<i>R3c</i>	Al ₂ O ₃	0.51580	...	1.3611	1/4Ti ₃ Al	-17 257.5	-18 377.0
Ti ₃ O ₂	<i>hP6</i>	<i>P6/mmm</i>	...	0.4991	...	0.2879	1/2TiAl	-27 179.2	-26 165.0
TiO ₂	<i>tP6</i>	<i>P4₂/mnm</i>	TiO ₂	0.45937	...	0.29619	1/3TiAl ₂	-27 666.0	-26 000.0
Al	<i>cF4</i>	<i>Fm3m</i>	Cu	0.40488	1/4TiAl ₃	-18 687.8	-23 007.0
Al ₂ O ₃	<i>hR10</i>	<i>R3c</i>	Al ₂ O ₃	0.4754	...	1.299	1/5Al ₂ O ₃	-254 273.0	...
							Ti _{0.668} Al _{0.222} O _{0.11}	...	-68 272.0
							Ti _{0.485} Al _{0.485} O _{0.03}	...	-39 837.0

Table 4.5 - Crystal structures of solid phases in the Ti-Al-O phase diagram

Table 4.6 – Thermodynamic data for relevant phases in the Ti-Al-O phase diagram

A simplified 900 °C isothermal section of Ti-Al-O system is shown in Fig. 4.29 [84]. Intermetallic compounds like Ti₃Al, TiAl, and TiAl₃ are considered in this estimated diagram as line compounds and this is the inherent limitation of this diagram.

The earliest evaluation of the Ti-Al-O system has been made by Tressler et al. [82] at 871 °C. Further investigations on the Ti-Al-O system at 800 °C were performed in [83]. Authors [83] have mentioned that they did not consider phases like Ti₃O because they are metastable. However, as per the binary phase diagram this phase does not exist above 500 °C.

One necessary, but not sufficient, prerequisite for the formation of a dense and continuous scale of Al₂O₃ on the surface of an alloy is that this oxide be the most stable of all possible oxides, otherwise it would be reduced by the base metal or other components of the alloy. Thermodynamic calculations of the oxide stabilities have to take into account the activities of the various components of the alloy, and, if necessary, those of the oxide, too. Fortunately, oxides as Al₂O₃ (and SiO₂) are among the most stable oxides, otherwise their slow growth rate could not be used to protect alloys.

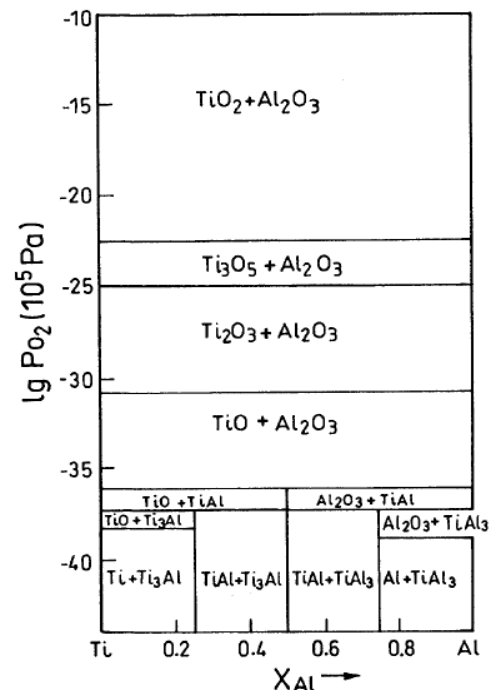


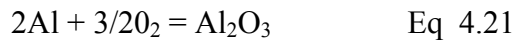
Figure 4.29 - An estimated isothermal section of the Ti-Al-O ternary diagram [84]

The situation is distinctly different if intermetallic phases with titanium as one of the main components are considered. Two aspects are important:

1. Oxygen equilibrium pressures of Al/Al₂O₃ and Ti/TiO are very similar [84]
2. The activities of metals in systems with intermetallic phases can depart strongly from ideal (Raoultian) behavior, as for example, in the Ni-Al system. [99],[100]. This, again, strongly affects the oxygen pressure of the metal/oxide equilibria, as will be shown in the following.

From this introduction it follows that correct statements on the stability of oxides on intermetallics can be made only if the activity variation of the metals in the system under consideration is known. The activities of Ti and Al in the binary Ti-Al system have been calculated using existing thermodynamic data. Thus, the essential prerequisites for estimating oxide stabilities in these two systems are available.

The activity variation of Al and Ti in the Ti-Al system at 700, 900, and 1100 °C is shown in Fig. 4.29. These values are based on data in [101]. Very large deviations from ideal behaviour exist, which increase with decreasing temperature. This is to be expected because the binding forces in the intermetallics increase with decreasing temperature. The activities remain constant in two-phase regions. Greater changes occur in the stability ranges of the various single phases. The exact activity behavior in a single-phase region has not been estimated, because it did not appear to be critical for the following considerations. The oxygen equilibrium pressure of a metal/oxide mixture can be calculated from the free energy of formation, ΔG, of the corresponding reaction of oxide formation. For the formation of Al₂O₃ :



$$\Delta G_1 = RT \ln K_1 \quad \text{Eq 4.22}$$

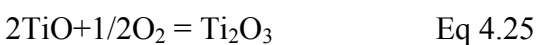
with the equilibrium constant

$$K_1 = \frac{a_{\text{Al}_2\text{O}_3}}{a_{\text{Al}}^2 P_{\text{O}_2}^{3/2}} \quad \text{Eq 4.23}$$

To form a pure oxide from a pure metal (i.e., for $a_{\text{Al}} = a_{\text{Al}_2\text{O}_3} = 1$), it follows from eq 4.22 and 4.23:

$$\ln P_{\text{O}_2}(\text{Al} / \text{Al}_2\text{O}_3) = \frac{2\Delta G}{3RT} \quad \text{Eq 4.24}$$

In a similar manner, for an equilibrium between two oxides of one metal (e.g., TiO and Ti₂O₃), according to the reaction :



and the equilibrium constant

$$K_5 = \frac{a_{\text{Ti}_2\text{O}_3}}{a_{\text{Ti}}^2 P_{\text{O}_2}^{1/2}} \quad \text{Eq 4.26}$$

$$\ln P_{\text{O}_2}(\text{TiO} / \text{Ti}_2\text{O}_3) = \frac{2\Delta G_5}{RT} \quad \text{Eq 4.27}$$

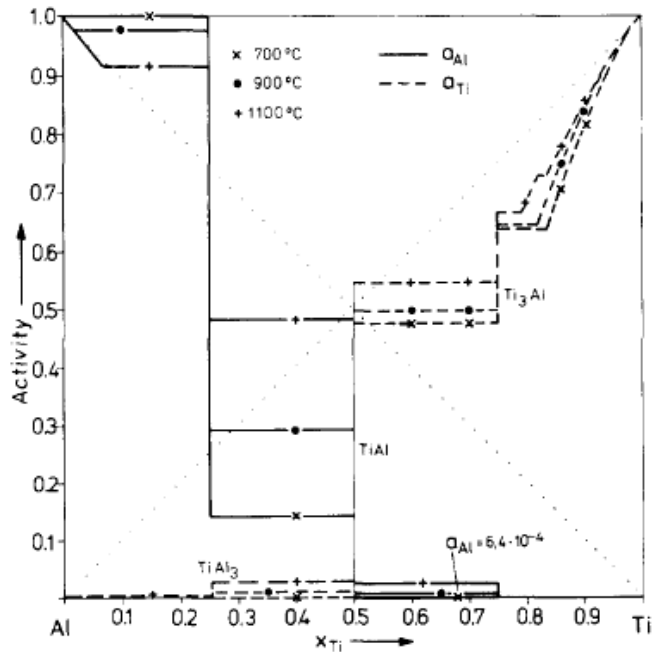


Figure 4.29 Variation of the activity of Al and Ti in the Ti-Al system

Oxygen equilibrium pressures calculated with this method are given in Figs. 4.30 for selected metal/oxide and oxide/oxide equilibria as functions of the reciprocal absolute temperature. For these calculations, data from the thermodynamic databank THERDAS (THERDAS –Thermodynamische Datenbank für Anorganische Stoffe - is a project of the Lehrstuhl für Theoretische Huettenkunde und Metallurgie der Kernbrennstoffe of the Technische Hochschule Aachen.) were used and the activities of metal and oxide were set to one. For the following calculations of the equilibrium pressures of Al/Al₂O₃ and Ti/TiO across the Ti-Al system, the assumption was made that TiO and Al₂O₃ exist as pure oxides (i.e., a_{TiO} = a_{Al₂O₃} = 1). It then follows from Eq 4.23 that :

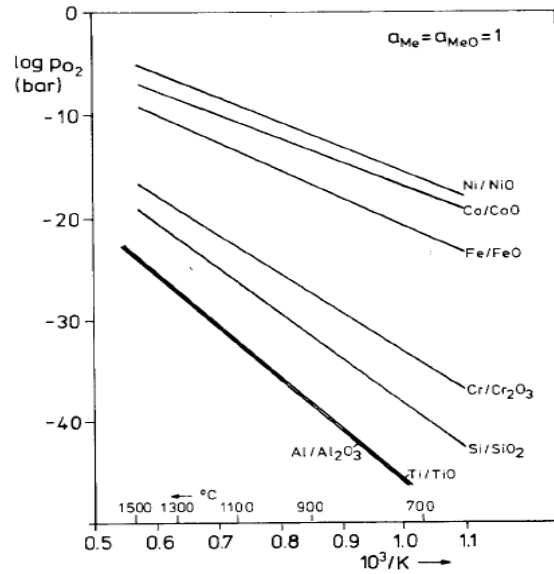


Figure 4.30 Oxygen equilibrium pressures of selected pure metal/oxide systems.

$$\log PO_2 = 2/3 \log K_1 - 3/4 \log a_{Al} \quad \text{Eq 4.28}$$

In an analogous manner for the reaction: $Ti + 1/2 O_2 = TiO$ Eq 4.29

with
$$K_9 = \frac{a_{TiO}}{a_{Ti} PO_2^{1/2}} \quad \text{Eq 4.30}$$

it follows that :
$$\log PO_2 = -2 \log K_1 - 2 \log a_{Ti} \quad \text{Eq 4.31}$$

If the corresponding data for K and a_{Al} or a_{Ti} are introduced into Eq 4.28 and Eq 4.31 , the results are summarized in Table 4.7 The exact variation in the α-Ti and β-Ti phases has been neglected, because it was not important for the ensuing considerations. A graphical representation is given in Fig. 4.31 for 900 °C and the course is very similar at 700 and 1100 °C.

Phases	Temp. (°C)	a _{Al}	P _{O₂} (Al/Al ₂ O ₃) (bar)	a _{Ti}	P _{O₂} (Ti/TiO) (bar)
Ti (x _{Ti} =0.9)	700	5.3 E-5	5.0 E-43	0.815	7.5 E-48
	900	4.7 E-4	7.9 E-35	0.890	7.1 E-39
	1100	3.0 E-3	1.7 E-26	0.905	7.7 E-33
Ti+Ti ₃ Al	700			0.634	1.2 E-47
	900			0.645	7.9 E-39
	1100			0.665	1.4 E-32
Ti ₃ Al+TiAl	700	6.4 E-4	1.8 E-44	0.475	2.2 E-47
	900	5.0 E-3	3.5 E-36	0.495	2.0 E-38
	1100	0.02	1.4 E-27	0.545	2.2 E-32
TiAl+TiAl ₃	700	0.14	1.4 E-47	0.002	2.5 E-45
	900	0.29	1.5 E-38	0.010	5.0 E-35
	1100	0.48	1.9 E-29	0.025	1.0 E-29
TiAl ₃ +Al	700	0.915	1.1 E-48		
	900	0.980	3.0 E-39		
	1100	0.995	7.4 E-30		

Table 4.7 - Activities in the Ti-Al System and Metal/Oxide equilibrium pressures

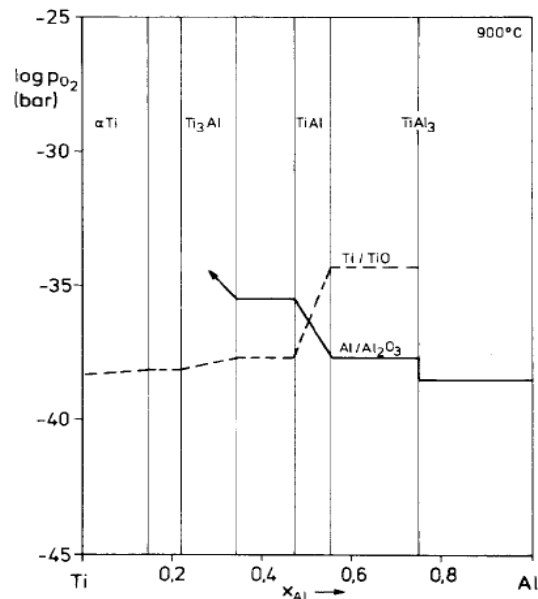


Figure 4.31 Variation of the metal/oxide equilibrium pressures in the Ti-Al-O system at 900 °C

From Table 4.7 and Fig. 4.31 it follows that:

- In the two-phase regions Al/TiAl₃ and TiAl/TiAl₃, the oxygen pressure of Al/Al₂O₃ is several orders of magnitude below that of Ti/TiO. Here Al₂O₃ is the most stable oxide.
- In the existence range of the TiAl phase, the oxygen pressure of Al/Al₂O₃ increases, that of Ti/TiO decreases dramatically, so that both pressures intersect. Consequently, in the two-phase region Ti₃Al/TiAl, the oxide TiO is more stable than Al₂O₃.
- The difference in the oxygen pressures of Ti/TiO and Al/Al₂O₃ increases within the Ti₃Al phase, and then even more within both α -Ti and β -Ti.

The formation of a continuous Al₂O₃ scale is not to be expected if the composition of the alloy is in the two-phase region Ti₃Al/TiAl. This corresponds with our own experimental observations. During the oxidation experiment, a Ti₃Al zone was often formed underneath the scale, which further favours TiO stability.. From studies of the oxidation of titanium it is known, however, that the main reaction product is TiO₂, and that TiO, Ti₂O₃, and the Magneli phases, with the general formula Ti_xO_{2x-1}, are oxidized rapidly to TiO₂, or that the formation of these oxides is retarded due to slow phase-boundary reactions [102] The same appears to apply to the oxidation of TiAl, because according to the literature and our observations TiO₂ and Al₂O₃ are the reaction products observed.

The formation of a continuous protective Al₂O₃ scale should be favoured by:

- Increase in the Al content up to or even above the TiAl/TiAl₃ equilibrium composition, because the alloy is then in equilibrium with Al₂O₃. The selective oxidation of Al to form the protective scale can nevertheless decrease the Al content in the subsurface zone below the critical value of Al₂O₃ stability.
- Alloying of TiAl with components which decrease the Ti activity and increase the Al activity.

The formation of Al₂O₃ on the surface leads to Al depletion on the sub-surface layer resulting in the formation of a new stoichiometric ternary phase, known as X-phase or Z-phase, in the sub-surface layer. Table 4.8 [85] briefly summarizes the results of different authors.

Reference	Composition Ti:Al:O[at%]	Crystal Symmetry	Lattice parameters	Experimental conditions
[86]	50:30:20	Cubic	a = 69 nm	Ti48Al at 900 °C in Ar + 20% O ₂
[87]	37.5 : 25: 37.5 ± 10	Cubic SG: P ₄ 32	a = 69 nm	Ti47Al at 1000 °C in O ₂
[88]	54 : 31 : 15 ± 5	Cubic	a = 69 nm	Ti50Al at 1000 °C in air

Table 4.8 - Literature Survey on X-Phase Determination

Figure 4.32 shows the calculated isothermal phase diagram of Ti-Al-O system at 900 °C including the ternary X-phase [88].

Figure 4.33 shows a part of the calculated isothermal phase diagram of the Ti-Al-O system at 900 °C with chemical potentials of oxygen and aluminium as axes (also known as potential phase diagram), including four calculated diffusion paths (t₁-t₄) [89].

Time of oxidation for path $t_4 >$ that for path $t_3 >$ that for path $t_2 >$ that for path t_1 . According to Kussmaul et al. [89] the layer sequence of a γ -TiAl and Al_2O_3 diffusion couple will change with time in the following manner:

- path t_1 : γ -TiAl/ Al_2O_3
- path t_2 : γ -TiAl/X/ Al_2O_3
- path t_3 : γ -TiAl/ α_2 - Ti_3Al /X/ Al_2O_3
- path t_4 : γ -TiAl/ α_2 - Ti_3Al / Al_2O_3

The calculated diffusion paths t_1 , t_2 , and t_3 [89] agree well with the experimental data of Dettenwanger et al. [88]. However, no experimental data could be found that matches with path t_4 .

Another relevant phase in the Ti-Al-O phase diagram is aluminum titanate (Al_2TiO_5): a well-known high temperature shock resistant and low thermal expansion material, is widely used as refractory linings for transportation and storing of liquid metals.

This Al_2TiO_5 undergoes a eutectoid like decomposition to α - Al_2O_3 and TiO_2 (rutile). There have been various reports in the literature about this decomposition temperature: 1237 ± 10 °C [90], 1200 °C [91], [92], 1262 ± 7 °C [93], 1240 °C [94], 1295 ± 10 °C [95], and 1280 ± 1 °C [96].

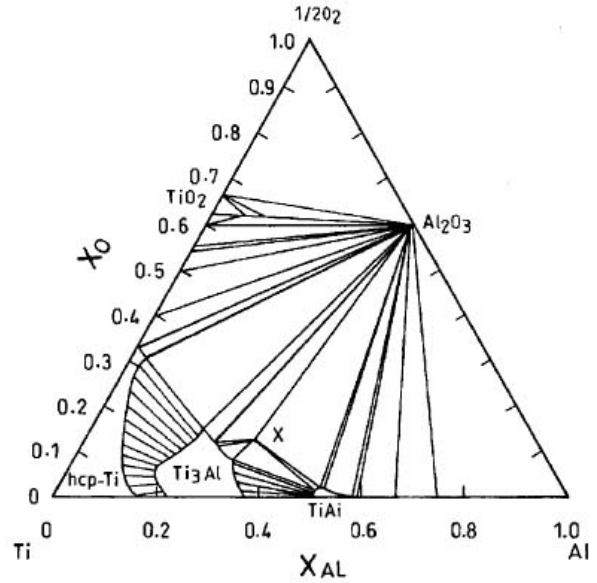


Figure 4.32 - Calculated isothermal section of the Ti-Al-O ternary system at 900 °C including the ternary X-phase

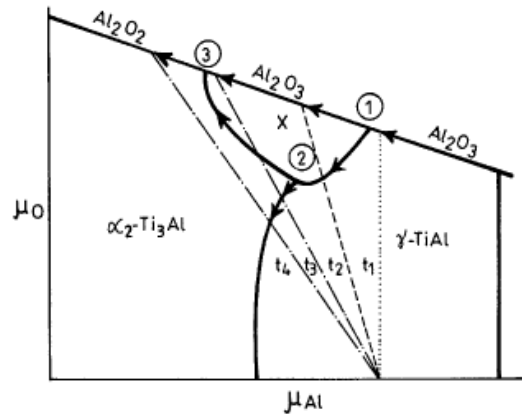
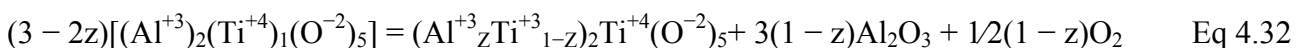


Figure 4.33 - Calculated isothermal section of the Ti-Al-O ternary system at 900 °C with chemical potentials of oxygen and aluminum as axes including four calculated diffusion paths

Seifert and Aldinger [97] report that decomposition of Al_2TiO_5 to Al_2O_3 and TiO_2 takes place below 1573 K. It has also been reported [97] that the composition and hence mechanical properties are strongly influenced by the oxygen partial pressure of the surrounding atmosphere.

Aluminium titanate, which can be also expressed as $(\text{Al}^{+3})_2(\text{Ti}^{+4})_1(\text{O}^{-2})_5$, is a stoichiometric phase at high oxygen pressure [97]. With decreasing oxygen pressures the stoichiometric Al_2TiO_5 decomposes to a reduced form of aluminium titanate, corundum, and oxygen. The decomposition reaction can be written as:



As the oxygen potential decreases ($z \rightarrow 0$), the decomposition reaction finally yields the titanium oxide Ti_3O_5 and corundum.

Figure 4.34 shows the calculated phase diagram $\text{TiO}_2\text{-AlO}_{1.5}$ for an oxygen partial pressure of 0.21 [bar] (air) [97].

Figure 4.35 shows the calculated phase diagram $\text{Ti}_x\text{O}_y\text{-AlO}_{1.5}$ for an oxygen partial pressure of 2.5×10^{-9} bar [97].

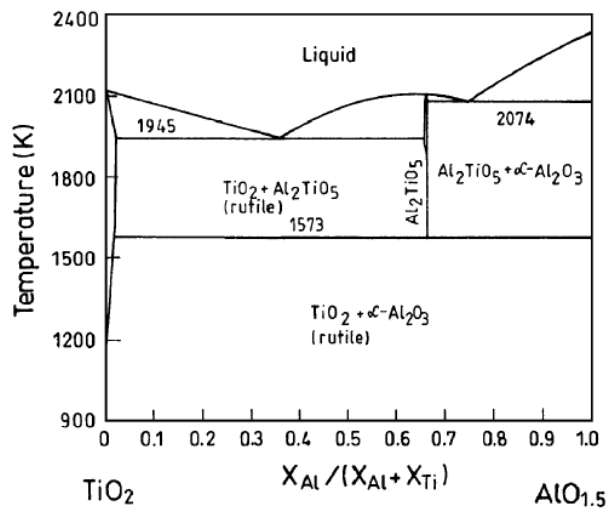


Figure 4.34 - Calculated phase diagram $\text{TiO}_2\text{-AlO}_{1.5}$ for an oxygen partial pressure of 0.21 bar (air)

Here (Fig 4.35), Ti_xO_y represents the different titanium oxides depending on the temperature. The dash line in the figure indicates the stoichiometric composition (Al_2TiO_5), and $(\text{Al}^{+3}_z \text{Ti}^{+3}_{1-z})_2 \text{Ti}^{+4} (\text{O}^{-2})_5$ denotes the reduced form of aluminium titanate.

Since the Magneli phases and Ti_4O_7 shows limited stability, they have not been considered in this calculated phase diagram.

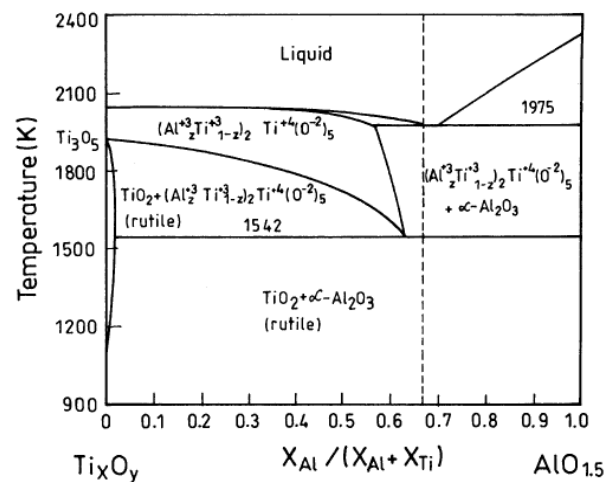


Figure 4.35 - Calculated phase diagram $\text{Ti}_x\text{O}_y\text{-AlO}_{1.5}$ for an oxygen partial pressure of 2.5×10^{-9} bar

As the oxygen partial pressure decreases from 0.21 bar to 2.5×10^{-9} bar, the important differences between two phase diagrams are (1) the homogeneity range of aluminium titanate phase is drastically extended; (2) the stoichiometric composition Al_2TiO_5 (dashed line in Fig. 4.35) is now located in the two-phase field (aluminium titanate + corundum); and (3) the decomposition temperature decreases by 31 K. With decreasing oxygen partial pressure stoichiometric compound Al_2TiO_5 decomposes into corundum and a reduced form of aluminium titanate, and with even lower oxygen pressure it decomposes to corundum and Ti_2O_3 .

At this point we can represent the nanocrystallized system as follows:

As displayed in Fig 4.36 the aluminium concentration in the laser ablated layer is lower than in the untreated zone : this fact is due to aluminium evaporation during laser local heating.

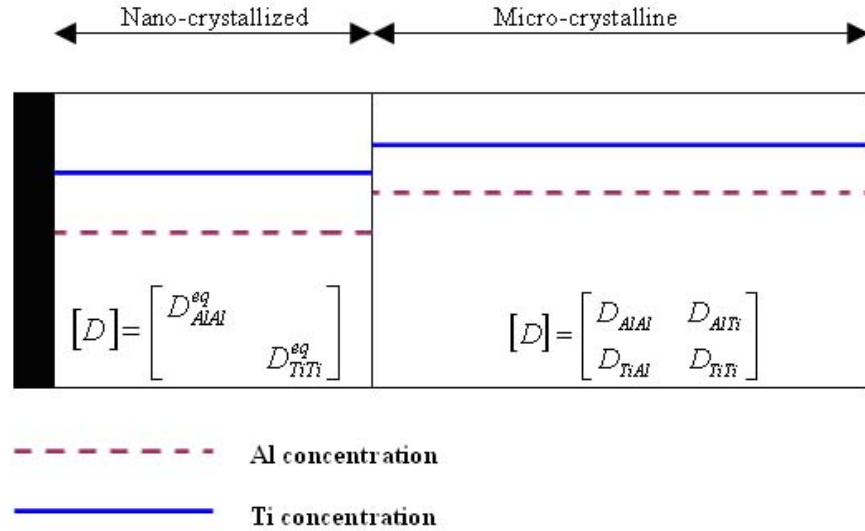


Figure 4.36 – Implementation of the nanocrystalline model with a two-layer (nano + micro) structure

Using as the diffusivity through the laser - modified layer (only for the D_{11} and D_{22} elements) the expression for the “ equivalent “ diffusivity (Eq 4.2 , Chapter 4)

$$D_{eq}^{Al} = \frac{\sqrt{3}\delta d D_{gb}^{Al} + \frac{\sqrt{3}}{2}(d - \delta)d D_g^{Al}}{\sqrt{3}\delta d + \frac{\sqrt{3}}{2}(d - \delta)d}$$

$$D_{eq}^{Ti} = \frac{\sqrt{3}\delta d D_{gb}^{Ti} + \frac{\sqrt{3}}{2}(d - \delta)d D_g^{Ti}}{\sqrt{3}\delta d + \frac{\sqrt{3}}{2}(d - \delta)d}$$

we can seek the correct values for the equivalent diffusivity by minimizing the weighed square errors between the predicted scale composition (thickness) and the experimental composition (thickness) .

From the calculations these values for the equivalent diffusivities were found :

$T [^\circ C]$	Element	$D_{eff} [cm^2/s]$
750	Al	1.12×10^{-16}
	Ti	9.59×10^{-17}
900	Al	3.24×10^{-15}
	Ti	2.608×10^{-15}

Table 4.9 – Calculated values of the “equivalent diffusivity “ at 750 °C and 900 °C relatively to the D_{AlAl} and D_{TiTi} terms

The average nano-crystallite size is about 15 nm (from TEM analysis , Fig 4.8 / Chapter 4) so that D_{GB} and D_G can be calculated :

T [°C]	Element	D_{GB} [cm ² /s]	D_G [cm ² /s]
750	Al	1.74×10^{-15}	3.023×10^{-19}
	Ti	1.47×10^{-15}	9.76×10^{-19}
900	Al	5.03×10^{-14}	6.16×10^{-18}
	Ti	4.01×10^{-14}	2.91×10^{-17}

Table 4.10 – Calculated values of the diffusivities at grain boundary (GB) and through the grain (G) at 750 °C and 900 °C relatively to the D_{AlAl} and D_{TiTi} terms

We can now calculate the value of the equivalent diffusivity for a specified value of the grain size using the Equation 4.2 , Chapter 4. The results are displayed in Fig 4.37

It is noticeable that below 250 nm grain size, aluminium diffusivity becomes comparable to titanium diffusivity in a wide temperature range (700 °C – 900 °C).

For $d = 0.5 \mu\text{m}$ the diffusivity coincides with the diffusivity at grain boundary .

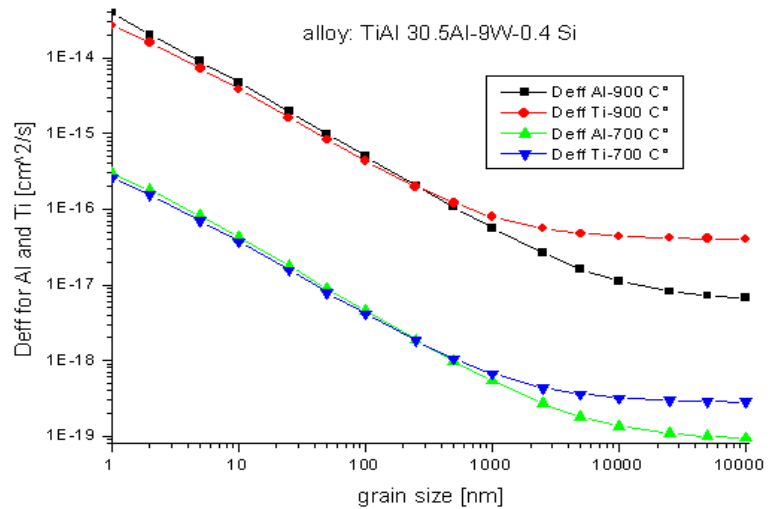


Figure 4.37- Equivalent diffusivities for Al and Ti versus the grain thickness at 700 °C and at 900 °C

As shown by Fig 4.38, there is a theoretical critical grain dimension for the oxidation resistance improvement : at 750 °C this value is approximately 500 nm.

At lower temperatures (700 °C) the calculated critical value decreases to 350 nm.

In Fig 4.38 the experimental “VPS” point indicates a VPS (Vacuum Plasma Spay) ablated sample , with grain dimension equal to about 90 nm. At 900 °C the calculated critical dimension rises up to 500 nm

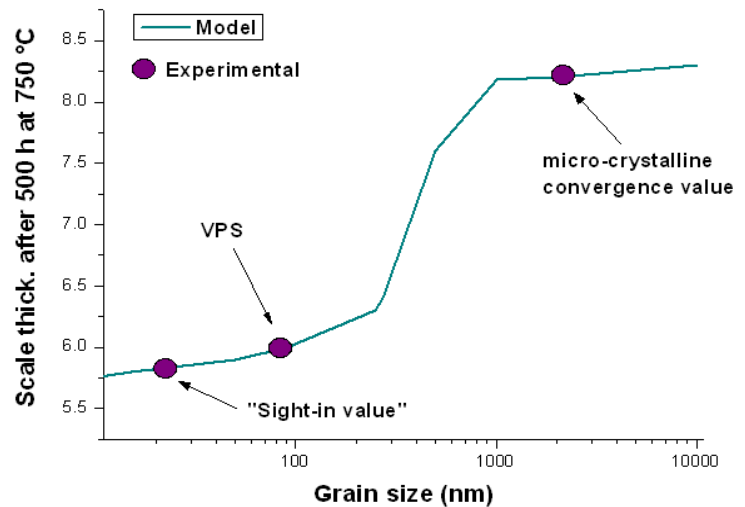


Figure 4.38 - Predicted (line) and experimental values (points) of the oxide scale thickness after 500 h of oxidation at 750 °C in air with different grain sizes

The schematization of the nanocrystallized system as in Fig 4.36 requires that :

$$L_{diff} = (D_{eq} \cdot t)^{1/2} \gg d \quad \text{Eq 4.33}$$

Where L_{diff} is the “ diffusion length “ , “ t ” the time and “ d ” the grain size.

This means that the diffusive behaviour in our material is similar to the situation “Type A” rather than the situation “Type B “ (see Fig 4.37)

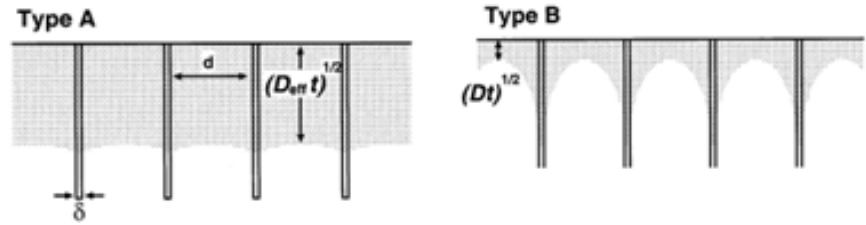


Figure 4.37- Uniformity of the " diffusion front " versus the grain thickness

This can now be verified as follows (for $t > 24$ h) at 750 °C and at 900 °C

$$750 \text{ } ^\circ\text{C} \quad \left\{ \begin{array}{l} L_{diff}^{Al} = \left(8.94 \times 10^{-17} \frac{\text{cm}^2}{\text{s}} \cdot 24\text{h} \cdot \frac{3600\text{s}}{1\text{h}} \right)^{1/2} = 2.78 \times 10^{-6} \text{ cm} = 27.8 \text{ nm} > 15 \text{ nm} \\ L_{diff}^{Ti} = \left(8.35 \times 10^{-17} \frac{\text{cm}^2}{\text{s}} \cdot 24\text{h} \cdot \frac{3600\text{s}}{1\text{h}} \right)^{1/2} = 2.68 \times 10^{-6} \text{ cm} = 26.8 \text{ nm} > 15 \text{ nm} \end{array} \right.$$

$$900 \text{ } ^\circ\text{C} \quad \left\{ \begin{array}{l} L_{diff}^{Al} = \left(3.3 \times 10^{-15} \frac{\text{cm}^2}{\text{s}} \cdot 24\text{h} \cdot \frac{3600\text{s}}{1\text{h}} \right)^{1/2} = 1.69 \times 10^{-5} \text{ cm} = 169 \text{ nm} \gg 15 \text{ nm} \\ L_{diff}^{Ti} = \left(2.6 \times 10^{-15} \frac{\text{cm}^2}{\text{s}} \cdot 24\text{h} \cdot \frac{3600\text{s}}{1\text{h}} \right)^{1/2} = 1.49 \times 10^{-5} \text{ cm} = 149 \text{ nm} \gg 15 \text{ nm} \end{array} \right.$$

In principle a post-verification of the condition $L_{diff} \gg d$ is not correct , but this assumption was necessary to solve the diffusivity problem.

The oxidation resistance improvement through laser ablation can be explained calculating the aluminium concentration at the oxidative interface for the microcrystalline and the nanocrystalline system, as shown in Table 4.11 (900 °C , up to 500 h)

Time (h)	NANO		MICRO	
	% at Al	% at Ti	% at Al	% at Ti
0	28	69	46	51
24	45	48	43	50
100	44	46	39	50
250	43	44	41	49
500	41	41	41	47

Table 4.11- Concentration of Ti and Al at the oxidation interface at 900 °C up to 500 h in the case of microcrystalline and nanocrystalline structure (calculated with the FD model)

As seen in Table 4.11 the activation of new diffusion pattern allows an high [Al]/[Ti] ratio at the oxidation interface, leading to an alumina rich scale.

5 IMPROVEMENT OF TiAl OXIDATION RESISTANCE USING THE “GETTERING EFFECT ”

The gettering effect is well known and it is the leading idea for MCrAlY coatings , where M = Ni,Co,Fe : these are alumina forming coatings even with very high Cr content (in excess of 20 wt %).

The Cr gettering effect acts in two ways :

- Reduces the “critical” aluminium content , that is the minimum aluminium content required in order to preponderantly oxidize this element
- Enhances aluminium diffusivity

MCrAlY coatings are not effective on TiAl alloys because their intrinsic chemical incompatibility with the substrate.

To solve this problem TiAlCr coatings were specifically designed : in Chapter 3.5 the oxidation behaviour of two bulk materials (Al–21Ti–23Cr and Al–37Ti–12Cr) was presented; The oxidation behaviour was very good but two additional aspects must be considered:

- the very high brittleness
- the adherence between coating and substrate

Al–21Ti–23Cr is in the $L1_2+Cr_2Al$ field and Al–37Ti–12Cr is in the $\gamma+TiAlCr$ zone : the first one has a better oxidation behaviour but the fragility of the $L1_2$ Laves phase must be considered. The equilibrium diagram is referred to 1000 °C [15]

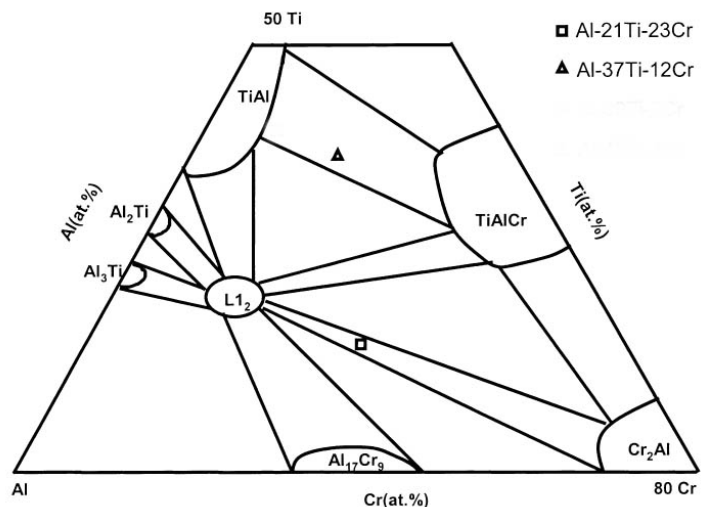


Figure 5.1- Partial section of the ternary Ti-Al-Cr phase stability diagram at 1000 °C [15]

Our methodology consist in two parts

1. The deposition (via laser ablation) of metallic Cr onto the sample surface
2. The subsequent interdiffusion treatment in order to reach the 15% [at] of Cr at the surface (the minimum Cr content in TiAlCr coatings)

The 15 % [at] of Cr at the sample external surface is in the lower zone of the TiAlCr “Cr-concentration scatter band” , which varies typically form 12 to 25 [%at].

This low “ target Cr concentration “ was chosen in order to demonstrate that there a very good oxidation resistance with a reasonable brittleness can be obtained [15].

5.1 EXPERIMENTAL

Alloy composition is given in Table 5.1

Element	Ti	Al	W	Y	Si
Wt %	bal	30.5	9	traces	0.4

Table 5.1 - Composition of the TiAl alloy used in this work

The alloy is in this case in the γ - region and a very little fraction of $\alpha_2 - \text{Ti}_3\text{Al}$ is visible , as shown in Fig 5.2. The structure type is lamellar.

Fig 5.3 shows the cross section (SEM image) and the surface of the deposited Cr layer via laser ablation (Optical Microscope)
The deposited thickness varied from 4 to 6 micron and in all cases no adhesion problems were reported .

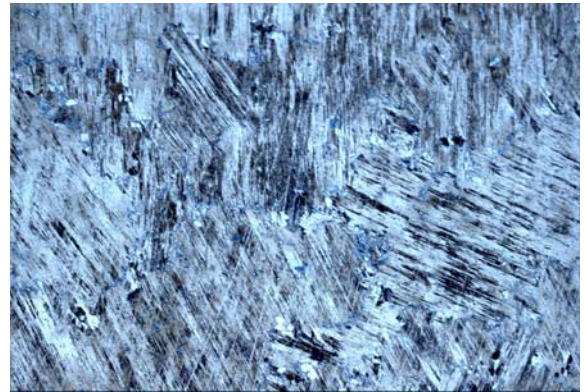


Figure 5.2 - Optical image (50X) of the TiAl alloy used in this work

Fig 5.3 shows the surface of the sample with Cr deposition : silvery - grey appearance indicates that the thickness is more than 5 micron .
This is a very practical approach and allows a very easy localization of the spots with insufficient deposition of Cr : we will see that there is a minimal suitable thickness (in relation with the expected service - temperature)

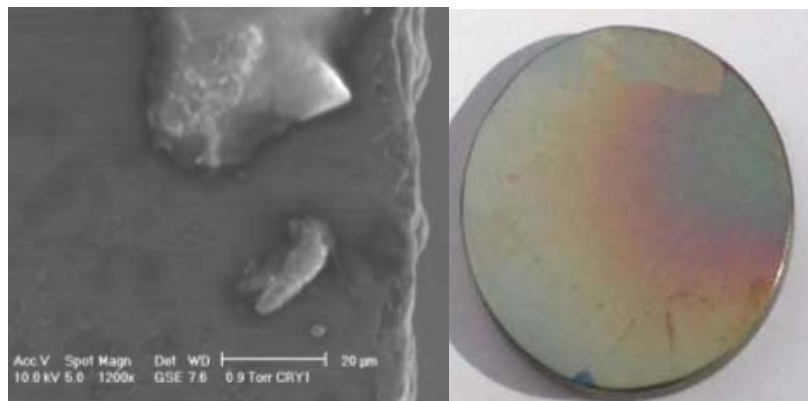


Figure 5.3 - Cross section (left) of the TiAl sample surface after the Cr deposition and relative optical image (right)

In order to compute the interdiffusion time the diffusivity of Cr in TiAl should be known : we can calculate this parameter with a “ calibration experiment “ .

The “sight-in” experiment was performed at 900 °C in inert atmosphere (Ar) for 16 h and gave this value for the diffusivity of Cr in TiAl : $D_{Cr} = 1.576 * 10^{-11} \text{ cm}^2 \text{ s}^{-1}$

The equivalent Cr diffusivity is very high (10^4 times greater) if compared with the diffusivity (trough the grain) of Ti and Al at the same temperature (see Table 4.5 in Chapter 4).

A schematic view of the diffusion problem is represented in Fig 5.4 .

In the interdiffusion stage without any oxidation reaction the atom flux at alloy surface (denoted by ξ) is only “ inward ” : the corresponding BC in this case is simply

$$C_{Cr,\xi^-} = C_{Cr,\xi} = C_{Cr,\xi^+} \quad \text{Eq 5.1}$$

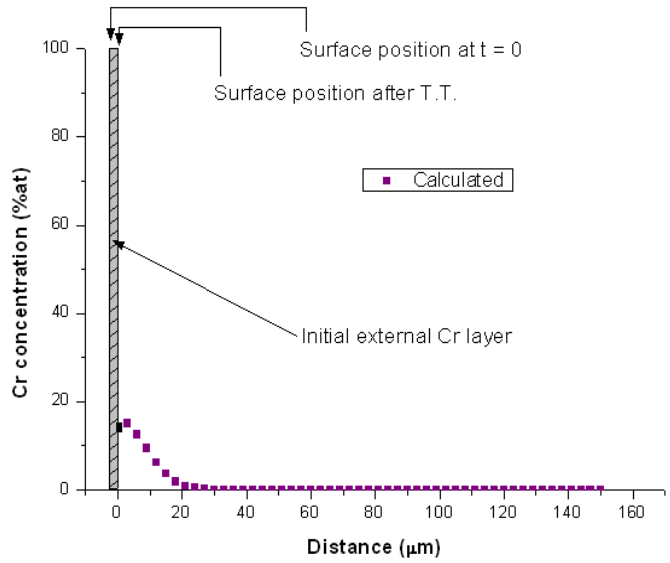


Figure 5.4 - Schematic model of the interdiffusion problem

The concentration at node ξ^- (C_{Cr,ξ^-}) is referred to the virtual “ ξ^- ” node , created only to impose an “only inward” flux from alloy surface.

The interdiffusion time can be estimated integrating 2nd Fick’s law with the implemented Finite Difference computational model :

$$\frac{\partial c_i}{\partial t} = D_{ii} \nabla^2 c_i + D_{ij} \nabla^2 c_j \quad \text{with : } \nabla^2 c = \frac{c_{i-1} - 2c_i + c_{i+1}}{\Delta x^2} \quad \text{Eq 5.2}$$

The index “i” represents a spatial node in the integration grid

We assume that Cr diffuses with an “equivalent” diffusivity which includes the effect of the non-diagonal elements of the diffusion matrix , as expressed in Eq 5.3

$$J_{Cr} = -D_{CrAl} \nabla Al - D_{CrTi} \nabla Ti - D_{CrCr} \nabla Cr \approx -D_{Cr}^{eff} \nabla Cr \quad \text{Eq 5.3}$$

For a given thickness “s” (of deposited Cr) we can use this formula to determine rapidly the interdiffusion time (at 900 °C):

$$t^{TT} = -0.55 + 0.325 * s + 0.225 * s^2 \quad \text{Eq 5.4}$$

Units are hours for the time and micron for the thickness (s). This thermal treatment leads to a Cr concentration of 15%(at) at the surface.

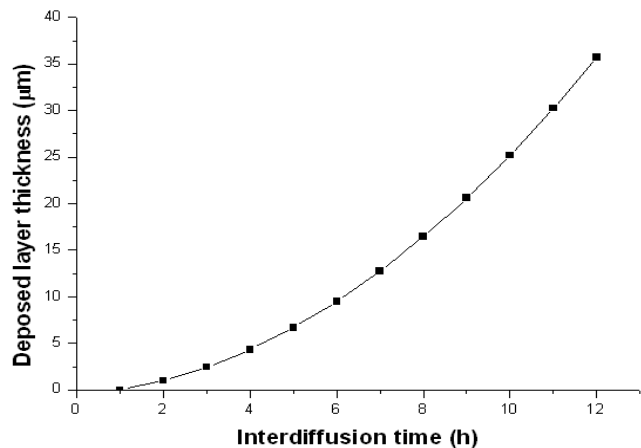


Figure 5.5- Estimated interdiffusion time vs the deposited Cr thickness (at 900 °C)

Fig 5.6 shows a slice of the specimen after the thermal interdiffusion treatment (TT) performed at 900 °C for 9 hours , as requested for 6 micron of deposited Cr. The appearance is very bright due the previous polishing.

Other treatments would not give a roughness like this : for example in order to operate a laser treatment the surface shouldn't be bright (in this case the laser impulse will be reflected)



Figure 5.6 - Cr - coated sample appearance after interdiffusion treatment

In the “ interdiffused “ condition with XRD analysis no new phases (except about a small percentage of Cr_{0.88} Ti_{0.12}) were detected. A quantitative XRD analysis will not to be reliable due the implicit non- homogeneity of a layered structure

The quantity of Cr_{0.88} Ti_{0.12} is in fact negligible and for this reason no correction on the Fick's second law was used (such as chemical potentials gradients originated by new phases or “ Cr-storage” boundary condition) .

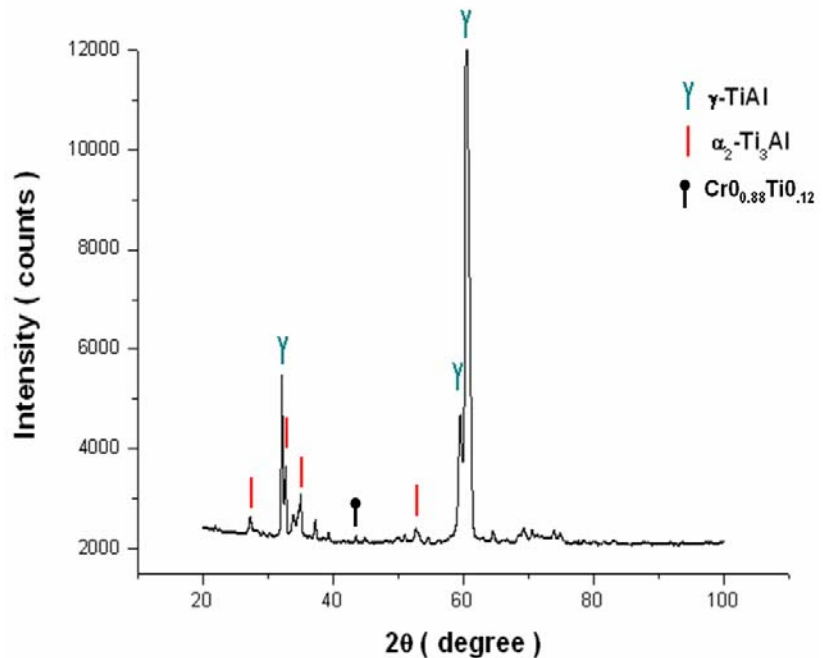


Figure 5.7 - XRD pattern of the TiAl sample after interdiffusion treatment

With the Cr interdiffusion treatment the cell parameter set of γ-TiAl are equal to

$$\begin{cases} a = 4.062 \text{ [Å]} \\ c = 4.10 \text{ [Å]} \end{cases}$$

Oxidation tests were performed at 900 °C , 1000 °C and at 1100 °C in air in a tubular furnace

5.2 RESULTS AND DISCUSSION

As seen in Chapter 3.7 (“ The improvement of high temperature oxidation of Ti50Al by sputtering Al film and subsequent interdiffusion treatment “) the improvement of oxidation resistance is limited when the Al film thickness is less than 2 μm . In that work this motivation is given : “ This may be because the thickness of TiAl_3 layer is not thick enough to protect against the diffusion of oxygen into the substrate “; Maintaining the same interdiffusion time (24 h at 600 $^\circ\text{C}$) for different deposited thickness is in fact erroneous : if the ratio between time and deposited layer thickness to high is then the formation of a TiAl_3 layer becomes impossible.

In order to obtain a surface layer of TiAl_3 a minimum Al concentration of about 63% (as weight) is required , as shown in Fig 5.8

If a 24 hours – long TT performed at 600 $^\circ\text{C}$ allows the formation of a TiAl_3 layer (starting with 5 micron of deposited Al) then the diffusivity of aluminium should be between $0.98 \cdot 10^{-15} \text{ cm}^2 \text{ s}^{-1}$ and $1.21 \cdot 10^{-15} \text{ cm}^2 \text{ s}^{-1}$.

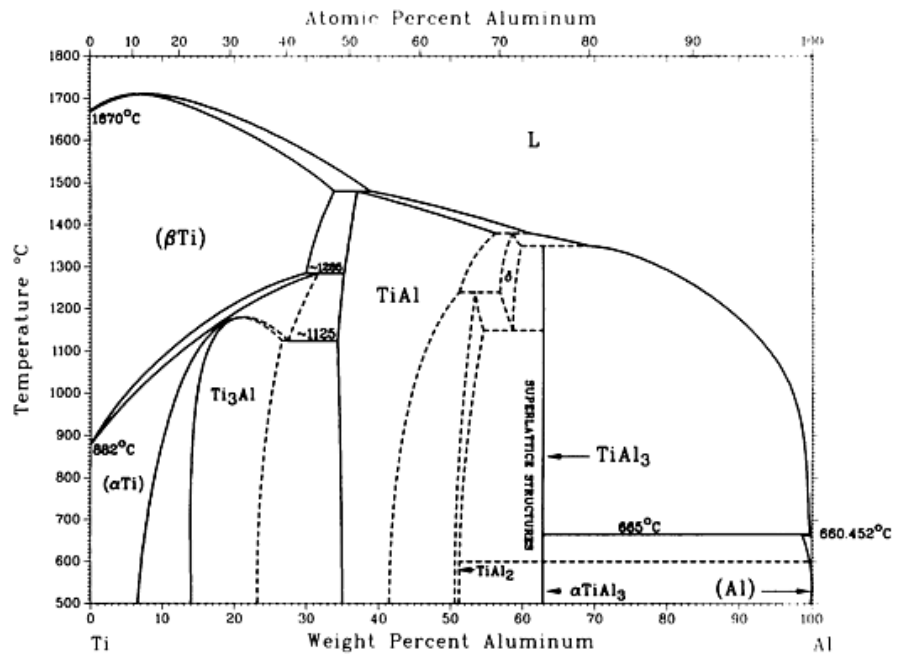


Figure 5.8 - Ti,Al stability phase diagram [52]

By integrating the Fick’s second law we can now calculate the right interdiffusion time for Al deposition , in order to obtain a superficial layer of TiAl_3

$$t^{TT} = 0.3 + 0.0265 * s + 0.9508 * s^2 \quad \text{Eq 5.5}$$

With our approach we need only a “ calibration experiment “ in order to calculate the diffusivities: the methodology allows to estimate still for example the effect of an imperfect Cr deposition.

Fig 5.9 shows a slice of TiAl with a “linear in the space” deposited thickness (20 micron on the left side and virtually 0 micron on the right side) .

We can calculate the interdiffusion profile on a real component generalizing the Fick’s law integration in 3D.

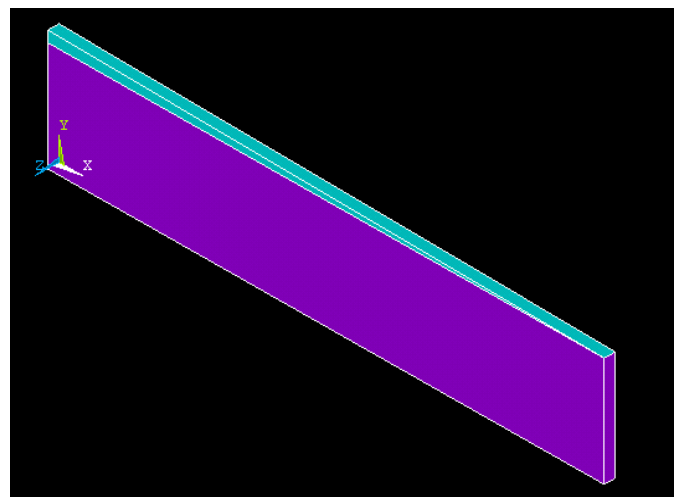


Fig 5.9 Deposited layer with variable thickness on a material slice

Fig 5.10 shows the diffusion profile after 24 h at 900 °C in an inert atmosphere : We can note that Cr content on the left side is too high (higher as 15 % at) ; on the other hand the content of Cr on the right side is too low for a reasonable oxidation resistance improvement

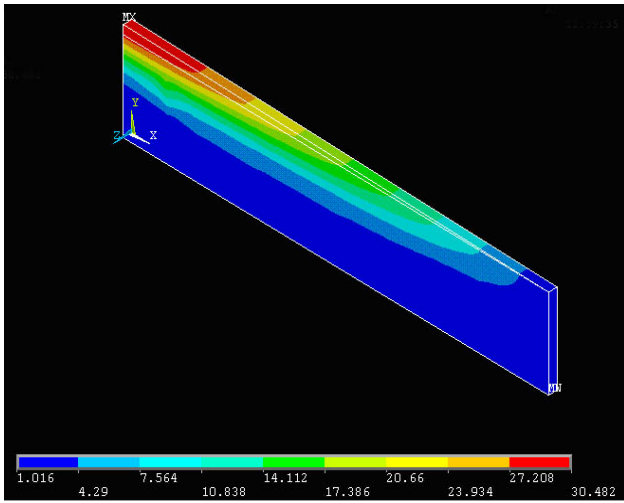


Fig 5.10 Calculated interdiffusion profile after a specified thermal treatment

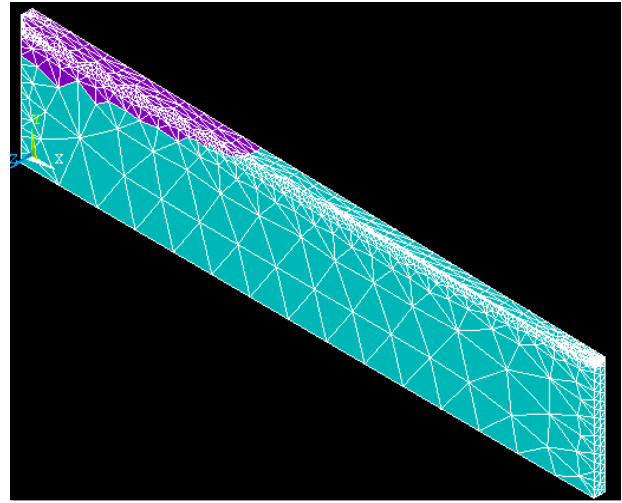


Figure 5.11 – Elements of the slice (purple color) with high chrome content after the interdiffusion treatment

If Cr content is higher than 20 [%at.] then the formation of L_{12} Laves phase will occur . After the interdiffusion profile calculation we can find the elements with these concentration values , identified by purple colour in Fig 5.11.

Result of the oxidation test

With Cr-rich samples oxidation resistance improvement at 1000 °C was very high:

Fig 5.12 and Fig 5.13 show the external scale obtained after 500h at 1000 °C for the bare alloy and Cr – interdiffused alloy , respectively.

The Kp reduction is about two orders of magnitude.

We can note that in the second case the scale has not a layered structure as in the bare alloy case. The scale adhesion in the case of Cr interdiffusion was very good.

The scale composition is quite uniform in terms of $\text{Al}_2\text{O}_3/\text{TiO}_2$ ratio.

The scale microstructure is very fine if compared with the scale found on the bare alloy : this improves the scale plasticity.

As seen in Chapter 4 laser – ablated alloy and the bare TiAl alloy were prone to massive oxide scale spallation after 250 h of annealing at 900 °C : On the Cr-coated samples after 500 h of oxidation at this temperature the oxide scale seems to be strongly bonded to the substrate.

Fig 5.14 shows the oxidation kinetic at 1000 °C for bare TiAl alloy and Cr-treated alloy.

In this case the oxide growth is measured with oxide scale thickness and not with specific weight change (as usual) due the impossibility to treat with Cr the whole area of the sample

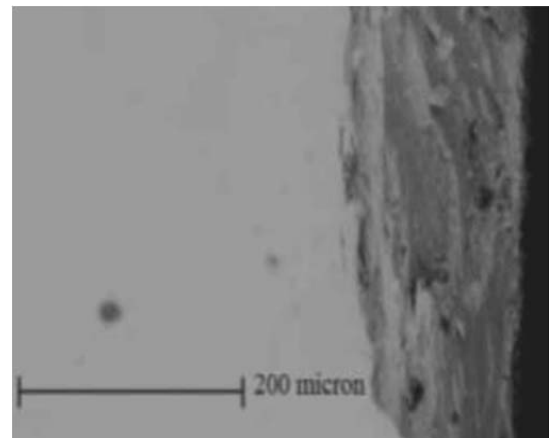


Figure 5.12 - External oxide scale of an untreated TiAl sample after 500 h of oxidation at 1000 °C in air

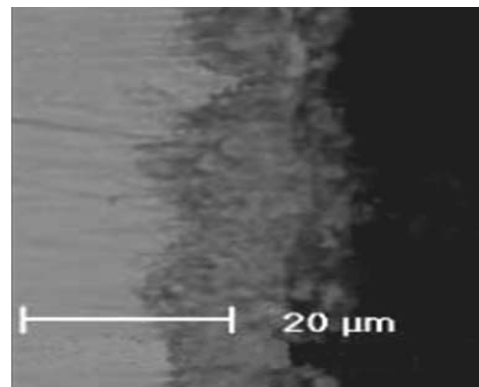


Figure 5.13 - External oxide scale of an TiAl Cr-coated sample after 500 h of oxidation at 1000 °C in air

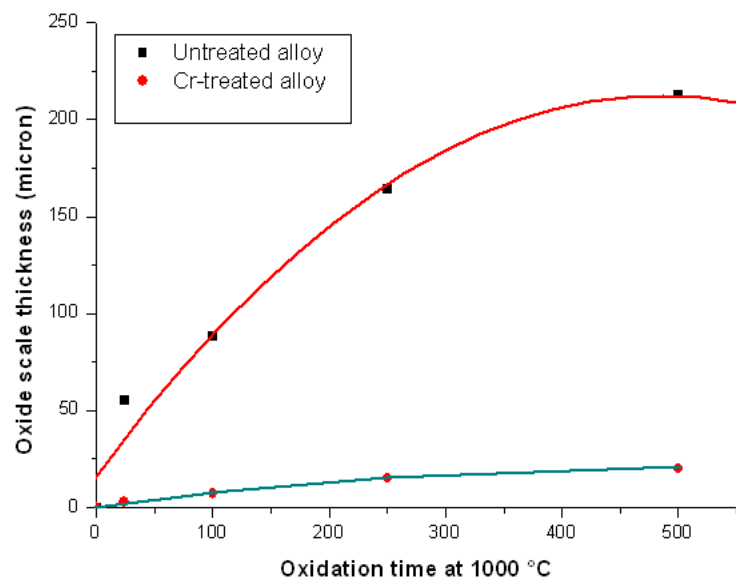


Figure 5.14 - Oxide scale thickness vs oxidation time (h) at 1000 °C

Fig 5.15 shows the experimental oxidation kinetic at 900 °C in air for untreated TiAl alloy and Cr-treated alloy.

Here the oxidation resistance improvement is more evident that the improvement obtained via laser ablation.

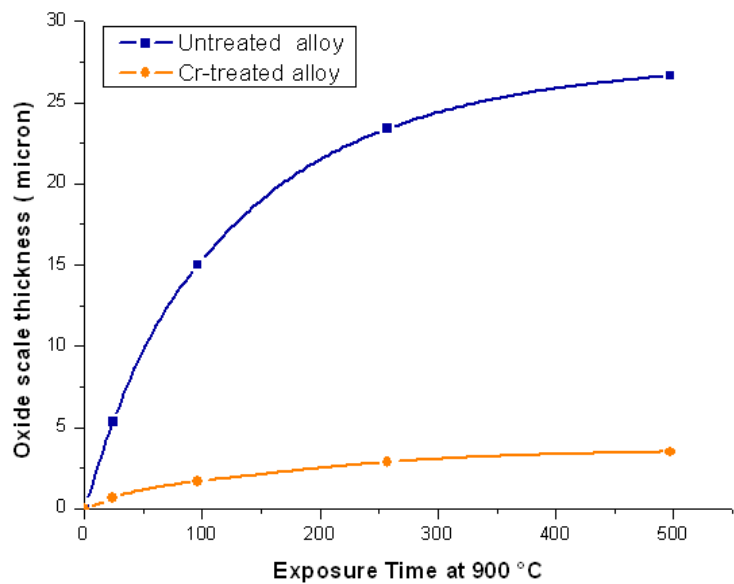


Figure 5.15 - Oxide scale thickness vs oxidation time (h) at 900 °C

Fig 5.3 shows the sample after the Cr deposition : in order to test it at 1000 °C the whole surface should be well coated , showing an uniform silvery grey colour on the surface.

If the Cr layer thickness does not reach a minimum of 5-6 micron then local oxidation of Ti can occur : the result is the formation of a TiO₂ structure which has usually a “volcano-like” appearance. An example of someone’s TiO₂ “volcano” is shown in Fig 5.16



Figure 5.16- Local defect in the oxide scale on an Cr - coated sample after 500 h of oxidation at 1000 °C

Some defects were not observed after oxidation at 900 °C

Fig 5.17 shows a SEM image of the TiO₂ volcano , indicated by the yellow arrow in Fig 5.16.

The sample was oxidized in air for 500 h at 1000 °C

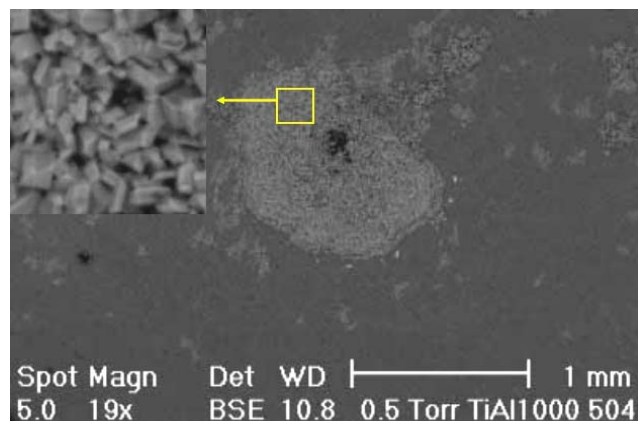


Figure 5.17 - detail of the superficial defect in the oxide scale indicated by the yellow arrow in Fig 5.16

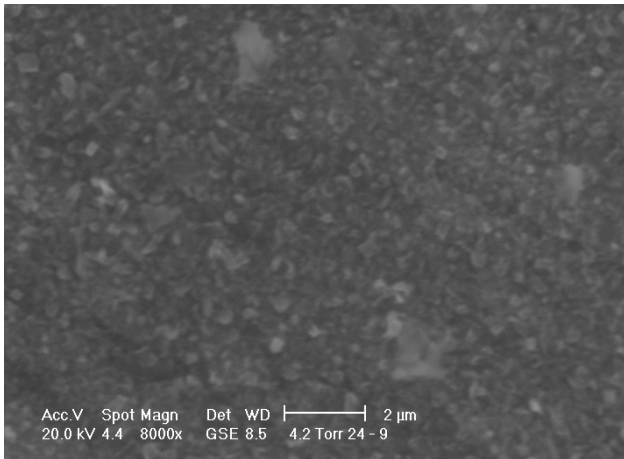


Figure 5.18 - Superficial appearance of the oxide scale after 250 h of oxidation at 1000 °C

Fig 5.18 shows the surface of the scale formed at 1000 °C after 250 h of oxidation in air.

The scale structure consists of TiO_2 platelets in a Al_2O_3 matrix : it is necessary that in order to obtain such as an oxidation resistance improvement the TiO_2 platelets shouldn't be paired and interconnected and in this case the oxygen diffusivity will be strongly reduced.

TiO_2 grows mainly by oxygen diffusion via oxygen vacancies in it and Al_2O_3 grows by the oxygen diffusion via self diffusion in it . The diffusivity of oxygen trough Al_2O_3 is about four orders of magnitude smaller as the diffusivity of oxygen trough TiO_2 : this fact implies that a small interconnection trough the TiO_2 platelets can supply a relatively large quantity of oxygen for the oxidation.

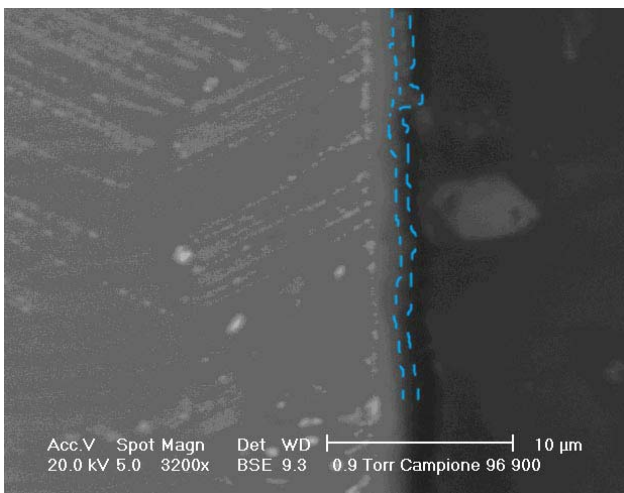


Figure 5.19 - Cross section of the oxide scale formed on a Cr-enriched sample after 96 h of oxidation at 900 °C

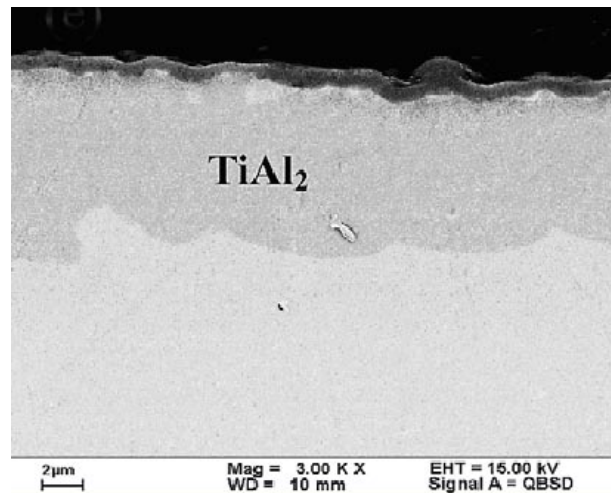


Figure 5.20 - Cross section of the oxide scale formed on a Al-enriched sample after 80 h of oxidation at 900 °C

Fig 5.19 shows the oxide scale formed on a Cr- enriched sample after 96 h of oxidation at 900 °C , externally delimited by the two dashed lines :The oxide scale thickness varies from 0.9 μm to 1.3 μm . The average value is 1.1 μm .

In this case the thickness of the oxide scale was so low that the shiny alloy surface was still visible. Before the Cr deposition the sample surface can be as “mirror” finished : this surface finishing in not suited for laser ablation process , in order to avoid reflections of the incoming beam.

Similar values (slightly bigger) are obtained with superficial Al enrichment (but on Ti50Al alloy) as shown in Fig 5.20 [24] (see Chapter 3.7) after 80 h of annealing at 900 °C

Onto the surface of the samples oxidized at 900 °C chromia efflorescences as “rose – structures “ were observed. The Cr₂O₃ don't seems to grow in a particular location and no relationships between oxidation time , dimension of the roses , and their total amount were found.

No roses were found after the oxidation at 1000 °C : this fact is securely due to the Cr₂O₃ evaporation.

The interdiffusion time was calculated in order to promote the formation of alumina (gettinger effect) without Cr oxidation : probably there is locally an insufficient Cr interdiffusion due to a bad aligned γ-TiAl (or an α₂-Ti₃Al) grain.

Cr loss during oxidation can be determined with the integration of EDXS linescan along the cross section of the sample.

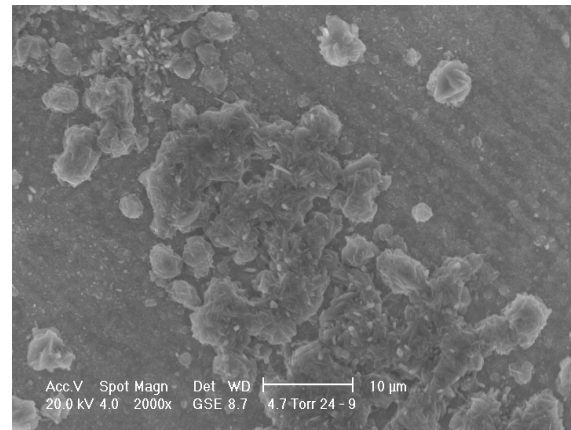


Figure 5.21- Chromia agglomerates on the surface after 24h of oxidation in air at 900 °C

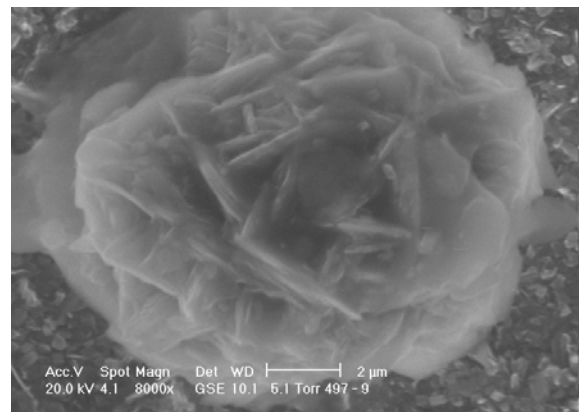


Figure 5.22- SEM Magnification of a chromia rose founded on the sample surface after 500h of oxidation at 900 °C, in air

As reported in Fig 5.23 a negligible amount of Cr₂O₃ was found after oxidation at 900 °C. The Al₂O₃ peak is very high if compared with TiO₂ peak . The “more reliable” EDXS microprobe confirms this fact. Alumina is the main oxidation product in the case of Cr treated TiAl alloy.

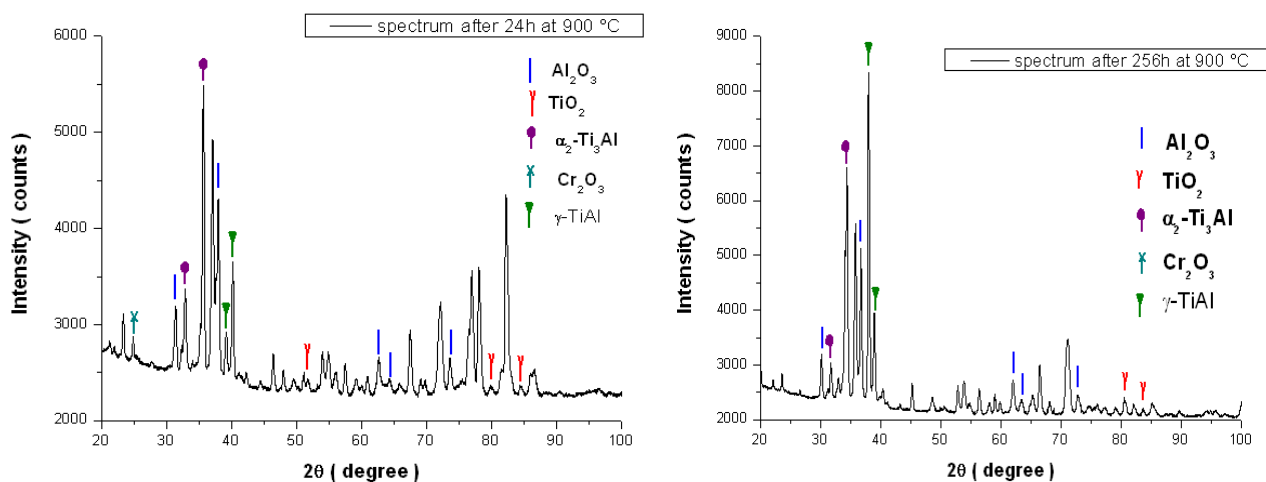


Figure 5.23 - XRD diffraction patterns of the surface of two oxidized chrome - coated TiAl samples; oxidation conditions are : 24h at 900 °C (left) and 256h at 900°C (right)

No Al depletion zones at the alloy-oxide scale were found with EDXS probe : this means that the γ -TiAl doesn't transform itself into α_2 -Ti₃Al.

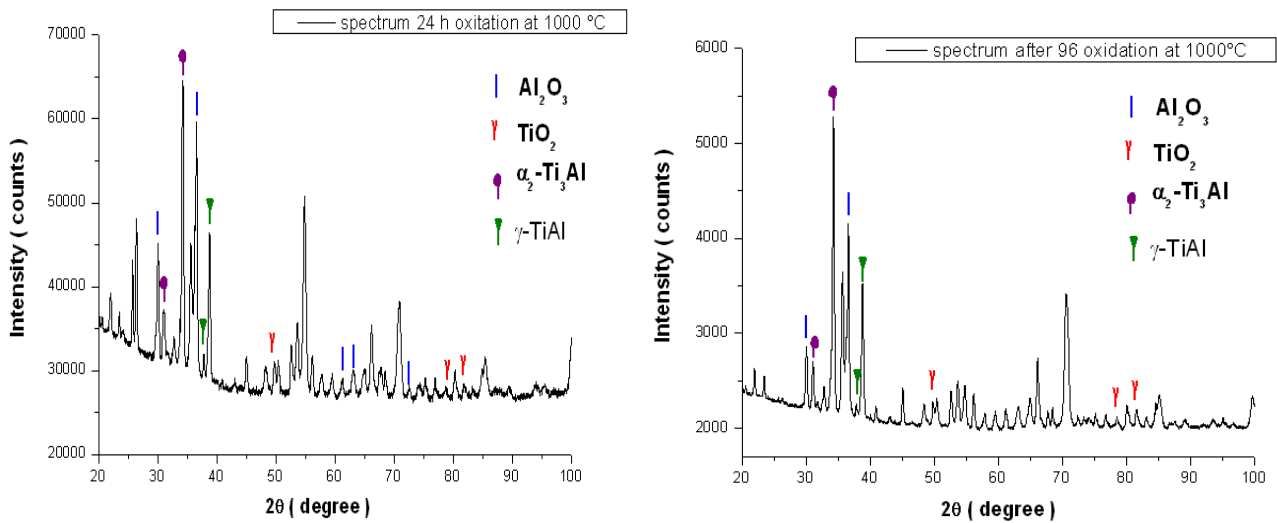


Figure 5.24 - XRD diffraction patterns of the surface of two oxidized chrome - coated TiAl samples; oxidation conditions are : 24h at 900 °C (left) and 96h at 1000°C (right)

Some Cr treated samples were tested still at 800 °C and no Cr₂O₃ was found in the oxide scale with XRD analysis.

This means that the Cr concentration at the surface allows the preferential oxidation of aluminium and does not lead to a Cr consumption via oxidation because Cr₂O₃ is not volatile at 800 °C.

This “average K_p” value can be now calculated (fitting the scale thickness – time relationship and assuming Arrhenius temperature dependence) as:

$$K_p = 1.248 \cdot 10^{17} \cdot \text{Exp}(-420136/RT) \quad [K_p] = [\mu\text{m}^2\text{s}^{-1}] \quad \text{Eq 5.6}$$

The validity of this formula is theoretically limited between 900 °C and 1000 °C , but we can note the relatively high activation energy and its value predict a very good oxidative behaviour even above 1000 °C.

This result was obtained with a very small Al percentage (if compared with other alloys used for oxidation tests, such as Ti50Al).

There is a substantial difference between Al interdiffusion (Chapter 3.7) and Cr interdiffusion : the first treatment gives an “initial increased budget of Al” which leads to the formation of an TiAl₃ layer. TiAl₃ transforms it self into TiAl₂ during oxidation and finally into γ TiAl : at this point no any oxidation resistance improvement would be possible [24]. The time for the complete transformation form TiAl₃ to γ -TiAl is calculated as 700h at 900°C [24]

The Cr interdiffusion treatment does not loose its effect because no Cr is consumed during the oxidation (only a small quantity evaporates in the initial oxidation stages as volatile Cr₂O₃ at temperatures in excess of 900 °C).

No aluminium depletion zones were found beneath the oxide scale : we must consider that in this case the aluminium flux as “ fuel “ for the oxidation is still reduced due the lower oxygen diffusivity trough the scale : this can lead to aluminium depletion zones absence.

Fig 5.25 shows the concentration profiles of Al and Ti trough a surface cross section of a sample oxidized for 500 h at 900 °C.

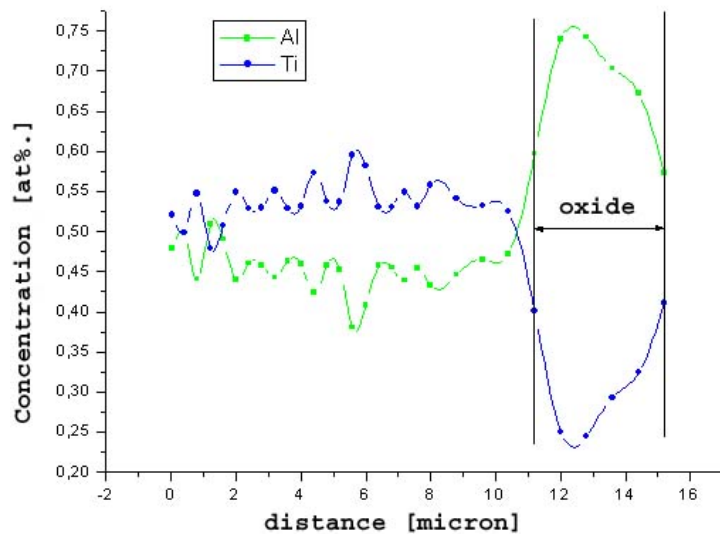


Figure 5.25 - Aluminium and Titanium concentration profiles after 500h of oxidation at 900°C in air

At 1100 °C the chrome interdiffusion treatment was not capable to protect the sample surface for in excess of 100 h periods.

After 100 h of oxidation exposure a small scale exfoliation process was observed.

The oxide scale on the treated side denotes as white – grey colour.

After 100 h of oxidation at 1100 °C (in isothermal condition) the scale was approximately 45 micron thick , but with good adherence.

At 1100 °C the strongest diffraction line was the titanium oxide peak (for both testing times : 24 and 100 h).

The XRD quantitative analysis is in this case unreliable due the non uniformity of the stratified oxide scale : the EDXS microprobe quantifies the alumina percentage as 35 % (at.).

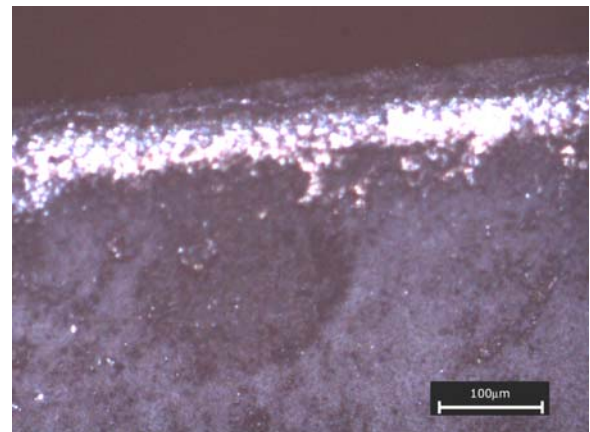


Figure 5.26 – Optical microscope image of the surface cross section of a TiAl oxidized sample for 100h at 1100 °C

As said before at 1100 °C the strongest line of the oxide scale diffraction pattern was the titanium oxide line.

Under the oxide scale a very thick layer of β -Ti was found : this has itself securely formed via the strong aluminium depletion beneath the oxide scale

Fig 5.27 shows the SEM surface cross section of a chrome coated sample oxidized for 100h at 1100 °C .

We can note the bright layer (BSE detector selected) under the external oxide scale : it is formed of β -Ti with tungsten in solution . This β -Ti is very brittle and leads to scale detachment , as shown in Fig 5.28
 We can observe in Fig 5.28 the bare alloy surface in absence of the protective external oxide scale : this implies that we are in presence of a particular fracture mechanism , as in the “ intersigmatic fracture process “ , which is typical for NiCoCrAlY Re-coating systems.

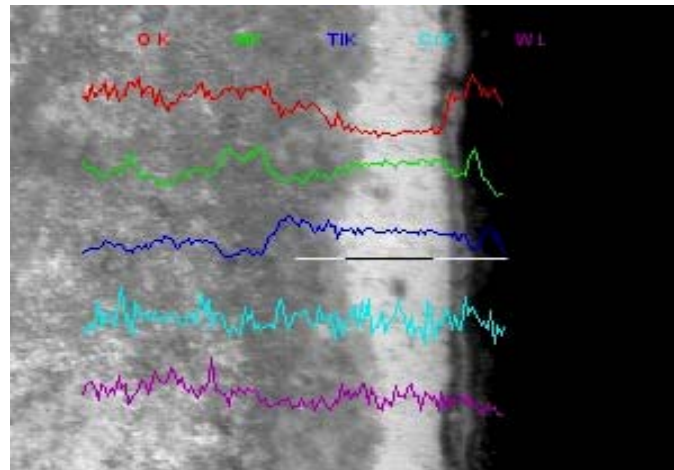


Figure 5.27- SEM image of a Cr-coated TiAl sample with EDXS concentration profiles for O,Al,Ti,Cr and W ; Oxidation conditions are 100h at 1100 °C

We can note in Fig 5.27 that the “ordinary” scale stratification is locally inverted:
 $Al_2O_3/TiO_2/Al_2O_3$ instead of $TiO_2/Al_2O_3/TiO_2$ /internal oxidation
 This means that the formation of alumina is initially favoured from the gettering effect.

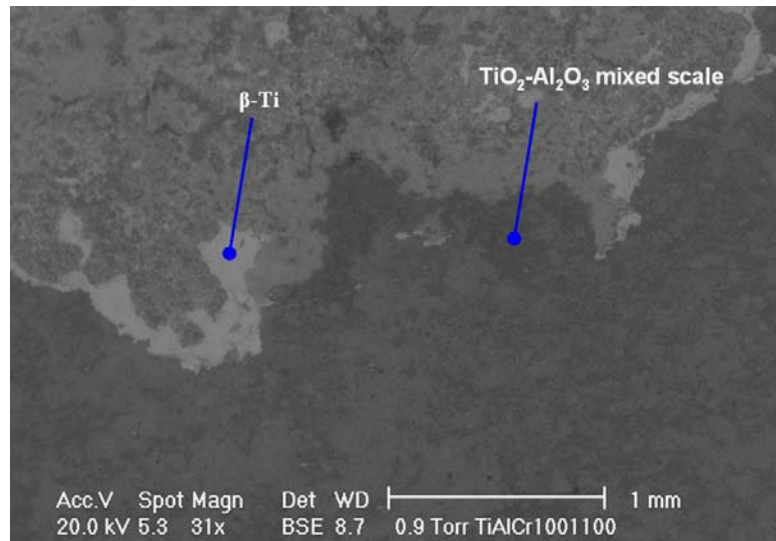


Figure 5.28 -SEM image of the surface of an Cr-coated sample after 100h of oxidation at 1100 °C: the scale is partially detached

The linearity of K_p in the Arrhenius-plot graph in the 900 °C – 1100 °C range was with very good agreement respected , as shown in Fig 5.29 .
 There are not detectable activation energy changes in the mentioned temperature range.
 The experimental data for $T=1100$ °C are coming from the scale thickness determination of the two tested samples at this temperature : oxidation times are 24h and 100h.

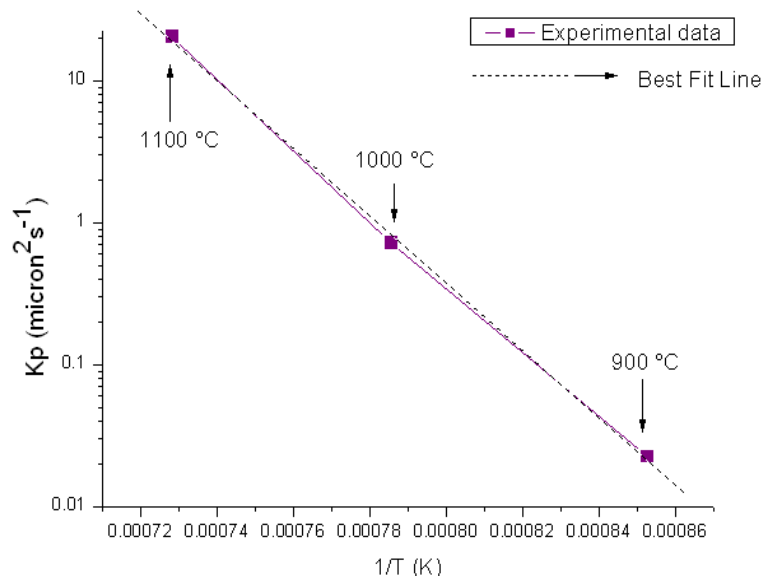


Figure 5.29- Arrhenius plot of K_p in the 900°C - 1100°C range

6 CONCLUSIONS

Some methodologies for oxidation resistance improvement of TiAl alloys were examined under a critical point of view : as shown in Fig 5.30 at 900 °C the Cr-surface enrichment and the NiAl coating are the two most promising surface approaches.

The Cr superficial enrichment seems to be the best strategy in order to obtain a significant oxidation resistance improvement : there aren't any adhesion problems and chemical incompatibility as by TiAlCr, NiAl or so. The Cl ions implantation remains also very attractive due its high efficiency and the easiness of the doping procedure but the existence of a "critical chlorine concentration" value in order to obtain a positive effect is the most limiting factor for its practical application

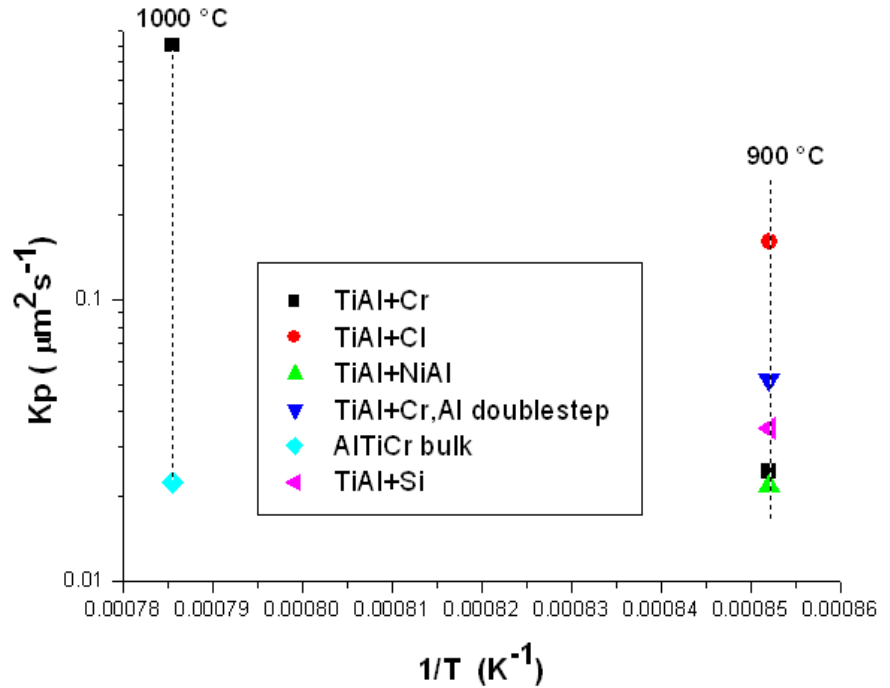


Figure 5.30- Kp values at 900 °C and 1000 °C for all the protection methodologies presented in this work

The values of the data represented in Fig 5.30 are given in the following table (Table 5.2)

Treatment	Chlorine	NiAl coating	Laser ablation	Cr+Al pack cementation	AlTiCr bulk	TiAl + Si	TiAl+Al	TiAl+Cr
Kp @ 900°C [μ²s⁻¹]	0.16	0.02179	0.969	0.0522		0.035	0.0151	From 0.0145 to 0.0225
Kp @ 1000°C [μ²s⁻¹]					0.0225			0.722
Kp @ 1100°C [μ²s⁻¹]				76.4				20.25
References	[9]	[10][11]	Present work	[14]	[15]	[20]	[24]	Present work

Table 5.2- Final results table for Kp values at 900 °C , 1000 °C and 1100 °C

This oxidation resistance improvement was obtained onto a composition-optimized alloy , as shown in Table 5.3 : our alloy was the best under a oxidation resistance perspective (in the untreated condition).

Alloy	Methodology	K_p "as untreated" [$\mu\text{s}^{1/2}$] at 900 °C
Ti-48Al-1.3Fe-1.1V-0.3B	Siliconizing	2.13
Ti50Al	Al interdiffusion	9.33
Ti50Al	Cl implantation	2.668
Ti30.5Al19W0.4Si	Cr interdiffusion	1.204

Table 5.3 - K_p values (at 900 °C) in the untreated condition for the different mentioned alloys (for our methods and for the bibliographic resources)

The quantitative-predictive approach used in this work is very useful and versatile ;

In the case of Ni-based superalloys some computational methods are often used , in order to optimize their concentration , avoiding long term phase instabilities. Our methodology can be coupled with these calculations for a double optimization process : oxidation resistance and bulk phase stability.

The computer calculation of phase equilibria in multicomponent alloys is becoming increasingly commonplace and it is now possible to make very accurate predictions for phase equilibria in a number of the more commonly used metallic and intermetallic alloys. These range from steels [53] to Ti-aluminides [54]. This paper will present results which can now be obtained in Ni-based superalloys giving a number of examples of where this methodology has been applied.

The CALPHAD method first requires that sound mathematical models exist for describing the thermodynamic properties of the various phases which can appear in an alloy. The coefficients used by the models are then held in databases which are accessed by software packages such as Thermo-Calc^[54] which then perform a series of calculations, usually via Gibbs energy minimisation, to provide the user with detailed information on phase equilibria. These calculations can be augmented with kinetic modelling to provide answers for phase formation under conditions which can deviate substantially from equilibrium [55] [56]

Early attempts at modelling of superalloys mainly concentrated on ternary sub-systems ^{[57] [58] [59]} . They provided some guidance in the search for high temperature eutectic reactions but the simple model types used in this early work inherently limited their more general usage. For example was treated as a stoichiometric or line compound whereas it is substantially non-stoichiometric in practice. New models have been developed which now allow the full solubility range and thermodynamic properties of intermetallic compounds (such as γ' -Ni₃Al) to be modelled very accurately [60] [61] .Some four years ago a development programme between Thermotech Ltd and Rolls-Royce plc was started to develop a database which could be used for CALPHAD and related calculations in Ni-based superalloys. Results [62][63] have demonstrated that the accuracy of calculated phase equilibria lies close to that obtained experimentally for commercial superalloys. Some applications of the database will then be shown including application to non-equilibrium solidification, σ phase formation and prediction of APB energies in γ' .

The roots of the CALPHAD approach lie in the mathematical description of the thermodynamic properties of the phases of interest. If they are stoichiometric compounds the composition is defined

and a mathematical formula is then used to describe fundamental properties such as enthalpy and entropy. Where phases exist over a wide range of stoichiometries, which is the usual case for metallic materials, other mathematical models are used which account for the effect of composition changes on free energy. Details of modelling procedures can be found in the review of Ansara [65]. All types of models require input of coefficients which uniquely describe the properties of the various phases and these coefficients are held in databases which are either in the open literature or proprietary.

The main models used in the present work are the substitutional type model [64]. and the multiple sublattice model [61]. Both of these models can broadly be represented by the general equation for a phase

$$\Delta G = \Delta G^\circ + \Delta G_{mix}^{ideal} + \Delta G_{mix}^{xs} \quad \text{Eq 5.7}$$

where ΔG° is the free energy of the phase in its pure form, ΔG_{mix}^{ideal} is the ideal mixing term and ΔG_{mix}^{xs} is the excess free energy of mixing of the components. It is not within the scope of the present work to describe in detail these models, particularly the multiple-sublattice model, but it is useful to briefly discuss some of their aspects.

The free energy of the substitutional model (ΔG_m) for a many component system can be represented by the equation where “ x_i ” is the mole fraction of component “i”, “ ΔG_{i0} ” defines the free energy of the phase in the pure component “i”, T is the temperature and R is the gas constant. Ωv is an interaction coefficient dependent on the value of v. When $v = 0$, this corresponds to the regular solution model and when $v = 0$ and 1 this corresponds to the sub-regular model. In practice the value for v does not usually rise above 2.

$$\Delta G_m = \sum x_i \Delta G_i^0 + RT \sum x_i \log_e x_i + \sum_i \sum_{j>1} x_i x_j \sum_v \Omega v (x_i - x_j)^v \quad \text{Eq 5.8}$$

Eq.5.8 assumes higher order interactions are small in comparison to those which arise from the binary terms but this may not be always the case. Ternary interactions are often considered but there is little evidence of the need for interaction terms of a higher order than this. Various other polynomial expressions for the excess term have been considered, see for example the reviews by Ansara [65] and Hillert [65], however all are based on predicting the properties of the higher-order system from the lower-component systems. The multi-sublattice model is substantially more complex and considers the phase to be made up of multiple interlocking sublattices. There are then interaction terms to be considered (i) between the sublattices and (ii) on the sublattices themselves.